Print ISSN 0033-9008
Online ISSN 1880-1765

QUARTERLY REPORT of RTRI

May 2025 Vol. 66 No. 2

CONTENTS

PAPERS

SUMMARIES

H Human factors
I Infrastructure
N Natural hazards
O Operations
R Rolling stock
T Technical system integration and interaction

RAILWAY TECHNICAL RESEARCH INSTITUTE

QUARTERLY REPORT of RTRI

Print ISSN 0033-9008
Online ISSN 1880-1765 May 2025 Vol. 66 No. 2

CONTENTS

PAPERS

SUMMARIES

[H] Human factors
[I] Infrastructure
[N] Natural hazards
[O] Operations
[R] Rolling stock
[T] Technical system integration and interaction

Stationary and Onboard Energy Storage System Control Method for Making Use of Renewable Energy

Takeshi KONISHI
Power Supply Systems Laboratory, Power Supply Technology Division
Takamitsu OGATA **Tamanosuke OIDE**
Power Supply Systems Laboratory, Power Supply Technology Division (Former)
Tatsuhito SAITO
Hydrogen and Sustainable Energy Laboratory, Vehicle Technology Division

The installation of renewable energy is accelerating to achieve carbon neutrality by 2050. This paper proposes a control system for integrating charge/discharge of stationary and onboard energy storage systems on DC electrified railways. A simulation of the performance of a train operation power shows the effect of the demand response and effective use of renewable energy by adopting the control system for energy conservation.

Key words: *integrated control, stationary energy storage system (SESS), onboard energy storage system (OESS), demand response (DR), DC traction power supply system*

1. Introduction

The Government of Japan has announced a policy to achieve carbon neutrality by FY2050 and has set an ambitious goal of reducing greenhouse gas emissions by 46% by FY2030 compared with FY2013.

Since carbon dioxide (CO_2) emitted from energy sources accounts for most greenhouse gas emissions in Japan, it is very important to reduce these emissions.

The Ministry of Land, Infrastructure, Transport and Tourism (MLIT) of Japan is promoting the following three objectives for the railway sector:

- "Decarbonization of railways" to reduce CO_2 emissions through energy conservation and electrification of diesel railcars,
- "Decarbonization by railways" to generate, transport and store renewable energy or hydrogen energy by utilizing railway assets, and
- "Decarbonization supported by railways" to reduce CO_2 emissions by promoting citizens to use railway services.

The growing installation of PV (photovoltaic power generation) is contributing to the realization of carbon neutrality in 2050. The power generation characteristics of PVs significantly depends on daylight, season and weather, means that this source of energy differs from other conventional power sources. At the same time, the daily power demand curve of railways is significantly different from the power generation characteristics of PV power. This therefore increases the significance of utilizing stationary energy storage systems (SESSs) for compensating differences in power generation and consumption. However, conventionally SESS is installed to utilize regenerative energy of electric trains. Therefore, it is necessary to improve methods for controlling conventional SESS to utilize PV energy which is generated on the power grid side.

To contribute to "decarbonization of railways" and "decarbonization by railways," firstly, the authors have proposed a new charge/discharge control method for SESSs to charge PV energy from the power grid. Secondly, the authors have proposed an integrated control method for some SESSs and onboard energy storage systems (OESSs) in the DC traction power supply system. In addition, the authors have carried out a study on effectiveness of the demand response (DR) control system for the integrated ESSs.

2. Charge/discharge control method of ESSs for utilization of both regenerative energy and renewable energy

2.1 Outline of ESSs for electrified railway systems

SESSs installed in Japan today are for effective use of regenerative power in DC electrified railways or used as emergency power sources in case of a disaster such as a large earthquake. In addition, OESSs are mainly used as a traction power sources on non-electrified lines and an emergency power sources for lighting or allowing trains to run to nearby stations on electrified lines. The typical kWh-capacity of SESS is less than 500 kWh, and that of OESS is less than 30 kWh per car when running on electrified lines, respectively.

2.2 Concept of proposed charge/discharge control

Figure 1 shows an image of applying SESSs to the DC Traction Power Substation (TPSS) [1] to contribute "decarbonization of railways." PV is selected as an example of renewable energy in this study.

The power load for traction substations tends to be larger during rush hours, such as in the morning and in the early evening. On the other hand, the power generated by renewable energy sources such as PV is usually high during the day. Therefore, the load of the TPSS and the generated power of PV are quite different in terms of their characteristics. The excess PV energy can be absorbed and can be discharged to electric trains by using SESSs. In addition to the use of PV energy, the use of utilizing regenerative energy through the braking of electric trains is also promising.

In order to realize the power flow shown in Fig.1, it is necessary to add new charge/discharge control functions to the conventional SESS. Therefore, the authors propose two types of control function. The proposed functions of the SESS are shown in Fig. 2.

The first of the two functions is to control PV energy charge in the standby mode of the conventional SESS. The SESS is charged when the catenary voltage is higher than the charge starting voltage

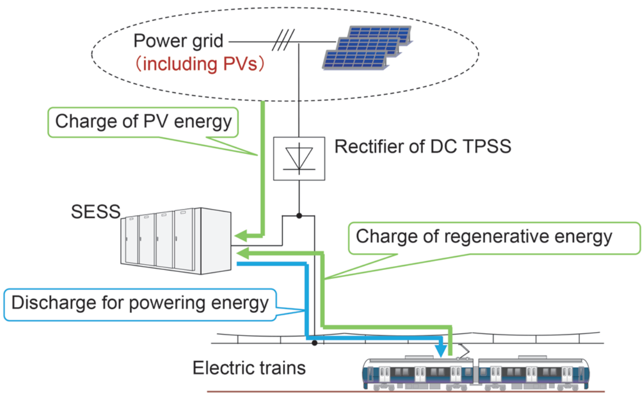

Fig. 1 Application of PVs and SESSs for DC TPSS

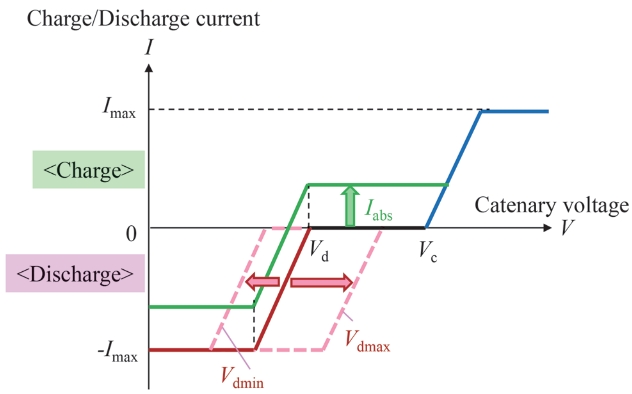

Fig. 2 Proposed charge/discharge control characteristics of SESS for charging PV energy from power grid

“V_c.” On the other hand, the SESS is discharged when the voltage is lower than the discharge starting voltage “V_d.” Furthermore, when the voltage is between “V_c” and “V_d,” the SESS is charged by the target current “I_{abs}.” Note that “I_{abs}” is calculated from the surplus PV energy and the nominal voltage of catenary.

The second function is to adjust state of charge (SOC) for SESS. It is important to control the SOC correctly to get a lot of charge from grid when excess PV power is being produced. The authors propose the changeable discharge starting voltage control depending on the SOC [1]. The target SOCs of SESS are set as SOC(T)* depending on time. “V_d” is increased to get more opportunities of discharge when the current SOC(t) is higher than the target SOC(T)*. The discharge energy is then increased through the control. On the other hand, “V_d” is decreased to cut the chances of discharge when the current SOC(t) is lower than the target SOC(T)*.

2.3 Simulation result of charge/discharge control

The authors studied the proposed control method by using a simulation model [2, 3]. The simulation model of a DC electrified railway line is shown in Fig. 3. All the trains stop at every station on the railway line. Each of the train sets consists of 6 cars. The diagram used in this railway line is the same as that of an actual commuter line. The train operating time treated in this simulation is 24 hours (from 1:00 to 25:00). The nominal voltage of catenary is DC 1,500 V. The line is 38.5 km long with double track and 19 stations. Each TPSS has a 3 MW rated rectifier. Each TPSS receives AC power supply from power grid, and supplies to DC traction power supply system and 6.6 kV 3-phase AC auxiliary trackside loads system. There are two large-scale stations, two medium-scale stations and 15 small-scale stations. The maximum values of load power of the three capacity types are 1,000 kW, 200 kW and 20 kW, respectively. A PV and a SESS are connected to the TPSS 01. The values of rated power of the PV and SESS are 2,000 kW and 3,000 kW respectively. To absorb large generation energy of the PV, the rated energy of the SESS is set for 6,000 kWh, which is much large compared to conventional SESSs. Figure 4 shows an example of the power characteristics for the PV output and the sum of station load. Surplus energy (4.8 MWh) is produced in the daytime since the PV output exceeds the sum of station load. The part of the surplus energy (1.8 MWh) is consumed for the DC traction power supply system. The rest of the surplus energy (3.0 MWh) is required to be suppressed. Such surplus energy can be therefore utilized by applying a SESS to the TPSS 01.

The calculation results of the utilized surplus PV energy and regenerative energy under the following conditions are shown in Fig. 5.

- No SESS in TPSS 01
- Conventional charge/discharge control of the SESS
- Proposed charge/discharge control of the SESS

A comparison of the regenerative energy utilized in the case of conventional charge/discharge control with that of the proposed charge/discharge control is nearly equal. Therefore, the proposed control method does not lead to degraded energy saving. On the other hand, the utilized surplus PV energy by applying the proposed control method is 13% larger than when applying the conventional control method.

The charge/discharge characteristics of the SESSs and the characteristics of the SOC are shown in Fig. 6. It shows that the charge by surplus PV energy contributes to gradual rise of the SOC from 08:00. The target SOC is set 0% after 16:30, therefore the SESS is discharged, and the result of the SOC decreases gradually. The regenerative energy is charged, and the powering energy is discharged by the SESS during the train operation period. The SESS is however constantly charged in the daytime depending on the ordered target current.

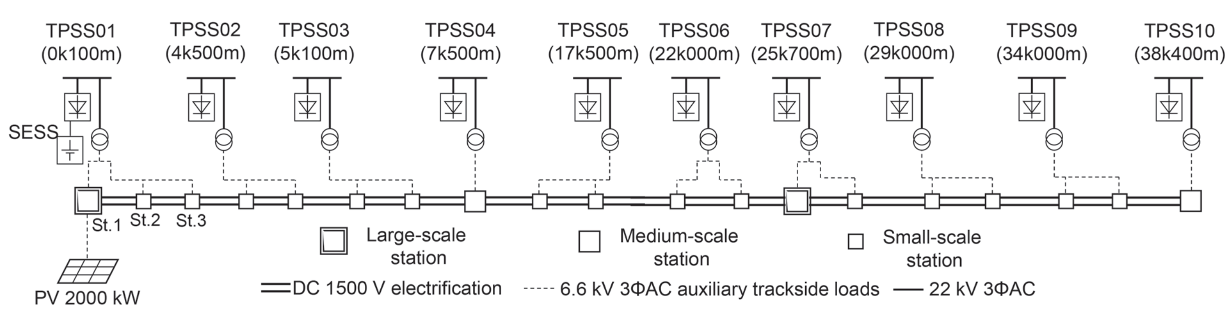

Fig. 3 Simulation model of DC electrified railway with SESSs and PV

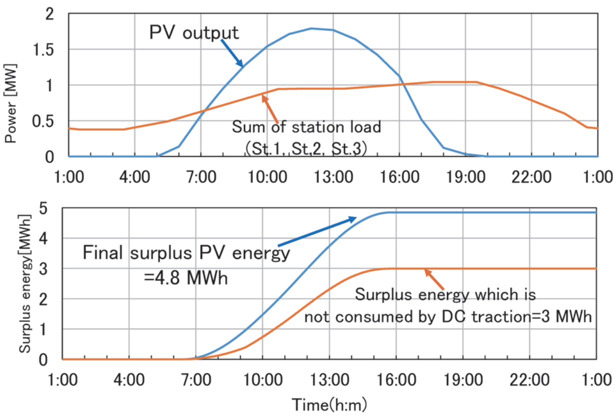

Fig. 4 Surplus energy at TPSS01

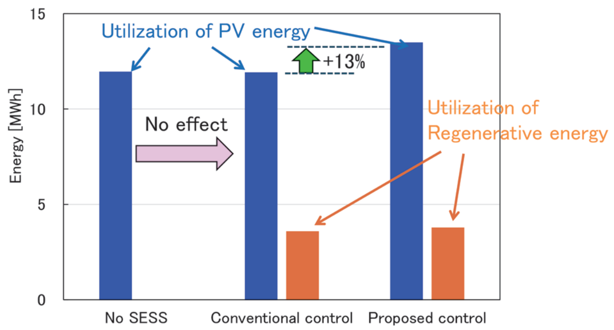

Fig. 5 Effect of utilizing regenerative or surplus PV energy

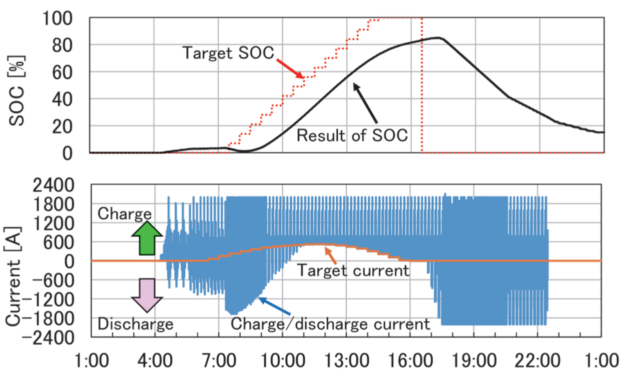

Fig. 6 SOC and current characteristics

3. Integrated control of SESSs and OESSs

3.1 Concept of integrated control

In the previous chapter, each SESS operates individually in accordance with the control shown in Fig. 2. In order to effectively increase charge of surplus PV energy from power grid, it is necessary to comprehensively control all of SESSs. The authors propose an integrated control method of SESSs for DR in accordance with the requirement of a grid manager [4] to contribute to "decarbonization by railways." The concept of the integrated control is shown in Fig. 7. There are two types of DR. One is to increase consumption in DC traction power supply system, which the authors call as "up

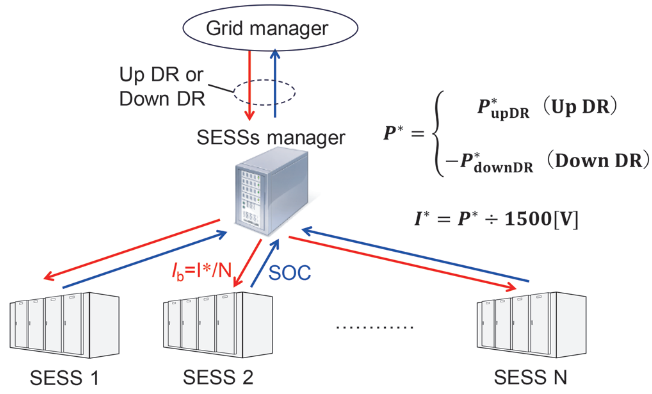

Fig. 7 Concept of integrated control for DR

DR." The other is to reduce consumption in DC traction power supply system, which the authors call as "down DR" in this paper.

The authors propose a concept of "SESSs manager" to realize the proposed control in this paper. The SESSs manager distributes to the charge current I_b to each SESS. "P^*_{upDR}" is the target power of the charge which is sent by the grid manager to the SESSs manager. On the other hand, "P^*_{downDR}" is the target power for reduction which is also sent by the grid manager to the SESSs manager. Note that the polarity of each I_b is set to minus when P^*_{downDR} is set. The target current I_b and the target SOC are the only control information between the SESSs manager and the SESSs. I_b corresponds to I_{abs} shown in Fig.2.

3.2 Expansion to SESSs and OESSs

In this study, the authors propose an "integrated control" system in which an external charging/discharging control is applied to the OESSs [5]. Although the installation locations and capacities of SESSs are known, OESSs move along the railway line and the number of electric trains equipped with OESSs is not constant due to traffic demand, vehicle inspection and other factors. It is therefore necessary to determine the number of available OESSs and to manage their chargeable/dischargeable capacities. Two controllers, the "SESS manager" and the "OESS manager," are used in this study to realize above-mentioned functions. The SESS manager regards the OESS manager to be one virtual SESS and includes the OESS manager in its control.

Figure 8 proposes the concept to add the "OESS manager." The procedure of this control is as follows:

1) The power grid manager sends DR event information such as start time, duration, and target charging/discharging power P_{input} to the SESS manager.
2) The SESS manager and the OESS manager collect the chargeable/dischargeable capacities of their own control targets.
3) The SESS manager distributes the charging/discharging current to the control targets according to (1).

$$I^i_{dist} = \frac{P_{input}}{1500} \times \frac{C^i_{available}}{\sum C^i_{available}} \tag{1}$$

where, I^i_{dist} and $C^i_{available}$ refer to the distributed charging/discharging current and chargeable/dischargeable capacity of the i-th object of management. The target current is converted by dividing the target power by the nominal voltage of 1,500 V.

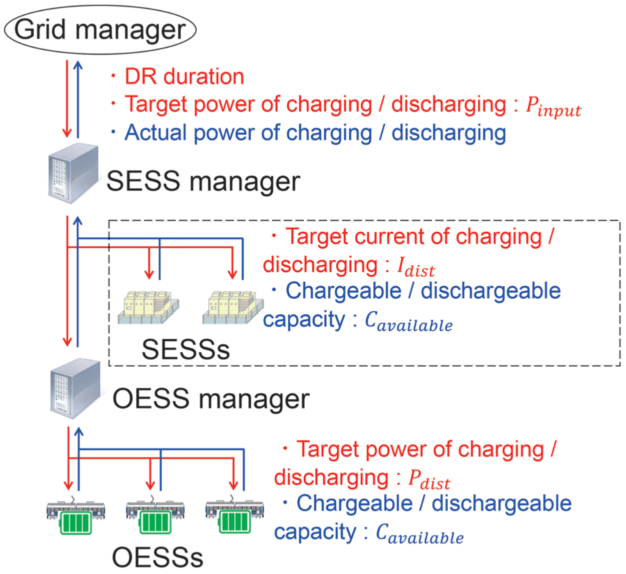

Fig. 8 Concept of integrated control for SESSs and OESSs

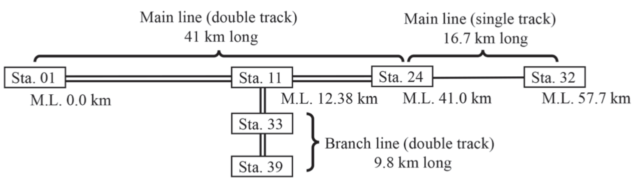

Fig. 9 Simulation model of main line for integrated control

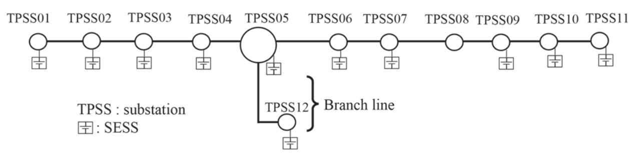

Fig. 10 Simulation model of DC traction power supply system for integrated control

3.3 Simulation of integrated control

Figure 9 shows a schematic diagram of the DC electrified railway line targeted in this study. The nominal OCS voltage is DC 1,500 V. The main line is about 57.7 km long, with double track from station 1 to station 24 and single track from station 24 to station 32. The branch line is about 9.8 km long and is double track. The total number of electric trains is 43, with 39 trains running on the main line and equipped with OESSs. Each of these 39 trains consists of seven cars. The other four trains run on the branch line and do not have OESSs. Each of these trains consists of six cars. Figure 10 shows the location of the traction power supply installation. There are 11 substations and SESSs are installed in three substations as shown in Fig. 10. Tables 1 and 2 show the specifications of the rectifier in the DC substations and those of SESSs and OESSs, respectively.

The period covered by the simulation is 4 hours, from 10:00 to 14:00. In a DR scenario, the authors assumed a condition where the grid manager commands an additional 1,000 kW of demand power from 11:00 to 13:00, in response to excess renewable energy flowing into the power grid. Table 3 shows the details of the DR command. Starting 30 minutes prior to the DR duration, a pre-discharge was carried out at a constant current to increase the chargeable capacities of the SESSs and the OESSs. Then, during the DR duration, the reference power value P_{input} was set to 1,000 kW. For one hour after the DR duration, charging and discharging at a constant current was carried out to restore the respective SOC of the SESSs and the OESSs to their initial values.

The simulation method used is an in-house developed "Train operation power simulator" [6]. The simulation time step is set to 1 second.

Figure 11 shows the total charging/discharging power versus time of the SESSs and the OESSs when a DR command is received. In this figure, the baseline of the total power is increased by 1,000 kW in the DR duration. Figure 12 shows the SOC versus time of each controlled object collected by the SESS manager and the OESS

Table 1 Specification of DC TPSS

Specifications	Value
Nominal voltage [V]	1,500
Rated power [kW]	6,000
Voltage regulation ratio [%]	8
No load voltage [V]	1,620

Table 2 Specification of SESSs and OESSs

Items	Specifications	
	SESSs	OESSs
Usage	Efficiency use of regenerative power	Power source in emergency condition
Number	11	39
Capacity	500 kWh per a SESS	110 kWh per an OESS
Available SOC zone	20% to 80%	10% to 90%
Available capacity	300 kWh per a SESS	88 kWh per an OESS
Initial SOC	50%	90%
Efficiency of charge/discharge	90%/90%	90%/90%

Table 3 Assumed DR command

Duration	Details	
	SESSs	OESSs
10:30 to 11:00	Each SESS discharges 50A until its SOC reaches 30%	Each OESS discharges 50A until its SOC reaches 0%
11:00 to 13:00	P_{input} = 1,000 kW	
13:00 to 14:00	Each SESS discharges 50A until its SOC reaches 50%	Each OESS charges 50A until its SOC reaches 100%

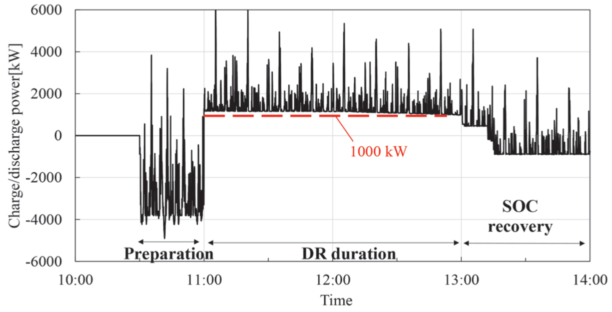

Fig. 11 Charge/discharge power characteristics for integrated control

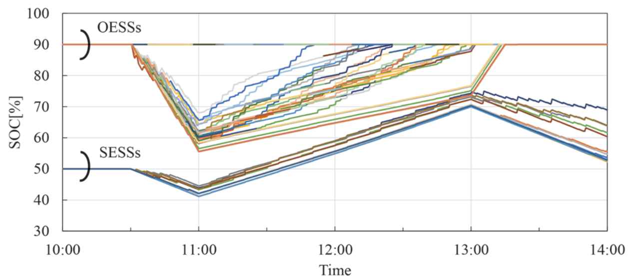

Fig. 12 SOC characteristics for integrated control

manager.

The charge/discharge power fluctuates in a positive direction in Fig. 11, indicating that regenerative power has been charged in all time periods. The total charge/discharge power of all the SESSs and the OESSs exceeds the DR limit of 1,000 kW for most of the two hours. However, SOCs of some OESSs reached the upper limit from 12:00 and the charging capacity of the OESSs gradually decreased. The charge power was finally less than the DR power before 13:00. There is room to improve the DR response by equalizing the variation in the SOC of the SESSs.

Figure 12 shows that the SOC of the SESSs and the OESSs during the DR period changes in accordance with the contents of Table 3. It was confirmed that the SESSs and the OESSs have been charged or discharged in accordance with the demands of the integrated controller.

4. Conclusions

In this study, the authors proposed new SESS control methods for the DC traction power supply system. In addition to these methods, the authors proposed an integrated control method for stationary energy storage systems (SESSs) and onboard energy storage systems (OESSs) on DC electrified railways. The simulation results confirmed that SESSs and OESSs performed charging and discharging approximately as planned by the DR command by using this control method.

Acknowledgment

This work was financially supported in part by the Japanese Ministry of Land, Infrastructure, Transport and Tourism.

References

[1] Oide, T. and Konishi, T., "Controlling Power Demand of Railways to Follow Output Characteristics of PVs Utilizing Large Scale Energy Storage Connected to DC Traction Power Supply System," *IEE-Japan Industry Applications Society Conference*, No. 5-1, pp. 103–106, August 2022 (in Japanese).
[2] Morimoto, H. and Yoshii, T., "Extension of DC traction power supply simulation tool," *J-RAIL2015*, SS 3-4-2506, December 2015 (in Japanese).
[3] Shimizu, K., Ogata, T. and Morimoto, H., "Technical issues related to reproduction of EN 50641 requirements on DC electric traction power supply system simulation," *IEE-Japan*, TER-23-037, MSS-23-003, pp. 13-19, March 2023 (in Japanese).
[4] Konishi, T. and Ogata, T., "Improvement of utilizing Renewable Energy by applying Demand Response Control for Energy Storage System in DC Electrified Railway," *J-RAIL2022*, S7-4-2, December 2022 (in Japanese).
[5] Ogata, T., Saito, T. and Konishi, T., "An Integrated Control Method of Stationary and Onboard Energy Storage Systems in DC Electric Railway," *The Annual Meeting record IEE Japan*, No. 5-213, pp. 367-368, March 2023 (in Japanese).
[6] Ogawa, T., Takeuchi, Y, Morimoto, H., Kageyama, M. and Minobe, S., "Estimation Method of Energy Consumption by Using Train Operation Power Simulator," *IEE Japan Transaction on Industry Applications*, Vol. 141, No. 5, pp. 374-387, May 2021 (in Japanese).

Authors

Takeshi KONISHI, Dr.Eng.
Chief Researcher, Power Supply Systems Laboratory, Power Supply Technology Division
Research Areas: Power Supply

Tamanosuke OIDE
Researcher, Power Supply Systems Laboratory, Power Supply Technology Division (Former)
Research Areas: Power Supply

Takamitsu OGATA
Researcher, Power Supply Systems Laboratory, Power Supply Technology Division (Former)
Research Areas: Power Supply

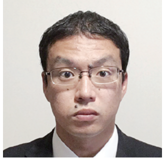

Tatsuhito SAITO, Dr.Eng.
Assistant Senior Researcher, Hydrogen and Sustainable Energy Laboratory, Vehicle Technology Division
Research Areas: Onboard Energy Storage System, Fuel Cell Train

Method for Estimating Molten Volume of Current Collecting Materials at Contact Loss Point using ϕ -θ Theory

Chikara YAMASHITA **Koki NEMOTO** **Takuya OHARA**
Current Collection Maintenance Laboratory, Power Supply Technology Division

In order to control electric wear of current collecting materials such as contact wires and contact strips in electric railways, it is necessary to understand the relationship between current and the molten volume at a contact loss point. In this paper, we propose a method for estimating the molten volume of the contact wire whose film resistance is taken into account, on the basis of the ϕ -θ theory. To verify the proposed method, we carried out wear tests under varying current conditions to measure the molten depth, molten radius, and molten volume. The wear test results showed that the experimental values of the molten volume of the contact wire are spread in the range where normalized potential at the contact boundary at which α was estimated to be 0.90 to 0.94.

Key words: *contact wire, molten bridge, electric potential-temperature parabolic curve, molten volume*

1. Introduction

In electric railways, electric power is supplied to a vehicle through an overhead contact line and a pantograph. Current collecting materials such as the contact wire and the contact strip of pantographs are subject to wear due to the contact forces, sliding speeds and currents. Previous field survey [1] has reported that the wear due to current becomes locally significant at a contact loss point between the contact wire and the contact strip. Since the local wear of the contact wire at the contact loss point is a major issue for maintenance and replacement of the contact wire, it is required to determine an allowable value of current from the viewpoint of wear to suppress the local wear.

Iwase [2] discussed the allowable current of the pantograph from the viewpoint of the temperature rise of the contact wire. However, he pointed out that the local wear of the contact wire is not considered for determination of allowable current of the pantograph. Kono et al [3, 4] and Oda [5] carried out wear tests under current flowing condition and reported that the wear increased by an arc discharge at the time of contact loss. In these wear tests, the wear volume at the time of contact loss was not clarified because there was a mixture of wear in contact and in contact loss. Hayasaka et al [6] reported that a molten bridge is formed between the contact wire and the contact strip before the arc discharge occurs, and that the materials are worn by the scattering of the bridge at the time of the arc discharge. Sasamoto [7] and Kubono et al [8] theoretically discussed the formation of the molten bridge in an ideal condition where there is no film resistance. We think that it is necessary to consider the film resistance in the case of outdoor field conditions such as sliding contact between the contact wire and the contact strip.

Previously, we classified wear modes of current collecting materials due to Joule heat with wear tests under current flowing condition and discussed that the main factor of significant wear of the contact wire should be the molten bridge [9]. In addition, we analyzed a temperature distribution in the vicinity of the contact spot and clarified that the relationship curve between the electric potential and the temperature becomes parabolic [10]. We also formulated the melting condition of the contact wire and the contact strip taking into account the film resistance and proposed a wear mode map due to Joule heat [10].

In this paper, we proposed a method for estimating the molten volume at the contact loss point of the contact wire for which the wear volume can be measured in wear tests under current flowing condition. To verify the method, we carried out wear tests under current flowing condition in a material combination of a hard-drawn copper contact wire and an iron-based sintered alloy contact strip, and compared the estimated value with the experimental value.

2. Method for estimating molten volume

Figure 1 [10] shows an analysis model of the temperature distribution in two contact members under the condition of current flow I [A]. The relationship curve between the electric potential ϕ [V] and the temperature θ [K] along the z axis of the model under the condition of contact voltage V_c [V] becomes parabolic as shown in Fig. 2. We call this curve the electric potential-temperature parabolic curve, and propose a method for estimating the molten volume from this curve. Table 1 shows symbols used in this paper.

The electric potential-temperature parabolic curve shown in Fig. 2 is calculated with (1).

$$\theta=\left[\frac{V_c^2}{L}\left\{\left(\frac{\phi}{V_c}\right)-\left(\frac{\phi}{V_c}\right)^2\right\}+300^2\right]^{1/2} \tag{1}$$

where, L is the Lorenz number (=2.4×10^{-8} [V^2/K^2]). The normalized potential at the contact boundary between the contact wire and the contact strip in Fig. 2 is calculated with (2) [10].

$$\alpha=\frac{\phi_c}{V_c}=\frac{\dfrac{\rho_2}{4a}+\dfrac{\rho_{d2}d_2}{\pi a^2}}{\dfrac{\rho_1+\rho_2}{4a}+\dfrac{\rho_{d1}d_1+\rho_{d2}d_2}{\pi a^2}} \tag{2}$$

where, ϕ_c [V] is the electric potential at the contact boundary, ρ_1, ρ_2 [Ω·m] are electric resistivities, ρ_{d1}, ρ_{d2} [Ω·m] are electric resistivities of the film resistances, d_1, d_2 [m] are film thicknesses. Here, the subscripts 1 and 2 of each constant indicate the contact wire and the contact strip respectively. The radius of the contact spot a [m] is calculated with (3) defined in reference [11].

$$a=\frac{\sqrt{L}\,I\left(\lambda_1+\lambda_2\right)}{8\lambda_1\lambda_2} \tag{3}$$

where, I [A] is the current, λ_1, λ_2 [W/(m·K)] are the heat conductivities.

Table 1 Parameter list used for molten volume estimation [13]

I	Current	[A]	R_{m1}	Electric resistance of molten range of contact wire	[Ω]
V_c	Contact voltage	[V]	R_{m2}	Electric resistance of molten range of contact strip	[Ω]
ϕ	Electric potential	[V]	R	Contact resistance	[Ω]
ϕ_c	Electric potential at contact boundary	[V]	L	Lorentz number	[V^2/K^2]
α	Normalized potential at contact boundary		λ_1	Heat conductivity of contact wire	[W/(m·K)]
β_1	Normalized potential at meting point of contact wire		λ_2	Heat conductivity of contact strip	[W/(m·K)]
β_2	Normalized potential at meting point of contact strip		a	Radius of contact point	[m]
θ	Temperature	[K]	d_1	Thickness of film resistance of contact wire	[m]
T_b	Boiling point	[K]	d_2	Thickness of film resistance of contact strip	[m]
T_{m1}	Melting point of contact wire	[K]	h_1	Molten depth of contact wire	[m]
T_{m2}	Melting point of contact strip	[K]	h_2	Molten depth of contact strip	[m]
ρ_1	Electric resistivity of contact wire	[Ω·m]	r_1	Molten radius of contact wire	[m]
ρ_2	Electric resistivity of contact strip	[Ω·m]	r_2	Molten radius of contact strip	[m]
ρ_{d1}	Electric resistivity of film resistance of contact wire	[Ω·m]	V_1	Molten volume of contact wire	[m^3]
ρ_{d2}	Electric resistivity of film resistance of contact strip	[Ω·m]	V_2	Molten volume of contact strip	[m^3]

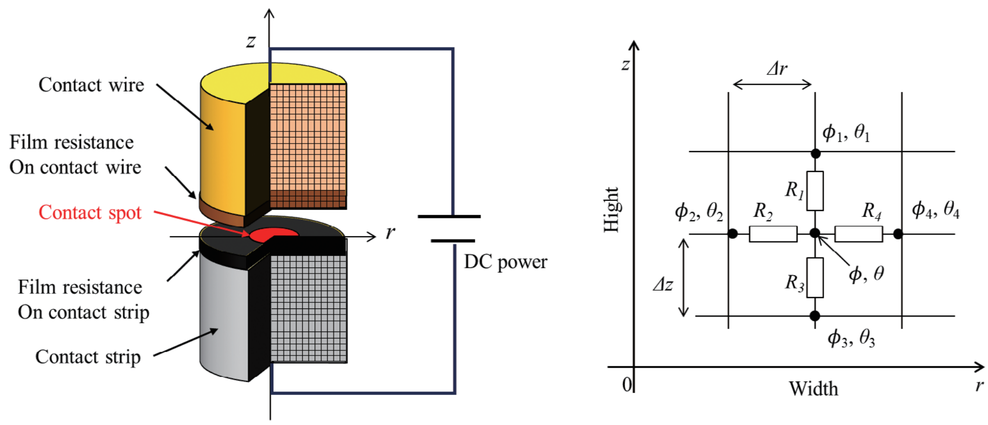

Fig. 1 Analysis model for contact temperature between contact wire and contact strip [10]

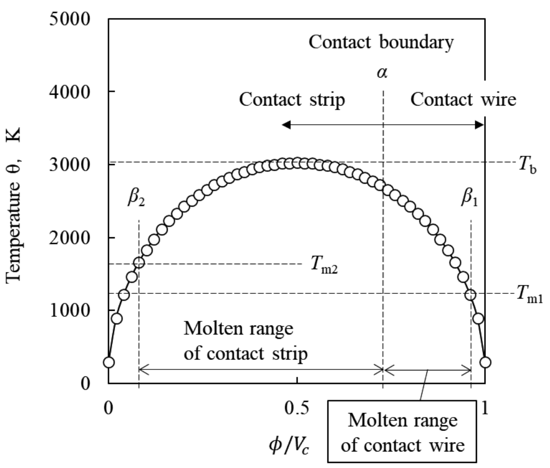

Fig. 2 Electric potential-temperature parabolic curve [10]

The molten bridge of the contact members boils and scatters at the time of arc discharge. At that time, the maximum temperature of the electric potential-temperature parabolic curve should be consistent with the boiling point of the member. Therefore, the contact voltage at the time arc discharge is calculated with (4) on the basis of the ϕ-θ theory [12].

$$V_c=\left[4L\left(T_b^2-300^2\right)\right]^{1/2} \tag{4}$$

where, T_b [K] is the boiling point of the member in which the maximum temperature occurs. If the temperature of the electric potential-temperature parabolic curve exceeds the melting points of the contact wire and the contact strip, the molten range of a member is consistent with the range between α and β_1, β_2 which are the normalized potentials corresponding to the melting points of each member. Normalized potentials β_1, β_2 are calculated with (5) and (6) by substituting T_{m1}, T_{m2} [K] which are the melting points of the contact wire and the contact strip into (1).

$$\beta_1=\frac{1}{2}+\frac{1}{2V_c}\sqrt{V_c^2-4\left(T_{m1}^2-300^2\right)L} \tag{5}$$

$$\beta_2=\frac{1}{2}-\frac{1}{2V_c}\sqrt{V_c^2-4\left(T_{m2}^2-300^2\right)L} \tag{6}$$

Next, the molten depths are calculated as the distance between the contact boundary and the molten range as follows. It is assumed that the molten range is along the equipotential surface as shown in Fig. 3. Each electric resistance R_{m1}, R_{m2} [Ω] between α and β_1, β_2 is calculated with (7) and (8) on the basis of Holm [12].

$$R_{m1}=\frac{\rho_1}{2\pi a}\arctan\frac{h_1}{a} \tag{7}$$

$$R_{m2}=\frac{\rho_2}{2\pi a}\arctan\frac{h_2}{a} \tag{8}$$

where, h_1, h_2 [m] are the molten depths from the contact boundary. Since the current I does not change in the contact members, β_1, β_2 are calculated by dividing (7) and (8) by the whole contact resistance R [Ω] and α. Then, h_1, h_2 are calculated with (9) and (10).

$$\begin{aligned}\beta_1&=\alpha+\frac{R_{m1}}{R}=\alpha+\frac{2}{\pi}(1-\alpha)\arctan\frac{h_1}{a}\\ h_1&=a\tan\frac{\pi}{2}\left(\frac{\beta_1-\alpha}{1-\alpha}\right)\end{aligned} \tag{9}$$

$$\begin{aligned}\beta_2&=\alpha-\frac{R_{m2}}{R}=\alpha-\frac{2\alpha}{\pi}\arctan\frac{h_2}{a}\\ h_2&=a\tan\frac{\pi}{2}\left(\frac{\alpha-\beta_2}{\alpha}\right)\end{aligned} \tag{10}$$

Since the molten radius is different from the radius of the contact spot and the shape of an isothermal surface is spheroid as shown in Fig. 3, the molten radii of each member r_1, r_2 [m] are calculated with (11) and (12).

$$r_1=\sqrt{a^2+h_1^2} \tag{11}$$

$$r_2=\sqrt{a^2+h_2^2} \tag{12}$$

The molten volumes of each member V_1, V_2 [m^3] when current flows through a contact spot are calculated with (13) and (14) by regarding the molten range as a semi-elliptical sphere.

$$V_1=\frac{2\pi}{3}r_1^2h_1 \tag{13}$$

$$V_2=\frac{2\pi}{3}r_2^2h_2 \tag{14}$$

The molten radius r [m] and the molten depth h [m] are functions of the contact radius a [m] as shown in (9) - (12), and the contact radius is a function of the current I [A] as shown in (3).

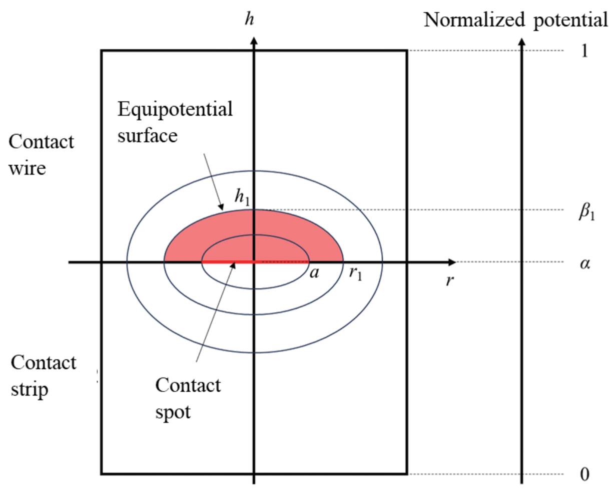

Fig. 3 Molten range along equipotential surface [14]

Therefore, the molten volumes V [m^3] calculated in (13) and (14) are functions proportional to the cube of the current I [A].

3. Verification of the proposed method by testing Method for estimating molten volume

3.1 Wear test apparatus and test conditions

The proposed method calculates the molten volume at the time of contact loss, i.e. when the contact members of the contact wire and the contact strip open. The method was then verified using the high-speed wear tester for current collecting materials shown in Fig. 4. In this apparatus, a real contact wire is installed on a disk and a contact strip specimen is pushed against the disk for current collection. The diameter of the disk is 2 m, and the circumference of the disk is 6.3 m. The method for estimating the molten volume uses the ϕ-θ theory used in steady state, so it is necessary that the sliding speed should be set as low as possible during the verification test. Since the fluctuation of contact force in this apparatus is larger than that in the linear wear tester which is reported in [9], arc discharge frequently occurs even at low sliding speed. In addition, since a larger current is able to set in this apparatus, it is expected to obtain effective results for determination the allowable current. From the above, we think that this apparatus is appropriate for the verification test.

Table 2 shows the material properties of the hard-drawn copper contact wire and the iron-based sintered alloy contact strip. In Table 2, the boiling points of each material are regarded as those of the base materials such as copper and iron [11]. Table 3 shows the test conditions. The verification test was carried out after running-in at a sliding speed condition of 300 km/h without current to suppress partial contact of the contact strip. The sliding surface of the contact

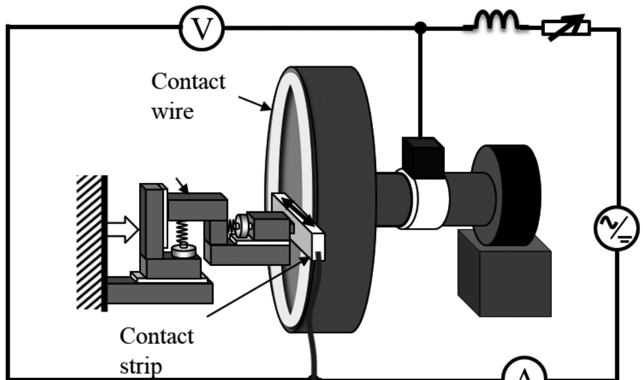

Fig. 4 Schematic image of wear test apparatus [13]

Table 2 Test specimens [13]

	Contact wire	Contact strip
Material	Hard-drawn copper	Iron-based sintered alloy
Melting point, K	1,334	1,646
Boiling point, K[11]	2,853	3,027
Electric resistivity, Ωm	1.77×10^{-8}	0.40×10^{-6}
Heat conductivity, W/mK	373	25.3

Table 3 Test conditions [13]

Contact force, N	Approximately 50
Sliding speed, km/h	5
Current, A	100, 200
Sliding time, s	～60

wire was ground before the verification test to remove the transfer layer on the contact wire. The contact force of the contact strip was set to 50 N which is close to the contact force of a pantograph. The sliding speed was set to 5 km/h which is the lowest speed of this apparatus. The current was set to 100 A and 200 A. Since the molten spot of the contact wire was too small to be observed at a current below 100 A, we set the current to 100 A or higher. In order to preserve the molten spot and to measure its radius and depth, the test was stopped and the contact strip was unloaded when several arc discharges were observed. The radius and the depth of the molten spot only of the contact wire were measured after the test. The reason for this is that the molten spot of the contact strip was damaged by additional friction and another arc discharge because the contact strip continued to slide in the same surface during the test.

After the test, the section profile around the molten spot of the contact wire was measured several times with a roughness meter (Mitsutoyo, SJ-310, load: 0.75 mN, distance: 5 mm). Figure 5 shows an example of the measured profile around the molten spot. The sliding surface was regarded as the reference surface, and the maximum depth of the molten spot from the reference surface was measured. Since the shape of the molten range was assumed to be spheroid as described above, the maximum value among several measurements was adopted as the molten depth. On the other hand, the molten spot was observed by a microscope (Keyence, VHX-100, lens: 175x). Figure 6 shows an example of the microscopic image of the molten spot. Although there were some cases where the molten spots were not perfect circular because of scattering of the molten copper and additional friction, the radius of the molten spot was measured by fitting a circle to three points on the circumference of the spot. The molten volume of the spot was calculated with (13) by substituting the measured depth and radius.

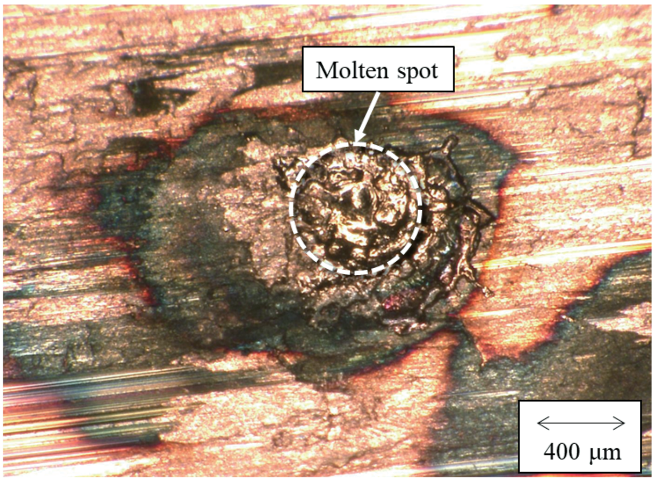

Fig. 6 Example of microscopic image of a molten spot [13]

3.2 Wear test results

Figure 7 shows a comparison of the experimental and the estimated values of the molten depth under varying current. The estimated values were calculated up to a current of 300 A because the current condition of iron-based sintered alloy contact strips used in Shinkansen trains is approximately 300 A. The boiling point of the contact strip is used for T_b in (4). The reason is that in the case of the combination of the hard-drawn copper contact wire and the iron-based sintered alloy contact strip, the maximum temperature in the electric potential-temperature parabolic curve would appear in the contact strip side because the normalized potential at the contact boundary α is thought to be 0.5 or more.

From Fig. 7, it is found that the estimated values increase as the value of α decreases, and the experimental values are in the range where α is estimated to be 0.90 to 0.94. The value of α in no film resistance condition is calculated to be 0.96 from (2) and Table 2. The decrease of α from 0.96 indicates an increase in the film resistance of the contact wire because it is unlikely that the resistivity of the contact strip decreases. In addition, the estimated value of the molten depth became negative at α of 0 .96. The reason for this is that the maximum temperature of the contact wire in the electric potential-temperature parabolic curve at the time of contact strip

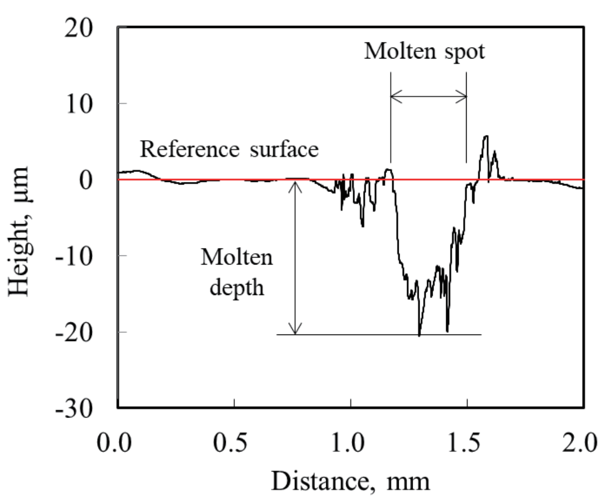

Fig. 5 Example of cross-sectional profile of a molten spot [13]

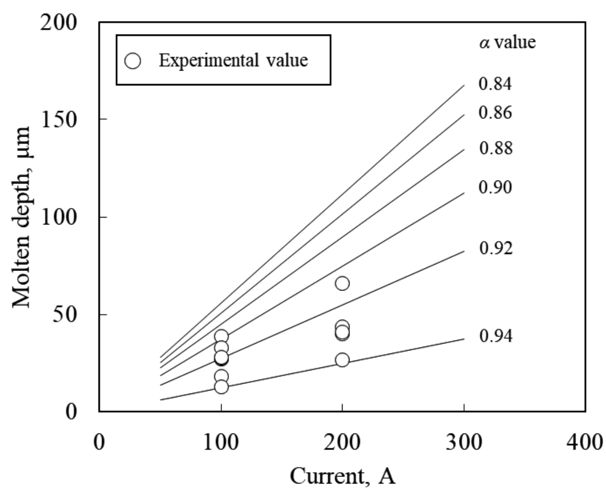

Fig. 7 Experimental and estimated values of molten depth of contact wire [13]

boiling is lower than the melting point of the wire T_{ml}. In this case, it means that the contact wire does not melt even when arc discharge occurs in no film resistance condition.

Figure 8 shows a comparison of the experimental and the estimated values of the molten radius under varying current. It is found that the estimated values increase as the value of α decreases, but the influence of α on the estimated radius is not as great as that on the estimated depth. Although some of the experimental values are out of the estimated range, we think that the trend of the increasing melt radius and the order of the values are generally consistent with the estimation. It should be noted that the experimental depths are in the range where α is estimated to be 0.90 to 0.94 as shown in Fig. 7, but some experimental radii are in the range where α is estimated to be 0.84 or less as shown in Fig. 8. Hayasaka [6] reported that the scattered volume was 1/5 -1/100 of the molten volume at the time of arc discharge. From (11) - (14), since the molten radius is also a function of the molten depth, the molten volume is proportional to the cube of the molten depth. In this case, it is thought that the experimental depth is 1/2 -1/5 of the true molten depth. In Fig. 7, if the true molten depth is twice the experimental value, some of them should be in the range where α is estimated to be 0.84 or less. Then the tendency of the molten depth would be similar to that shown in Fig. 8.

Figure 9 shows the experimental and the estimated values of the molten volume under varying current. As mentioned in Chapter 2, the relationship between the current and the estimated molten volume is not liner, but the molten volume is proportional to the cube of the current. And it is also found that the estimated values increase as the value of α decreases, and the experimental values are in the range where α is estimated to be 0.84 to 0.94. As mentioned above, it is quite possible that the true molten volume is larger than the experimental value because not all of the molten portions were scattered. Therefore, when considering the wear of the contact wire, it is necessary to take into account the softening of the remaining molten portions.

These tests have not verified the validity of α because the film resistance of the contact wire was not measured. Since the tests were carried out immediately after the surface of the contact wire was ground, it is unlikely that there was a large film resistance on the contact wire. Therefore, it is reasonable that the experimental values are in the range where α is close to 0.96.

We think that it is useful to formulate the molten volume of the contact wire and confirm the consistency between the estimated value and the experimental value. On the other hand, this proposed method of estimating the molten volume is applicable only under the low sliding speed condition close to the steady state where the ϕ-θ theory holds. Therefore, in order to use this method in the railway field, it is necessary to improve the method so that the molten volume can properly be estimated under the unsteady state such as the high sliding speed condition. In the future, the estimation of the molten volume of the current collecting materials due to Joule heat without using the sliding speed, will contribute to the innovation of maintenance, such as the prediction of wear in usage conditions and the determination of the allowable contact loss ratio in usage current. In addition, it contributes to the determination of the allowable current of pantographs.

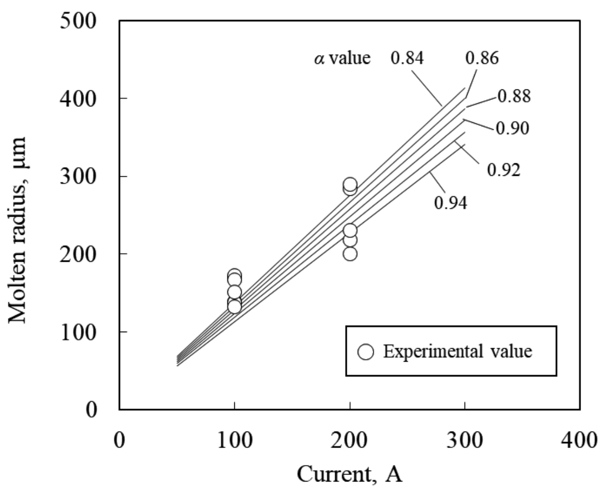

Fig. 8 Experimental and estimated values of molten radius of contact wire [13]

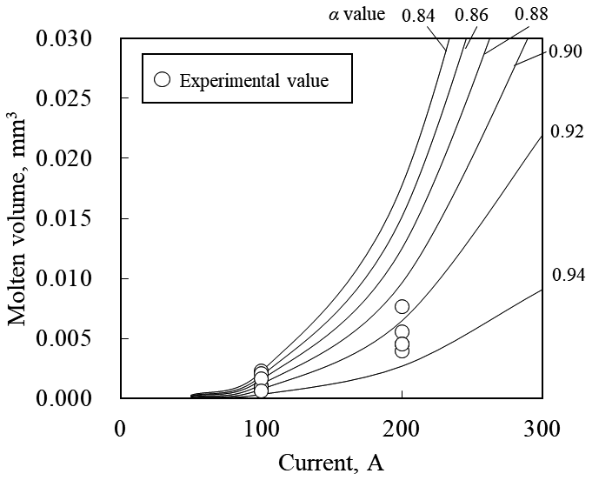

Fig. 9 Experimental and estimated values of molten volume of contact wire [13]

4. Conclusions

In order to estimate the molten volume of the contact wire at the contact loss point, we focused on the relationship between the electric potential and the temperature in the vicinity of the contact spot to propose a method for estimating the molten volume taking into account the film resistance. In addition, we carried out verification tests and measured the molten volume at the contact loss point. The results obtained in this study are as follows.

(1) Using the electric potential-temperature parabolic curve in the vicinity of the contact spot, we determine the area enclosed by the electric potential corresponding to the melting point and that corresponding to the contact boundary. Then the estimation formulas of the molten volume are proposed by estimating the molten depth and radius at the time of contact boiling.
(2) The estimated results show that the molten depth and the molten radius are proportional to the current, and the molten volume is proportional to the cube of current. In addition, the results also show that the molten volume of the contact wire increases as the normalized potential α, which is the contact boundary in the electric potential-temperature parabolic curve, decreases.
(3) The experimental results show that the measured values of the molten volume of the contact wire were spread the range where α is estimated to be 0.90 to 0.94. In the experiment, the true molten volume was thought to be larger than the measured value because not all of the molten volume was scattered, but the mag-

nitude and tendency of the measured values are generally consistent with the estimated value.

(This paper is the updated version of the reference [13] [14].)

References

[1] Iwase, M., "Current Collecting by the Pantograph and its Wear (I)," *Railway Technical Research Report*, No. 53, 1959 (in Japanese).

[2] Iwase, M., "Capacity of Overhead Wire and Current-Collecting Capacity of Pantograph," *Railway Technical Research Document*, Vol. 14, No. 1, pp. 283-287, 1957 (in Japanese).

[3] Kohno, A. Ohyabu, H. and Soda, N., "Effect of Discontact Arc on Wear of Materials for Current Collection (Part 1)," *Journal of Japan Society of Lubrication Engineers*, Vol. 27, No. 4, pp. 283-287, 1982 (in Japanese).

[4] Kohno, A., Ohyabu, H. and Soda, N., "Effect of Discontact Arc on Wear of Materials for Current Collection (Part 2)," *Journal of Japan Society of Lubrication Engineers*, Vol. 27, No. 7, pp. 527-532, 1982 (in Japanese).

[5] Oda, O., "Study on Wear of Contact Wire and Contact Strip on Shinkansen," *Railway Technical Research Report*, No. 1323, 1986 (in Japanese).

[6] Hayasaka, T., Akagi, Y., "Influence of Arc Discharge on the Surface of a Contact Wire," *IEEJ Transactions on Industry Applications*, Vol. 135, No. 4, pp. 327-334, 2015.

[7] Sasamoto, T., "The Theoretical Analysis of Bridge Transfer of the Opening Contacts," *IEICE Transactions on Electronics*, J58-C, 3, pp. 101-108, 1975 (in Japanese).

[8] Kubono, T. and Suzuki, J., "A Theoretical Investigation of the Dimension of Molten Metal Bridge and Its Transfer," *IEICE Transactions on Electronics*, J63-C, 10, pp. 667-674, 1980 (in Japanese).

[9] Yamashita, C., Adachi, K., "Influence of Current on Wear Modes and Transition Condition of Current Collecting Materials," *Journal of Japanese Society of Tribologist*, Vol. 58, No. 7, pp. 496-503, 2013 (in Japanese).

[10] Yamashita, C., Adachi, K., "Wear Mode Map of Current Collecting Materials," *Journal of Japanese Society of Tribologist*, Vol. 62, No. 2, pp. 129-136, 2017 (in Japanese).

[11] Takagi, T., *Arc Discharge Phenomena of Electric Contacts*, Corona, pp. 56-67, 1995 (in Japanese).

[12] Holm, R., *Electric Contacts: Theory and Applications, 4th ed.*, Springer, pp. 64-68, 2000.

[13] Yamashita, C., Nemoto, K., Ohara, T., "Estimation Method of Melting Volume of Current Collecting Materials under Current Flowing Condition in Electric Railway," *Journal of Japanese Society of Tribologist*, Vol. 67, No. 5, pp. 366-372, 2022. (in Japanese).

[14] Yamashita, C., Nemoto, K., Ohara, T., "Estimation Method of Melting Volume of Current Collecting Materials at Contact loss Point by using Theory," *RTRI Report*, Vol. 38, No. 7, pp. 23-28, 2024. (in Japanese).

Authors

Chikara YAMASHITA, Ph.D.
Senior Chief Researcher, Head of Current Collection Maintenance Laboratory, Power Supply Technology Division
Research Areas: Overhead Contact Line, Tribology, Electric Contact, Fatigue

Koki NEMOTO
Researcher, Current Collection Maintenance Laboratory, Power Supply Technology Division
Research Areas: Overhead Contact Line, Tribology

Takuya OHARA
Assistant Senior Researcher, Collection Maintenance Laboratory, Power Supply Technology Division
Research Areas: Overhead Contact Line, Fatigue

PAPER

A Simple Method for Predicting Track Settlement Caused by Culvert Pipe Damage

Takashi NAKAYAMA **Yu OHARA** **Akihiko MIWA**
Tunnel Engineering Laboratory, Structures Technology Division

Takaki MATSUMARU
Foundation & Geotechnical Engineering Laboratory, Structures Technology Division

In this study, we developed a nomogram to easily predict track settlement due to culvert pipe damage. First, a calculation method was developed to estimate the reduction ratio of the subgrade reaction coefficient under railway tracks. The accuracy of this method was verified by comparison with trap-door tests and field tests. Secondly, to produce the nomogram, we calculated track displacement under conditions of reduced subgrade reaction.

Key words: *maintenance, culvert pipe, embankment*

1. Introduction

In railway embankments, small-diameter ceramic pipes are buried divert the water source around or under the track. If these culvert pipes are damaged (Fig. 1), the surrounding ground may become loose. There is a possibility that the subgrade reaction force under the track will decrease, leading to settlement of the track (Fig. 2).

To ensure safe train operation, railway operators regularly need to inspect and repair culvert pipes. However, this work is time-consuming because there are many culvert pipes in railway embankments, often hidden in the grass (Fig. 3).

In this study, we developed a nomogram to easily predict track settlement caused by culvert pipe damage (Fig. 4). By plotting the pipe diameter and depth on this nomogram, railway operators can understand the degree of track settlement. This information helps to determine more accurately the priority and frequency of inspections of the culvert pipes. First, we developed a calculation method to estimate the reduction ratio of the subgrade reaction coefficient under railway tracks when a culvert pipe is damaged. The accuracy of this method has been verified through laboratory tests and field tests. Secondly, we used this method to calculate track settlement under various conditions and prepared a nomogram by aligning these calculation results with track management values.

Fig. 1 Inside damaged culvert pipe

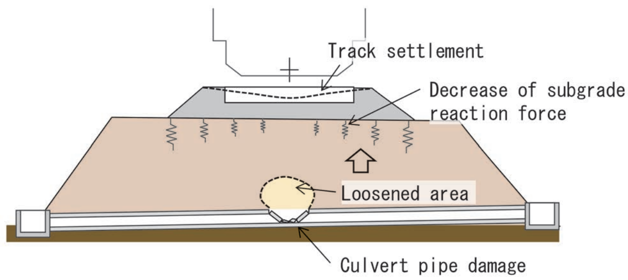

Fig. 2 Track settlement caused by culvert pipe damage

Fig. 3 Inspection of culvert pipe

2. Method for calculating the reduction ratio of subgrade reaction coefficient under track

2.1 Assumptions and calculation steps

The calculation method created in this study is shown in Fig. 5, and the calculation steps are as follows:

Step 1: Divide the ground into two layers at the top of the loosened area (layer1 below the boundary and layer2 above the boundary). It is assumed that the height of the loosened area is equal to the diameter of the pipe.

Step 2: Assuming there is a ground surface beside the pipe, calculate the reduction ratio (λ) of the ground reaction coefficient on the top surface of Layer 1. The reduction ratio (λ) is calculated using a method for designing foundations near slopes, as described in the 'Design Standards and Commentary for Railway Structures (Foundation Structures)'[1]. In this method, the ultimate bearing capacity near the slope and on level ground is calculated and their ratio is used as a reduction factor for the ground reaction coefficient (k). In this study, we calculated the ultimate bearing capacity of ground surfaces on level ground and used their ratio as the reduction ratio (λ).

Step 3: With stress propagating at an angle of 30 degrees from

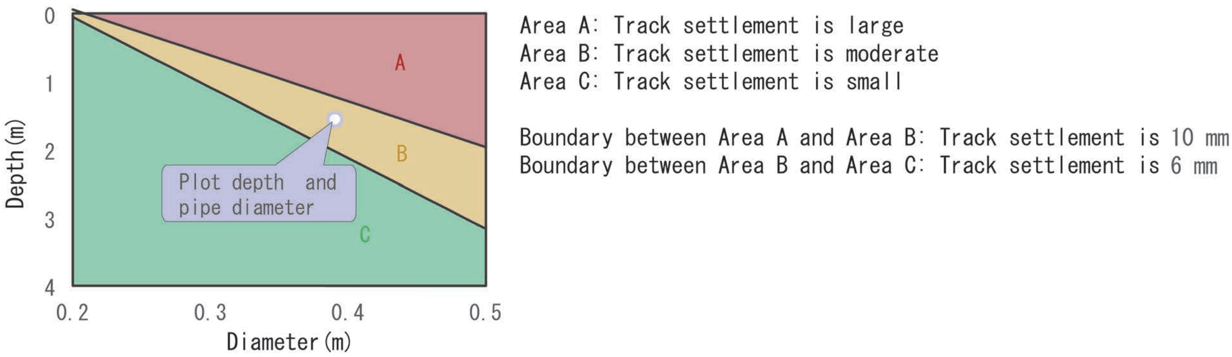

Fig. 4 Nomogram to predict the degree of track settlement due to culvert pipe damage.

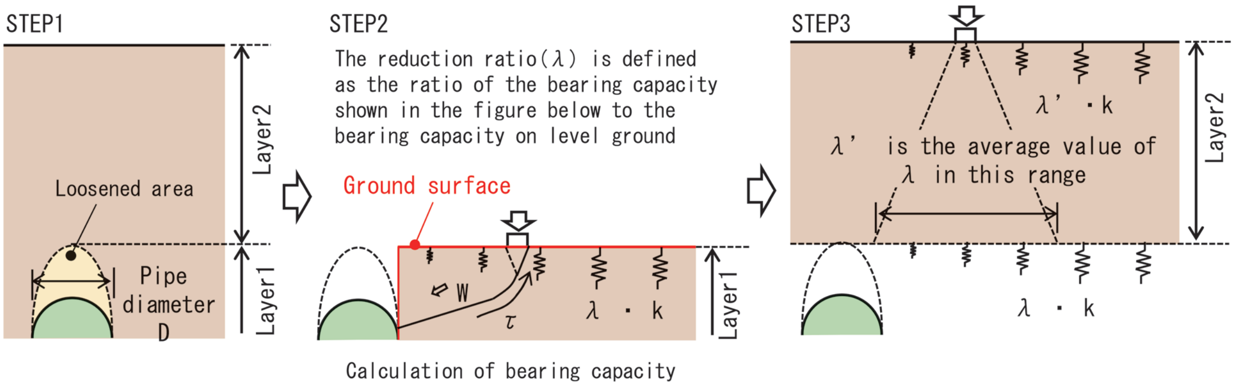

Fig. 5 Calculation steps of the reduction rate of subgrade reaction coefficient

the edge of a sleeper in Layer 2, calculate the average reduction ratio (λ') on the top surface of Layer 2.

2.2 Comparison of trap-door test and the calculation method of reduction ratio

To verify the accuracy of the calculation method shown in Fig. 5, we conducted a model experiment known as a 'trap-door test' and carried out simulation analysis using the calculation method. The trap-door test is a geotechnical model test used to study the behavior of soil and structures under specific conditions. In this test, a model ground is constructed within a soil tank, and a portion of the tank floor, referred to as the 'trap door,' is gradually lowered. This test has been widely used to simulate ground loosening caused by tunnel excavation. In this study, we simulated ground conditions after culvert pipe damage, with a semi-circular culvert pipe fixed on top of the trap door that was gradually lowered.

The experimental apparatus is shown in Fig. 6, and the test procedure is detailed in Fig. 7. The ground material used was dry silica sand No. 7, compacted to achieve a target relative density of 70%. We carried out trap-door tests by varying the overburden.

Figure 8 shows the relationship between the horizontal distance from the center of the culvert pipe and the reduction ratio of the subgrade reaction coefficient. It can be seen that these results are generally in agreement with each other.

2.3 Comparison of field test and the calculation method of reduction ratio

Field tests were carried out at three sites where culvert pipe collapses were observed using a borehole camera. The internal strength of the ground was measured using a surface wave exploration test, and a portable falling weight deflectometer (FWD) test was carried out to measure the distribution of the ground reaction coefficient on the ground surface.

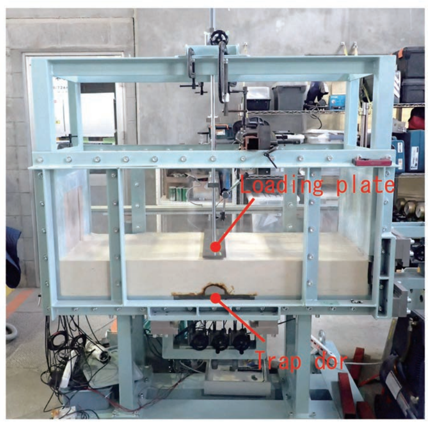

Fig. 6 Experimental equipment

At two of these sites with higher shear wave velocity, the ground reaction coefficient did not decrease above the culvert pipe. On the other hand, at the site with lower shear wave velocity compared to the other two sites, the ground reaction coefficient decreased above the culvert pipe. The detailed results of these investigations for one of the higher shear wave velocity sites (Site 1) and the lower shear wave velocity site (Site 2) are described in the next section.

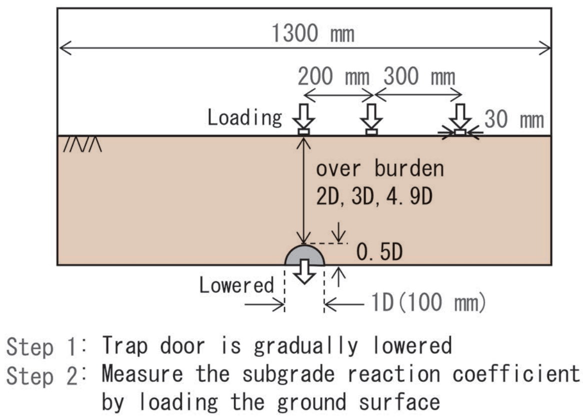

Fig. 7　Experimental method

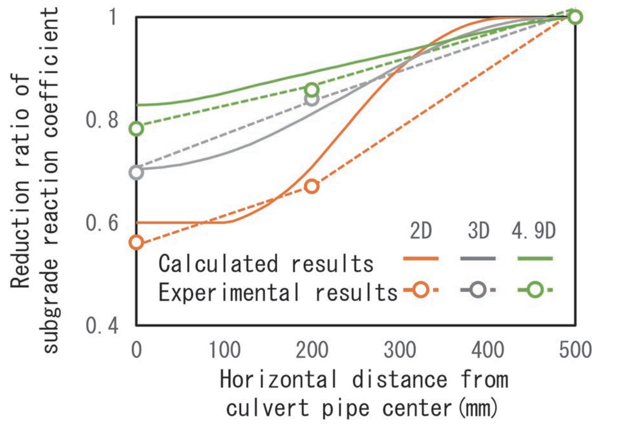

Fig. 8　Comparison of experimental results with calculated values

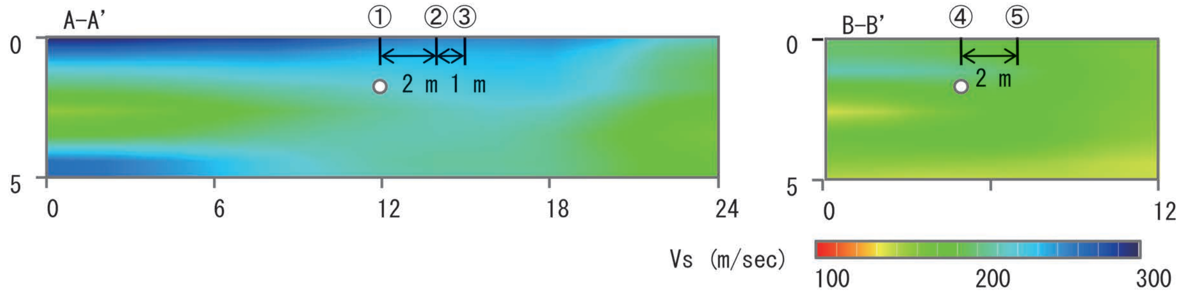

Fig. 9　Distribution of shear wave velocity (Site 1)

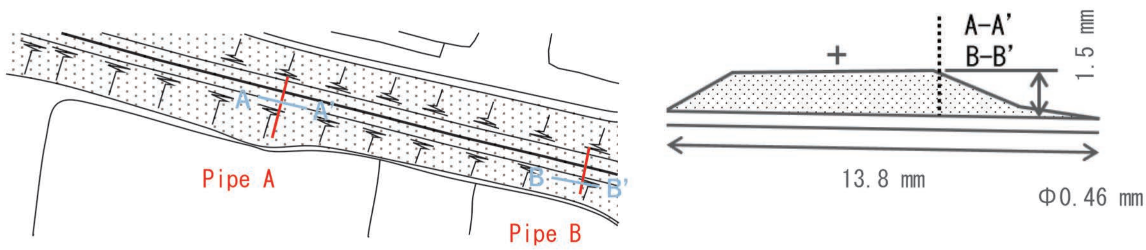

Fig. 10　Culvert pipe location (Site 1)

Table 1　Result of portable FWD test (Site 1)

	①	②	③	④	⑤
K30 (MN/m³)	69.0	71.1	67.4	80.7	81.0

2.3.1 Test results of site 1

Figure 9 shows the results of the surface wave exploration test carried out along lines A-A' and B-B' (Fig. 10). The results indicate that a layer with high shear wave velocity is distributed near the ground surface. Table 1 shows the results of the portable FWD test, where significant differences were not observed above the culvert pipe. The K30 values were approximately 70 - 80 MN/m³, meeting the requirements specified in the 'Design Standards for Railway Structures and Commentary (Earth Structures)'[2].

2.3.2 Test results of site 2

There are also two culvert pipes: Pipe A, which has a large soil cover, and Pipe B, which has a small soil cover (Fig. 11). Since this is an abandoned railway line, the track and facilities have been removed.

Figure 12 shows the results of the surface wave exploration test. These results indicate that a layer with low shear wave velocity is distributed near the ground surface, and that Pipe B is located within this layer. Table 2 shows the results of the portable FWD test. It can be seen that the K30 value is lower above Pipe B. The value at point 1 was approximately 70% lower than the value at point 3. This result indicates that the impact of the pipe B damage appeared on the ground surface due to the weak soil conditions.

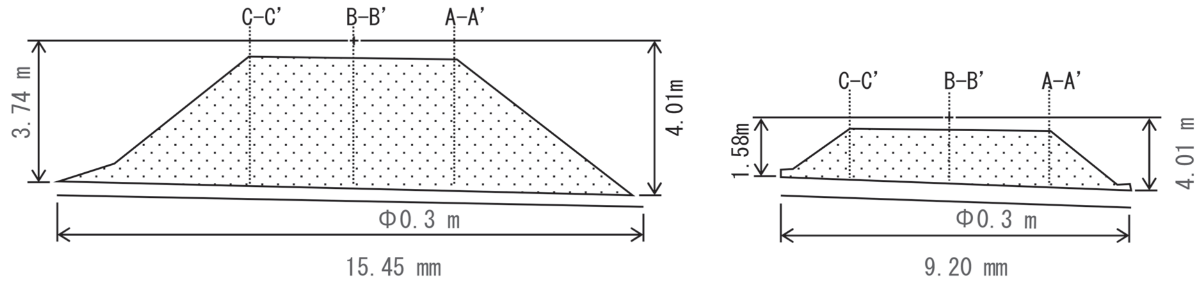

(a) Pipe A (b) Pipe B

Fig. 11 Culvert pipe Location (Site 2)

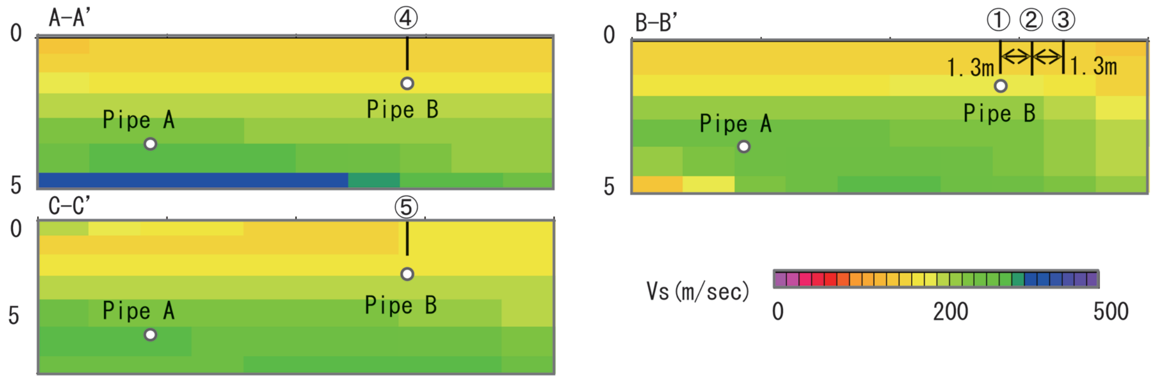

Fig. 12 Distribution of elastic wave (Site 2)

Table 2 Result of portable FWD test (Site 2)

	①	②	③	④	⑤
K30 (MN/m³)	30.3	84.6	104.5	167.1	176.7

2.3.3 Calculation of reduction ratio of subgrade reaction coefficient

Figure 13 shows the relationship between the field test results (Pipe B at Site 2, where a decrease in the ground reaction coefficient was observed) and the calculated values. It is apparent that the calculated values are about 10-20% smaller. For other field test results where the ground reaction coefficient did not decrease, the calculated values showed that the ground reaction coefficient ratio above the culvert pipe was also approximately 20% smaller.

The result was that the calculation method can safely estimate the reduction ratio of the ground reaction coefficient in the field.

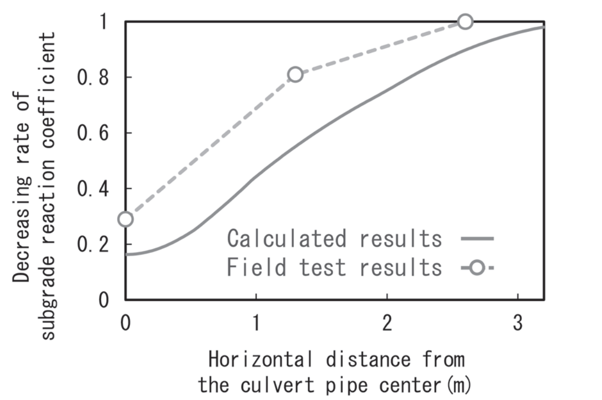

Fig. 13 Comparison of field test results with calculated values

3. Nomogram production

Figure 14 shows the calculation conditions used to produce the nomogram. The train load was assumed to be in accordance with EA-17 and a crossing angle of 30° between the track and the culvert pipe was taken into account. Although actual culvert damage would be partial, it was assumed that the pipe was completely damaged.

The limit values for track settlement were set at two levels: Limit 1 is set at 6 mm, which is 0.4 times the standard track management value of 15 mm for conventional lines (Class 1, vertical displacement, static value). Limit 2 is set at 10 mm, which is 0.7 times the standard value.

The coefficient of subgrade reaction of the original ground is calculated using the K30 value (70 MN/m³) required for railway embankment Performance Rank II, which is commonly used for conventional lines. The types of soil used in the calculations are shown in Table 3. The cohesion and internal friction angle for the calculations were determined from triaxial compression test results using samples extracted from the existing embankment (Fig. 15).

Table 4 shows examples of the nomogram produced for different ground conditions. The nomogram categorizes the impact as

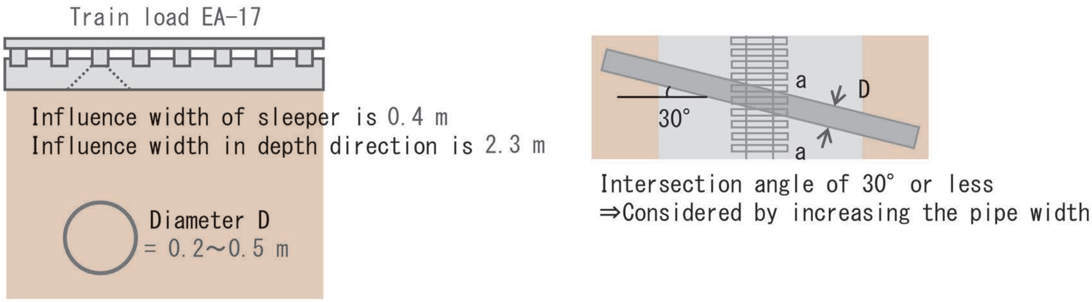

Fig. 14 Calculation conditions

Table 3 Soil classification

Types of soil	Category	γt (kN/m³)
Soil 3 (sand and gravel with poor particle size distribution, sandy soil, etc.)	GF, GF-S, GFS SF, SF-G, SFG	16
Soil 4 (cohesive soil, etc.)	ML, CL, MH, CH OL, OH, OV, Pt, Mk VL, VH1, VH2	14

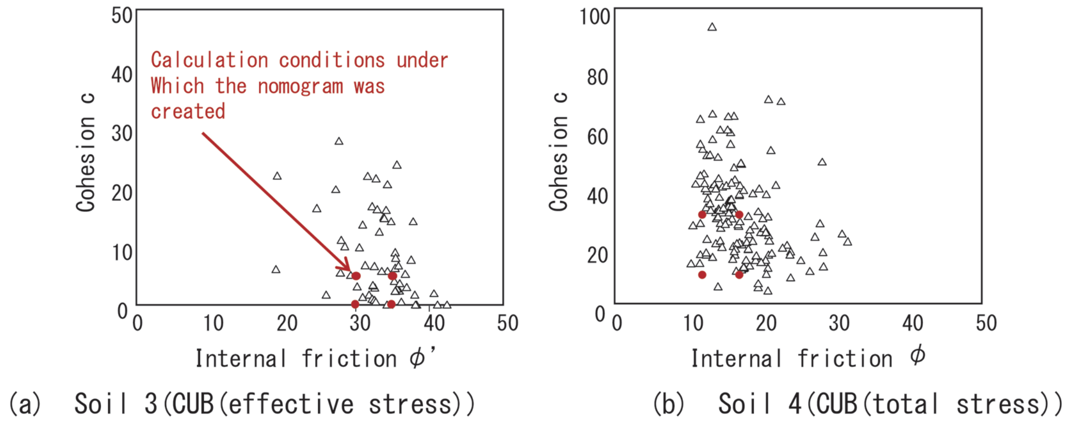

Fig. 15 Internal friction angle and cohesion

small if it is below Limit 1, medium if it is between Limit 1 and Limit 2, and large if it is above Limit 2. In all cases, the larger the pipe diameter or the shallower the depth, the greater the impact on the track. It is also clear that a lower cohesion and internal friction angle will result in a larger area of high impact.

Additionally, since the cohesion and internal friction angle of the embankment are often unknown in the field, a consolidated nomogram is produced (Fig. 3).

4. Conclusions

The results obtained from this study are summarized as follows:

(1) As a result of comparative verification with model experiments, it was confirmed that the calculation method developed in this study is applicable for calculating the distribution of the subgrade reaction coefficient under the track when a culvert pipe is damaged.

(2) Comparative verification with on-site portable FWD tests showed that the calculation method developed in this study can safely estimate the distribution of subgrade reaction coefficients under the track.

(3) A nomogram has been developed to easily evaluate the impact on the track by calculating the track settlement under various conditions. This nomogram helps to determine more accurately the priority and frequency of inspections of the culvert pipes.

The method for calculating the reduction ratio of subgrade reaction coefficients developed in this study tends to produce values that are approximately 20% on the safe side. Additionally, conservative conditions were used to produce the nomogram. It is therefore possible to estimate the impact with higher accuracy by further in-depth analysis. We are currently working on revising the chart through comparative verification with actual field conditions. Furthermore, this nomogram evaluates the impact immediately after the culvert pipe is damaged. If soil erosion into the pipe occurs due to prolonged rainfall after the damage, the impact may change. We are currently investigating this aspect and will report on new findings in due course.

Table 4 Examples of nomogram (soil 4)

<table>
<tr><th></th><th>φ=12°</th><th>φ=17°</th></tr>
<tr><td>c=30 kPa</td><td>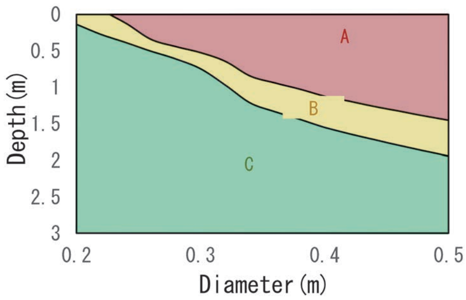
</td><td>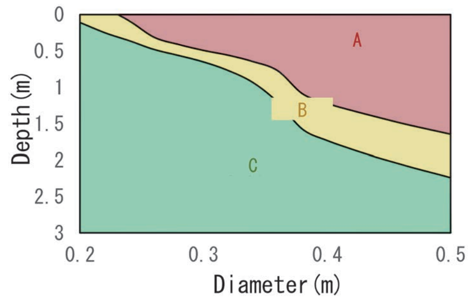
</td></tr>
<tr><td>c=10 kPa</td><td>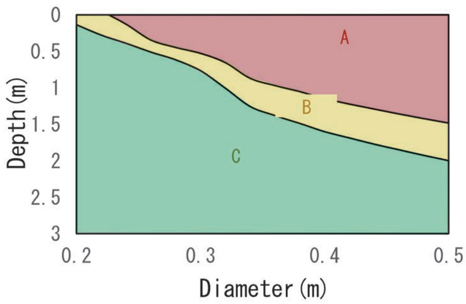
</td><td>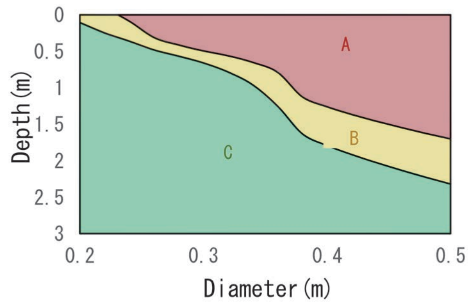
</td></tr>
</table>

Area A: Track settlement is large
Area B: Track settlement is moderate
Area C: Track settlement is small

References

[1] Railway Technical Research Institute, *Design Standards and Commentary for Railway Structures (Foundation Structures)*, 2007.

[2] Railway Technical Research Institute, *Design Standards for Railway Structures and Commentary (Earth Structures)*, 2007.

Authors

Takashi NAKAYAMA, Dr.Eng.
Senior Researcher, Tunnel Engineering Laboratory, Structures Technology Division
Research Areas: Tunnel Engineering

Akihiko MIWA
Assistant Senior Researcher, Tunnel Engineering Laboratory, Structures Technology Division
Research Areas: Tunnel Engineering

Yu OHARA
Researcher, Tunnel Engineering Laboratory, Structures Technology Division
Research Areas: Tunnel Engineering

Takaki MATSUMARU, Dr.Eng
Senior Researcher, Foundation & Geotechnical Engineering Laboratory, Structures Technology Division
Research Areas: Geotechnical Engineering

Allowable Strain Value for Contact Wires Taking into Account Probability of Failure

Takuya OHARA **Chikara YAMASHITA**
Current Collection Maintenance Laboratory, Power Supply Technology Division

The allowable strain value for all types of contact wire, including high-strength contact wires, has been set to 500×10⁻⁶ based on the fatigue characteristics of a basic hard-drawn copper. However, as train speeds increase, the strain value of contact wires may increase to more than 500×10⁻⁶ in the future. Therefore, in this paper, we propose a method for setting allowable strain values for each contact wire, taking into account the probability of failure. This probability is consistent with the margins of the conventional allowable strain value of 500×10⁻⁶. In addition, using this method, we propose allowable strain values for four types of high-strength contact wires.

Key words: *contact wire, allowable strain value, fatigue test, S-N curve, probability of failure, mean tensile stress*

1. Introduction

When a pantograph slides over a contact wire, bending strain is generated in the contact wire. This bending strain tends to increase as the train speed increases. Depending on the magnitude of the strain, the contact wire may break due to fatigue. To suppress the fatigue breakage of the contact wire, the allowable strain value for contact wires has been set at 500×10^{-6}, and railway operators confirm that the strain of contact wires is below the allowable value.

This allowable strain value was set by adding a certain margin to the fatigue properties of hard-drawn copper wire under no tension conditions [1]. So far, this allowable strain value has been applied to all types of copper and copper alloy contact wire. However, if the contact wire strain increases in the future as a result of further increases in train speeds, railway operators may not be able to keep contact wire strain below the allowable value, even if they improve overhead contact line equipment.

It is now well known that there is a roughly positive correlation between the mechanical strength and fatigue resistance of metallic materials. Therefore, it is possible to increase the allowable strain value from 500×10^{-6} for high-strength copper alloy contact wires used in the simple catenary systems that are intended for operating speeds of over 300 km/h (hereafter referred to as “high-speed simple catenary system”) [2]. However, as described below, the conventional methods used to set allowable strain values have some problems, such as not quantifying margins. Therefore, in order to set different allowable strain values for each type of contact wire, it is necessary to quantify the basis for margins.

In this study, we propose a method for evaluating fatigue properties that can be applied to any type of contact wire by setting the statistical probability of failure equivalent to the margin in the conventional allowable strain value. In addition, using this method, we propose allowable strain values for four types of high-strength contact wires. We also investigate a method for calculating the allowable strain value of contact wires when the mean tensile stress is different.

2. Conventional method for setting allowable strain values

The conventional method for setting allowable strain values [1] is described below. First, bending fatigue tests under no tension on a wire made of the same material as the hard-drawn copper contact wire with a diameter of 2 mm are carried out. Then, based on the fatigue test results, an S-N curve for the wire (Fig. 1) is created. The bending stress amplitude of 120 MPa at 10^7 cycles on the S-N curve is defined as the fatigue limit. This is because, if number of cycles of 10^7 is regarded as the fatigue life of the contact wire, it is thought that a contact wire will need replacing due to wear before the wire fails due to fatigue.

Since the mean tensile stress is applied to a contact wire by the catenary tension in a real installation, the fatigue limit of the contact wire decreases from one that is not under tension. Therefore, the fatigue limit under non-tension is corrected to the fatigue limit under certain tension using the fatigue limit diagram called the Smith diagram shown in Fig. 2. In this diagram, when a stress equal to the tensile strength of a metal material (350 MPa in the case of hard-drawn copper) is applied, the material will fail immediately. So, the repeated stress at this point is 0 (point A in Fig. 2). There is an empirical law whereby the repeated stress as the fatigue limit decreases linearly with increasing mean tensile stress. And as mentioned above, the fatigue limit of hard-drawn copper with non-tension is 120 MPa, so the fatigue limit corresponding to the mean tensile stress forms a triangle ABC in Fig. 2. Then, in order to set a safer allowable strain value, the practical minimum fatigue limit of the contact wire (i.e., the fatigue limit of the contact wire that has been worn to its limit) is calculated. The mean tensile stress of the GT110 hard-drawn copper contact wire with a tension of 9.8 kN at the wear limit (residual diameter of 7.5 mm at the time) is 145 MPa. The re-

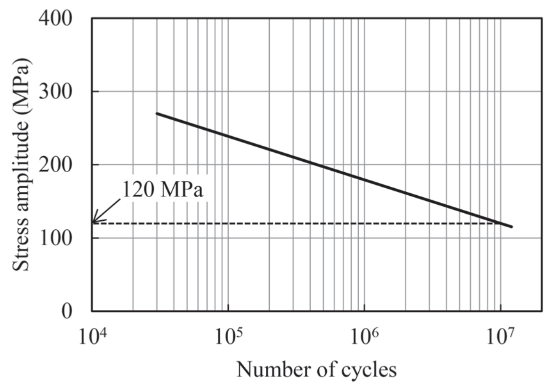

Fig. 1 S-N curve of non-tension hard-drawn copper wire
Note: Figure 1 is redrawn based on reference [1].

peated stress as the practical minimum fatigue limit is calculated to be 70 MPa at the 145 MPa position on the horizontal axis in Fig. 2. Furthermore, a margin for uncertainties (such as deformation of the overhead contact line height over time and surface deterioration of the contact wire [1]) is added to this value to set the allowable stress 60 MPa. Finally, the value converted to strain using Young's modulus of hard-drawn copper, 120 GPa, is the conventional allowable strain value of 500 × 10^{-6}.

There are two problems with the above method of setting the allowable strain value. The first problem is that the quantitative basis for the margin between 70 MPa and 60 MPa has not been presented. From past experience, it is true that fatigue failure can be prevented by keeping the contact wire strain in actual overhead equipment at 500 × 10^{-6} or less, so the above margin is considered to be sufficient for safety. However, there is a possibility that this margin is excessive.

Another problem is that the conventional allowable strain value is set based on the S-N curve obtained from the fatigue test results of hard-drawn copper wire under non-tension. The S-N curve should be prepared by matching the size of a test specimen and repeated bending stress as closely as possible to actual conditions of use. It is therefore desirable to set an allowable strain value based on the S-N curve obtained from fatigue test results of real contact wires under tension.

As mentioned above, the margin for setting the conventional allowable strain value is intended to include the effects of deterioration over time. However, this margin does not reflect the quantitative deterioration of the contact wire. It is thought to be a value that gives a sufficient margin in the fatigue characteristics of a new contact wire to compensate for deterioration. Therefore, to quantify how much safety the conventional allowable strain value margin gives for a new contact wire, we decided to evaluate it using the statistical probability of failure.

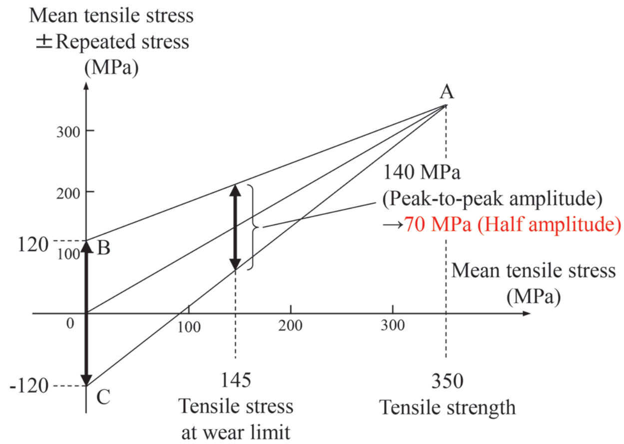

Fig. 2 Smith line of hard-drawn copper wire

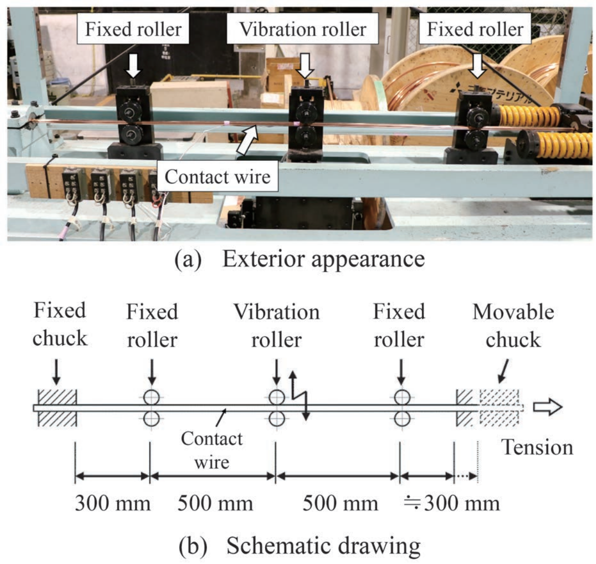

Fig. 3 Wire/metal fittings vibration testing machine

3. Margin of the conventional allowable strain value

3.1 Test method

In this chapter, we carry out fatigue tests on real contact wires of hard-drawn copper under tension. We also obtain a P-S-N curve (S-N curve for P% probability of failure) from the fatigue test results and clarify a probability of failure that is consistent with the conventional margin. In the following, a graph in which the vertical axis (stress amplitude) of the S-N curve is converted to strain amplitude is also treated as an S-N curve.

The tests were carried out using the "wire/metal fittings vibration testing machine" shown in Fig. 3. This machine is capable of applying tension to a real contact wire, and also has a mechanism to repeatedly generate any bending strain by vibrating the vibration roller. The fatigue tests were carried out until the contact wire broke, and the number of repetitions until the break was measured. The vibration waveform was a sine wave, the vibration frequency was 5 Hz, and the tension was 9.8 kN, which is the standard tension at the time of installation.

The contact wire used in the test was a hard-drawn copper contact wire, GT110. Table 1 shows the allowable stress of GT110 (tensile strength divided by a safety factor of 2.2) and the mean tensile stress corresponding to each residual diameter. The hard-drawn copper contact wire was machined to a residual diameter of 7.1 mm to meet the mean tensile stress condition (156.2 MPa) corresponding to the wear limit at a tension of 9.8 kN. Figure 4 shows a cross-section of the hard-drawn copper contact wire after machining.

The fatigue limit was set to a strain amplitude corresponding to 10^7 cycles, similar to the method used to set the conventional allowable strain value. Other test procedures and the construction of the S-N curve were carried out in accordance with the 14S-N test method in reference [3].

3.2 Test results

The results of the fatigue test are shown in Table 2. And the S-N curve of GT110 created from the test results is shown in Fig. 5. Based on the data from the slope in Table 2, the slope data of the regression line (approximation line corresponding to a 50% probability of failure) of the S-N curve in Fig. 5 was set. Furthermore, the estimated standard deviation of the strain amplitude, $\hat{\sigma}$, was calculated to be 93 × 10^{-6} using the data from the slope.

A staircase method was used to estimate the strain amplitude corresponding to 10^7 cycles, which is the fatigue limit [3]. The horizontal data in Table 2 shows the test results using the staircase method. In addition, using the horizontal data, the mean strain amplitude corresponding to a 50% probability of failure, $\hat{S}_{10^7}$, was calculated to be 762 × 10^{-6}.

From the above $\hat{\sigma}$ and $\hat{S}_{10^7}$, the failure probability factor for any strain amplitude can be calculated as follows:

$$k = \frac{\hat{S}_{10^7} - S}{\hat{\sigma}} \qquad (1)$$

where k is the failure probability factor, and S is any strain amplitude.

Substituting the conventional allowable strain value of 500 × 10^{-6} for S in (1), k is calculated to be 2.81. According to reference [3], this value corresponds to a probability of failure of approximately 0.3%. This means that the margin included in the conventional allowable strain value of 500 × 10^{-6} is equal to the strain between 50% and 0.3% probability of failure at 10^7 cycles.

This margin roughly coincides with the general indicator of data variability, the 3σ interval (an interval that contains data with a 99.7% probability when the distribution of measurement data follows a normal distribution). This means that the above margin is equivalent to the minimum strain based on the general statistical indicator, and is therefore of an appropriate quantity.

3.3 How to set the allowable strain value

There are two approaches to setting the allowable strain value of a contact wire. The first approach is to use a width of the margin of hard-drawn copper contact wire as it is. The margin of hard-drawn copper contact wire is defined by the following formula: (strain amplitude with 50% probability of failure) - (strain amplitude with 0.3% probability of failure) = (762 − 500) × 10^{-6} = 262 × 10^{-6}. This approach defines the allowable strain value as the value obtained by subtracting 262 × 10^{-6} from the 50% probability of failure strain amplitude of the target contact wire. The second approach defines the allowable strain value as the strain amplitude with 0.3% probability of failure of the S-N curve of the target contact wire.

Now, the variation in fatigue properties depends on the material and processing of the contact wire. Therefore, applying the margin of hard-drawn copper contact wire as it is, may lead to a dangerous evaluation in some cases. For this reason, the second approach, which allows the variation in fatigue characteristics to be evaluated for each type of contact wire, is considered more appropriate.

From the above, this paper proposes a method for evaluating the fatigue properties of contact wires as follows: Obtain the S-N curve of a contact wire under mean tensile stress conditions equivalent to the wear limit, and evaluate the strain amplitude with a 0.3% probability of failure at 10^7 cycles.

4. Allowable strain values for high-strength contact wires

This chapter describes the results of setting the allowable strain values of four types of high-strength contact wires using the method proposed in the previous chapter. These contact wires are indium-containing hard-drawn copper contact wire, SNN170 (cross-sectional area 170 mm²), precipitation-hardened copper alloy contact wire, PHC110 (cross-sectional area 110 mm²) and PHC130 (cross-sectional area 130 mm²), and cobalt-phosphorus copper alloy contact wire, CPS130 (cross-sectional area 130 mm²). They are used in high-speed simple catenary systems, etc.

First, fatigue tests were carried out on these contact wires, and the S-N curves were obtained. Table 3 shows the allowable stress, tension, mean tensile stress, and residual diameter conditions for

Table 1 Mean tensile stress of hard-drawn copper contact wire, GT110

Residual diameter (mm)	Cross-sectional area (mm²)	Tensile strength (MPa)	Allowable stress (MPa)	Tension (kN)	Mean tensile stress (MPa)
12.34	111.1	344	156.4	9.8	88.2
7.3	65.2				150.4
7.2	64.0				153.2
7.1	62.7				156.2
7.0	61.5				159.3
6.9	60.3				162.6

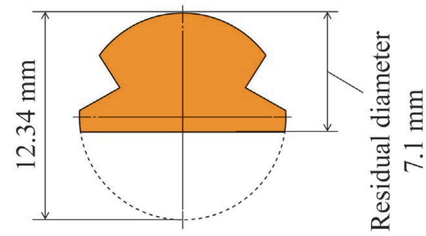

Fig. 4 Cross section of the hard-drawn copper contact wire, GT110

Table 2 Test results of the hard-drawn copper contact wire, GT110

Slope data			Horizontal data		
No.	Strain amplitude	Number of cycles	No.	Strain amplitude	Number of cycles
1	1930×10^{-6}	2.11×10^5	1	530×10^{-6}	>1.00×10^7*
2	1910×10^{-6}	1.86×10^5	2	630×10^{-6}	>1.00×10^7*
3	1580×10^{-6}	5.79×10^5	3	730×10^{-6}	>1.00×10^7*
4	1580×10^{-6}	5.50×10^5	4	800×10^{-6}	>1.00×10^7*
5	1240×10^{-6}	8.95×10^5	5	900×10^{-6}	9.00×10^6
6	1230×10^{-6}	1.51×10^6	6	810×10^{-6}	8.84×10^6
7	880×10^{-6}	5.37×10^6			
8	880×10^{-6}	7.53×10^6			

*> represents 'Not broken'.

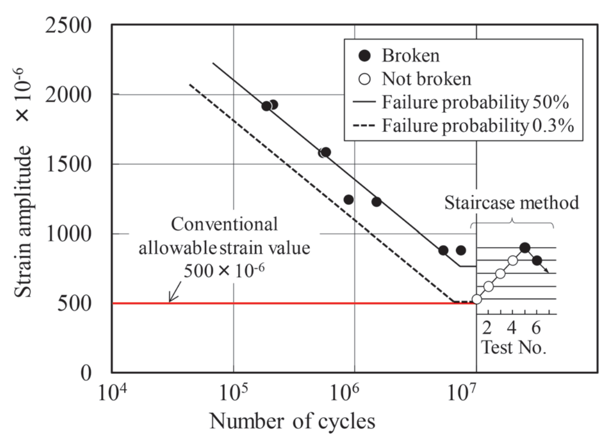

Fig. 5 S-N curve of the hard-drawn copper contact wire, GT110

Table 3　Allowable stress of high-strength contact wires and test conditions

Contact wire type	Allowable stress (MPa)	Test condition		
		Tension (kN)	Residual diameter (mm)	Mean tensile stress (MPa)
SNN170	196.5	22.54	10.4	194
PHC110	241.4	19.60	8.7	240
PHC130	241.4	24.50	10.2	240
CPS130	241.4	22.54	9.5	240

each contact wire. Tension was set to the tension when each contact wire was used in a high-speed simple catenary system. The residual diameter condition was set to the value when the mean tensile stress was equivalent to the wear limit, as described above. The other test methods were the same as in the previous chapter.

The S-N curves of each contact wire obtained from the fatigue test results are shown in Fig. 6 to Fig. 9. Table 4 shows the standard deviations obtained from each S-N curve and the strain amplitudes corresponding to failure probabilities of 50% and 0.3%. From Table 4, it can be seen that the allowable strain value of all high-strength contact wires is larger than the conventional allowable value of 500×10^{-6}.

5. Allowable strain for different mean tensile stresses

5.1 Method of calculating allowable strain when mean tensile stress is different

In the previous chapter, we showed how to obtain the minimum allowable strain value in practical use by setting the mean tensile stress condition of the contact wire equivalent to the wear limit. However, in reality, contact wires are rarely used to their wear limit for safety reasons, and are often replaced with some margin before they reach their wear limit. As the residual diameter increases, the mean tensile stress decreases, so the allowable strain should also increase. In this chapter, we consider how to calculate the allowable strain of a contact wire when the mean tensile stress conditions are different.

Reference [4] shows that fatigue test results with different mean stresses fall within a single variation band when organized by (maximum stress × stress amplitude)$^{1/2}$. It has also been reported that the equation proposed in reference [4] is applicable to hard-drawn copper contact wires [5]. Therefore, we convert the strain amplitudes in the fatigue test results of the high-strength contact wires mentioned above to strain amplitudes when the mean tensile stress is different using the above equation. Hereafter, we will add ’ (dash) to the symbol after changing the mean tensile stress. The following formula is obtained:

$$\left\{\left(\sigma_m+\sigma_a\right)\sigma_a\right\}^{1/2}=\sigma_e=\left\{\left(\sigma_m'+\sigma_a'\right)\sigma_a'\right\}^{1/2} \tag{2}$$

$$\therefore\quad \sigma_a'=\frac{-\sigma_m'+\sqrt{\sigma_m'^{2}+4\sigma_e^{2}}}{2} \tag{3}$$

$$\sigma_m'=T'/A' \tag{4}$$

where σ_m: mean tensile stress;
σ_a: stress amplitude,
σ_e: (maximum stress × stress amplitude)$^{1/2}$, that is,

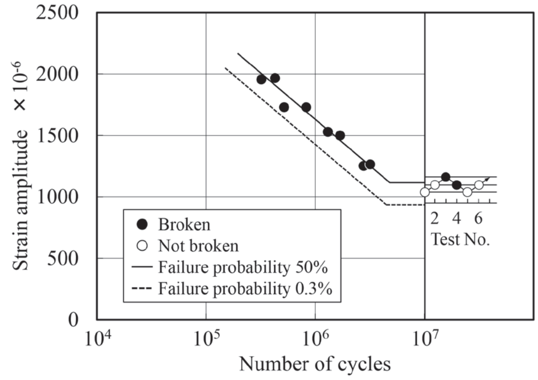

Fig. 6　S-N curve of SNN170

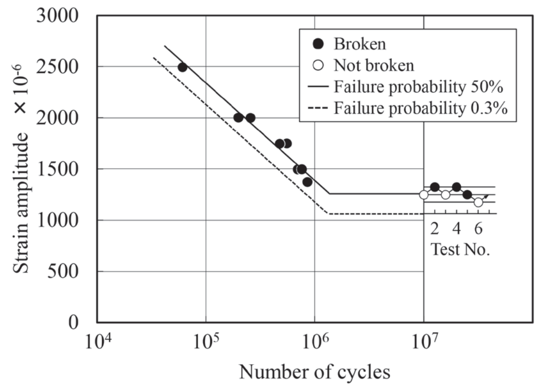

Fig. 7　S-N curve of PHC110

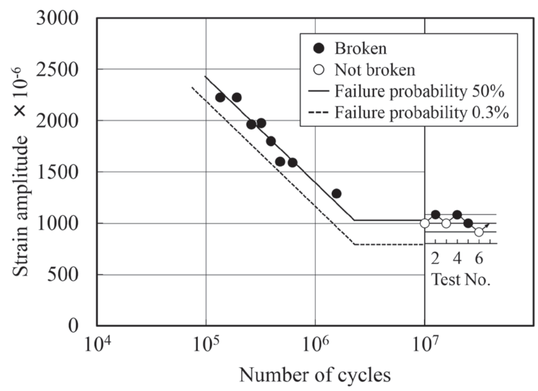

Fig. 8　S-N curve of PHC130

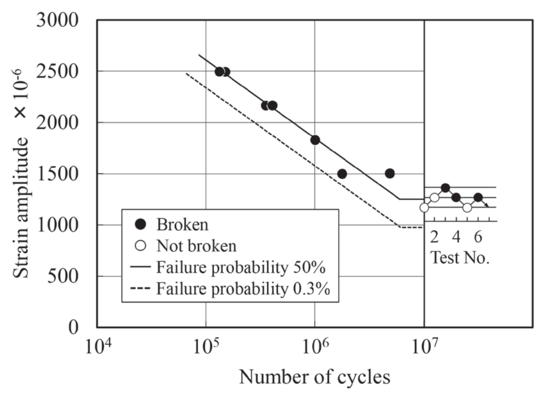

Fig. 9　S-N curve of CPS130

$\{(\sigma_m + \sigma_a)\sigma_a\}^{1/2}$,

T: tension; and,
A: cross-sectional area of contact wire.

Furthermore, by calculating σ_a' using (2) to (4), a strain amplitude after mean tensile stress conversion can be calculated using the following equation:

$$\varepsilon_a' = \sigma_a' / E \quad (5)$$

where ε_a: strain amplitude; and
E: Young's modulus of contact wire.
(Note that in section 5.2 and 5.3, E = 117.6 GPa.)

5.2 When residual diameter is different

First, we consider the case where the tension T of contact wire is constant and the residual diameter (i.e., A) is different. As an example, we use the test results of CPS130 in Fig. 9 and assume that the residual diameter is set before the mean tensile stress conversion to 9.5 mm (wear limit) and after the conversion to 12.0 mm. Figure 10 shows a comparison of the S-N curves before and after the conversion. To avoid complication, only the dots of the slope data are shown in Fig. 10. This figure shows that the larger the residual diameter, the larger the strain amplitude for the same number of cycles. Furthermore, comparing the allowable strain values showed that the allowable strain value increased by approximately 120 × 10^{-6} due to this conversion. Figure 11 shows the strain amplitude corresponding to a 0.3% probability of failure (i.e., allowable strain value) when the residual diameter is changed from 9.5 mm to 13.38 mm (new wire). From Fig. 11, it is possible to set the allowable strain value corresponding to the residual diameter of the replacement standard set by each company.

5.3 When tension is different

Next, we consider the case where the residual diameter of the contact wire is constant and the tension T is different. As in the previous section, the test results of CPS130 were used, and the tension was set to 22.54 kN before the conversion of the mean tensile stress, and to 14.7 kN after the conversion. Figure 12 shows a comparison of the S-N curves before and after conversion. This figure shows that the lower the tension, the larger the strain amplitude for the same number of cycles, and the difference is approximately 200 × 10^{-6}. Figure 13 shows the allowable strain value when the tension is changed from 9.8 kN to 22.54 kN. Using Fig. 13, it is possible to set the allowable strain value corresponding to the tension of the contact wire.

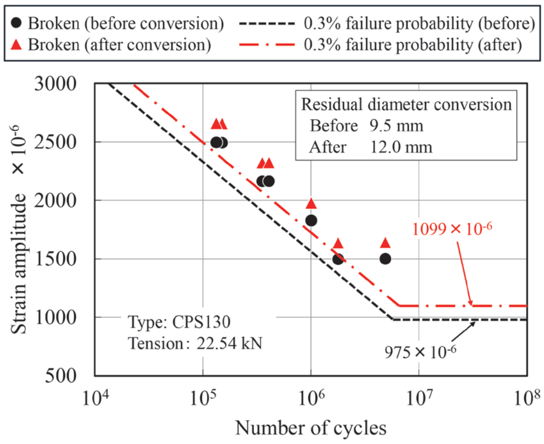

Fig. 10 Comparison before and after residual diameter conversion

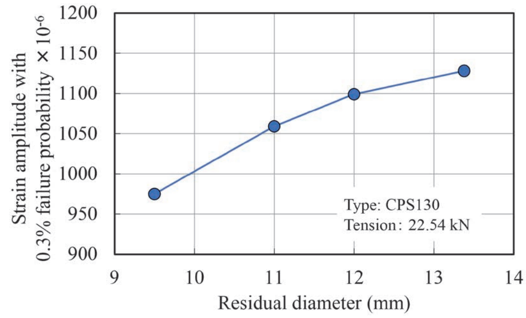

Fig. 11 Relation between residual diameter and strain amplitude with 0.3% probability of failure

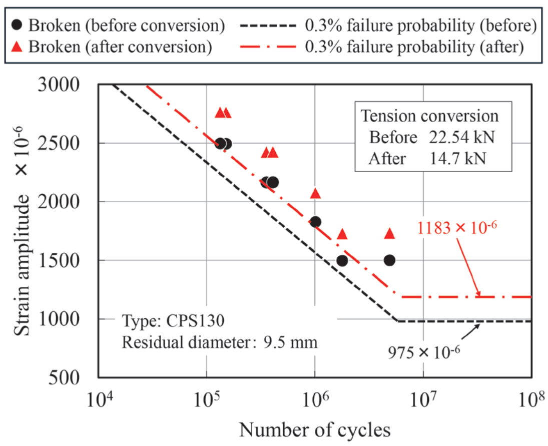

Fig. 12 Comparison before and after tension conversion

Table 4 Standard deviation of S-N curve, strain amplitude with 50% and 0.3% probability of failure

Contact wire type	Mean tensile stress* (MPa)	Standard deviation $\hat{\sigma}\times10^{-6}$	Strain amplitude with 50% probability of failure $\hat{S}_N\times10^{-6}$	Strain amplitude with 0.3% probability of failure $\times10^{-6}$ ($\hat{S}_N-2.75\hat{\sigma}$) (i.e. allowable strain value)
SNN170	194	63	1107	932
PHC110	240	74	1263	1061
PHC130	240	85	1016	781
CPS130	240	99	1247	975

*These data are at worn limit condition.

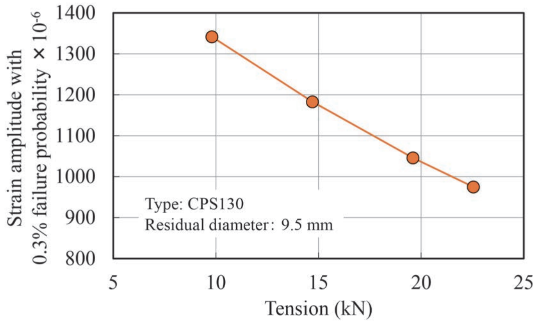

Fig. 13 Relation between tension and strain amplitude with 0.3% probability of failure

6. Conclusions

We quantified the margin of the conventional allowable strain value of contact wires using the probability of failure and proposed a new method for evaluating the fatigue properties of contact wires. We also set allowable strain values for four types of high-strength contact wires using the above method. Furthermore, we investigated a method for calculating the allowable strain value of contact wires when the mean tensile stress is different. The main results are as follows:

- The fatigue test results of GT110 contact wires under tension showed that the conventional allowable strain value 500 × 10^{-6} corresponds to the strain amplitude with a probability of failure of about 0.3% at 10^7 load cycles.
- In the P-S-N curve of a real contact wire under mean tensile stress equivalent to the wear limit, we propose to set the strain amplitude with a 0.3% probability of failure at 10^7 load cycles as the allowable strain value.
- Using the above method, we propose allowable strain values for four types of high-strength contact wires (Table 4).
- We organize the fatigue test results with different mean tensile stresses by (maximum stress × stress amplitude)$^{1/2}$, and present a method for calculating the allowable strain value of a contact wire at any mean tensile stress.

References

[1] Railway Technical Research Institute, *Manual and explanation for conventional railway operation speed improvement test* [Translated from Japanese.], Railway Research-Culture Promotion Foundation, pp. 203-209, 1993 (in Japanese).

[2] Tsunemoto, M., Shimizu, M., Irikura, K., Morimoto, H., Yamashita, C., and Ikeda, K., “Development of Simple Catenary System for Operation over 300 km/h,” *Quarterly Report of RTRI*, Vol. 61, No. 1, pp. 47-53, 2020.

[3] Japan Society of Mechanical Engineers, *Statistical Fatigue Testing Methods (Revised Edition)* [Translated from Japanese.], Japan Society of Mechanical Engineers, 1994 (in Japanese).

[4] K. N. Smith, P. Watson, T. H. Topper, “A Stress-Strain Function for the Fatigue of Metals,” *Journal of Materials*, Vol. 5, No. 4, 1970.

[5] Sugahara, A., Yamashita, C., “Evaluation of Factors Which Affects Fatigue Life of Hard-drawn Copper Contact Wire,” *RTRI Report*, Vol. 20, No. 9, pp. 17-22, 2006 (in Japanese).

Authors

Takuya OHARA
Assistant Senior Researcher, Current Collection Maintenance Laboratory, Power Supply Technology Division
Research Areas: Fatigue of Overhead Contact Line, Vibration Engineering

Chikara YAMASHITA, Ph.D. Eng.
Senior Chief Researcher, Head of Current Collection Maintenance Laboratory, Power Supply Technology Division
Research Areas: Tribology under Current Flowing Condition, Fatigue of Overhead Contact Line

FEM Analysis for Constructing Rail Head Transverse Crack Detection System Using Guided Waves

Yuki KONAYA **Mitsuru HOSODA**
Rail Maintenance and Welding Laboratory, Track Technology Division

Ryuichi YAMAMOTO
Rail Maintenance and Welding Laboratory, Track Technology Division (Former)

We performed simulations of ultrasonic wave propagation in cracked rails to investigate a method for detecting transverse cracks in the rail head using guided waves. The results show that 100-150 kHz input frequencies are suitable for detecting rail head cracks and that the peak intensity of the first few waves in the received signal waves decreases with the degree of cracking. Further investigation shows that transverse cracks greater than 20 mm that have grown below horizontal cracks can be detected by checking the intensity of the first three waves in the received waves at 100 kHz.

Key words: *guided waves, FEM analysis, rail defect detection, transverse crack, horizontal crack*

1. Introduction

Many railway operators regularly inspect rails for crack generation and size using rail inspection vehicles that transmit (or emit) ultrasonic waves from the top surface of the rail and detect the ultrasonic waves reflected from the cracks. However, as shown in Fig. 1, detecting transverse cracks, which account for approximately 40% of rail breakages, is difficult with a rail inspection vehicle. This is because transverse cracks develop below horizontal cracks that occur under the top surface of the rail, and ultrasonic waves cannot reach transverse cracks. Therefore, many railway operators generally detect transverse cracks by transmitting and receiving ultrasonic waves from the side of the rail head. However, this inspection method is manual work because continuous inspection is not possible, and it cannot be used to inspect rails with worn sides of the head and at level crossings. On the other hand, rail inspection methods using contactless air-coupled ultrasonic waves (guided waves) have been investigated in the past both in Japan and overseas [1, 2], and a contactless broken rail detection method using guided waves has also been proposed [3]. In this study, we created an FEM analytical model for contactless ultrasonic transmission and reception on the rail. Basic ultrasonic propagating simulations using this FEM analytical model with a slit in the rail have verified the conditions for ultrasonic waves to be sensitive to defects inside the rail. In addition, we performed ultrasonic propagating simulations using the FEM analytical model with an artificial horizontal crack and transverse crack in the rail to verify the possibility of detecting transverse cracks that exist below horizontal cracks by the received response.

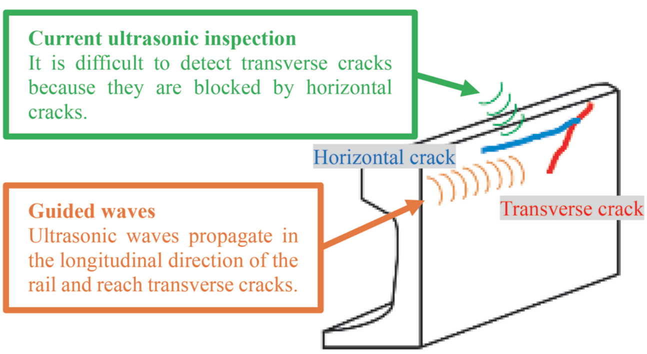

Fig. 1 Image of a horizontal and transverse crack in the rail head and ultrasonic propagation

2. Basic evaluation of the propagation characteristics of guided waves in a rail

2.1 FEM analysis model and analysis conditions

Figure 2 shows an overview of the FEM analysis model. We used ultrasonic analysis software "ComWAVE." The ultrasonic transmitter and receiver are placed away from the top surface of the JIS 50 kg N rail with a finite total length of 1500 mm. The mediums, which were the spaces between the transmitter (or the receiver) and the rail, were provided. Previous research has reported that the propagation depth in the rail varies depending on the frequency of the guided waves [4]. Therefore, we have to understand the input frequency that is sensitive to rail head defects such as transverse cracks. We then inserted a slit of varying depth into the cross-sectional direction from the top surface of the FEM rail models.

Table 1 shows the analysis conditions of the transverse crack model. In this analysis, we considered that the difference in the type of medium outside the rail does not significantly affect the ultrasonic propagation mechanism inside the rail and set water as the medium to reduce the computational load. This is because ultrasonic propagation wavelength in water is several times longer than that in air, significantly reducing the number of elements and analysis time. The element size of the FEM analysis model was set to approximately 1/20 of the ultrasonic wavelength propagating in the water medium (0.35 to 0.75 mm, depending on the input frequency) to ensure the accuracy of the analysis. Three types (100, 150, and 200 kHz) of the ultrasonic input frequency were used based on a study on rail breakage detection [3]. They were then propagated in the longitudinal direction of the rail as high-power continuous waves

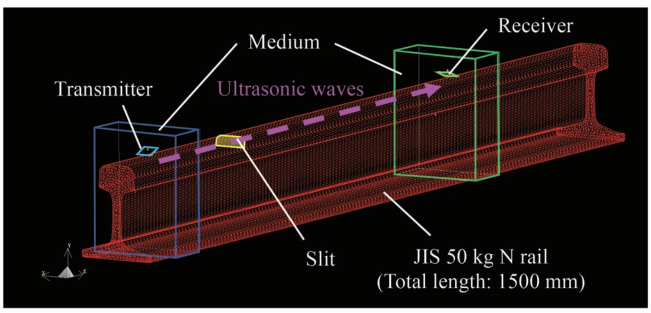

Fig. 2 FEM analysis model

Table 1 Analysis conditions (Part 1)
(a) Fixed conditions

Size of transmitter and receiver	25 mm square
Angle of transmitter and receiver	20°
Distance from transmitter to cracks	200 mm
Distance from transmitter and receiver to top surface	10 mm
Type of cracks	Transverse slit in rail head
Horizontal distance between transmitter and receiver	950 mm
Type of input wave	Wave burst
Input wavenumber	12

(b) Relationship between frequency of input wave and number of elements in FEM model

Input frequency	100 kHz	150 kHz	200 kHz
Number of elements, approx.	50 million	170 million	500 million

(wave bursts, wavenumber 12). The angle of both the transmitter and receiver relative to the horizontal plane was set at 20 degrees, and the critical angle of the transverse wave from the water to the rail was set to maximize the received intensity. This is because a previous study [5] showed that in a mode close to the transverse wave (approximately 3 mm/μs), the guided wave propagates through the rail head as a high-speed and high-intensity mode. Therefore, we can generally transmit the transverse wave with high intensity when the angle of the transmitter relative to the object is close to the critical angle. It has been confirmed that ultrasonic waves can be transmitted and received at a distance of more than 70 mm from the transmitter and receiver to the top surface of the rail when mounted on a railway vehicle [3]. However, since the purpose of this study is to understand the ultrasonic propagation characteristics inside the rail, the distance was set at 10 mm, taking into account the number of elements in the entire FEM analysis model, which affects computational load. The transverse slits inserted as cracks were 1 mm wide and inserted at a depth of 10 to 60 mm from the top surface. We also conducted guided wave propagation tests on a rail simulating this analysis model and have confirmed that these responses are almost identical to the analyses.

2.2 Results of FEM analysis

Figure 3 shows the ultrasonic propagation on the rail surface (contour map of the displacement). It was confirmed that the slit points inserted from the top surface of the rail show a change in the propagation of ultrasonic waves. In this study, unless otherwise noted, the intensity of the volume strain was used. Volume change in strain was obtained from the volume change calculated from the displacement in each direction of the three dimensions as the intensity of the received signal of the ultrasonic waves. The intensity of the peak values obtained from the analysis results of rails without cracks (slit) was considered to be 1.0, and then with this peak value, each analysis result was normalized.

Figure 4 shows the received waveforms when there is no slit, a slit with a depth of 10 mm and a slit with a depth of 40 mm in the FEM rail model, for 100 and 200 kHz, of the input frequency, respectively. It was confirmed that the intensity decreases with slit depth. Figure 5 shows the change in peak intensity as a function of the difference in slit depth for each input frequency. At the input frequencies 150 and 200 kHz, the peak intensity dropped sharply to about 0.6 when the slit was inserted at a depth of 10 mm from the top surface of the rail. At the input frequency of 100 kHz, the intensity decreased significantly when the slit was inserted at a depth of 20 to 40 mm deep. In addition, at the input frequency of 150 kHz, it was confirmed that the decrease in peak intensity was also large when the slit with a depth of 10 to 30 mm deep was inserted.

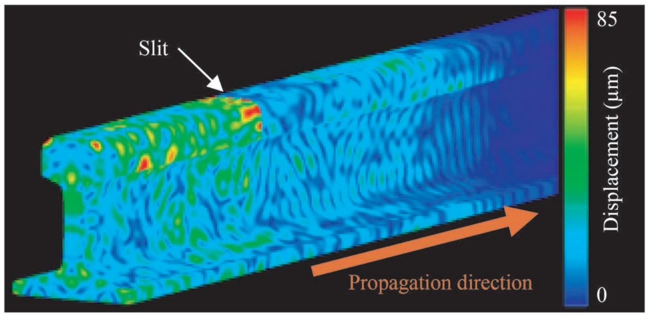

Fig. 3 Ultrasonic waves Propagation (input frequency: 100 kHz, slit depth: 40 mm) [6]

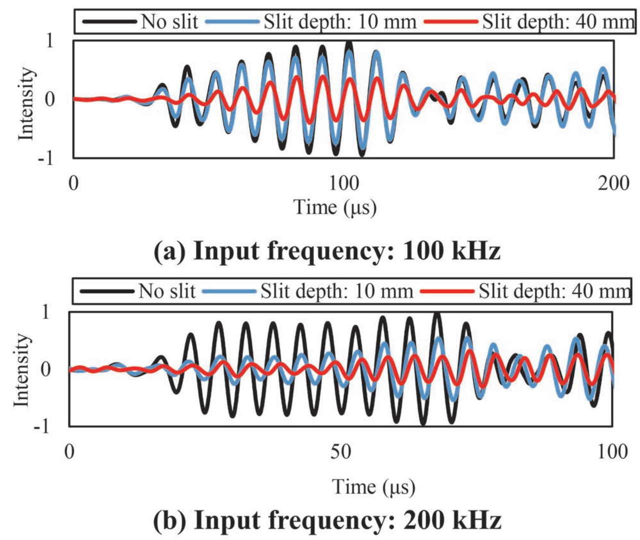

Fig. 4 Example of received waveform (Part 1)

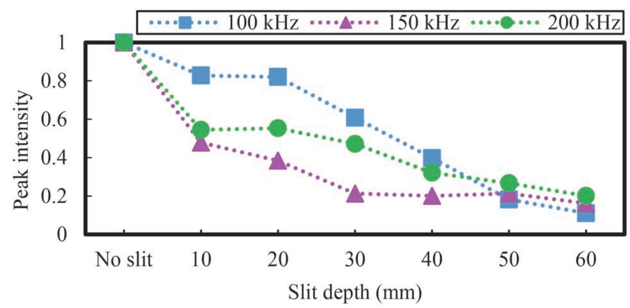

Fig. 5 Relationship between the depth of slit and the peak intensity

The transverse crack depth that should be detected through planned track inspections before rail breakage is 20 to 30 mm. The above results showed that guided waves with a frequency of 100-150 kHz are likely to be suitable for detecting transverse cracks in the rail head.

We further considered the change of depth of propagation in the rail as a function of the difference in ultrasonic frequency. We acquired waveforms at interval of 5mm in the longitudinal direction of the rail at a depth of the top surface and 40 mm from it and produced dispersion curves (color maps) of the volume strain by using two dimensional Fast Fourie Transform [7]. Figure 6 shows the produced dispersion curves. In Fig. 6, the horizontal axis indicates the frequency, and the vertical axis indicates the wavelength. Note that the strong intensity lines (volumetric strain amplitude) with white to red color represent the vibration modes of the waves that propagate prominently at each depth in the rail. The dispersion curves in Fig. 6 show that vibration modes below 200 kHz are stronger at a depth of 40 mm compared to the top surface. Therefore, we assumed that at a depth of 40 mm from the top of the rail, ultrasonic waves in the frequency band of 100 to 150 kHz propagated predominantly. In addition, the slit interrupting this depth partly blocked largely ultrasonic waves in these frequency bands.

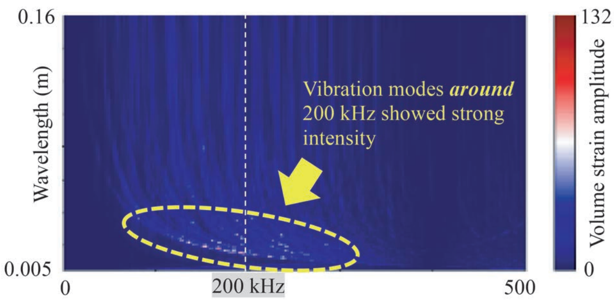

(a) Top surface

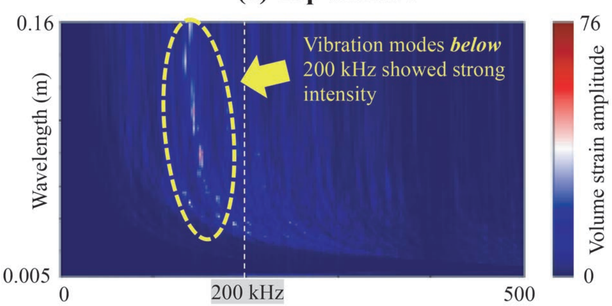

(b) Depth 40 mm from the top surface

Fig. 6 Dispersion curves of the volume strain in the longitudinal direction of the rail [6]

3. Evaluation of the propagation characteristics of guided waves on rail with horizontal and transverse cracks

3.1 FEM analysis model and analysis conditions

We created rail models with inserted artificial horizontal and transverse cracks and conducted FEM analysis to verify the detectability of transverse cracks that developed below the horizontal cracks. Figure 7 shows an overview of the analysis model for the rail model. The calculation process of the analysis was divided into three parts of a series of ultrasonic wave propagation processes from the transmitter to the receiver: propagation from the transmitter in the air to the inside of the rail, propagation in the longitudinal direction inside the rail, and propagation from the inside of the rail to the receiver in the air. We then created an independent model for each part and carried out the calculation in order. As a result, by setting a different mesh size for each model, we can perform calculations using air as the medium and significantly reduce the calculation load while maintaining the calculation accuracy.

Table 2 shows the conditions in this analysis. Since the medium was air, the angle of the transmitter and receiver concerning the horizontal direction was 6 degrees, which is the critical angle of the transverse wave from air to rail. Considering the results of Fig. 5 in Chapter 2, two ultrasonic input frequencies were set at 100 and 120 kHz, which are expected to have higher sensitivity. In addition, the input wavenumber was set to three. This is because, in general, the frequency distribution of the propagating wave becomes broader as the number of waves decreases [8]. Thus, we considered the possibility of capturing the change in the characteristics of the frequency distribution due to the cracks. Figure 8 shows the frequency distribution of the received wave in the case of 3 and 12 of the input wavenumbers obtained by FEM simulation without cracks in the

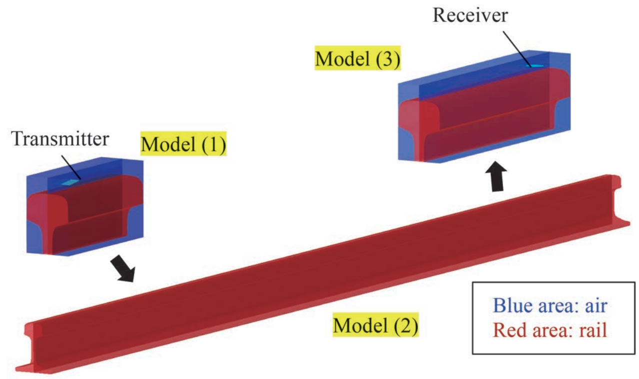

(a) Image of calculation in order

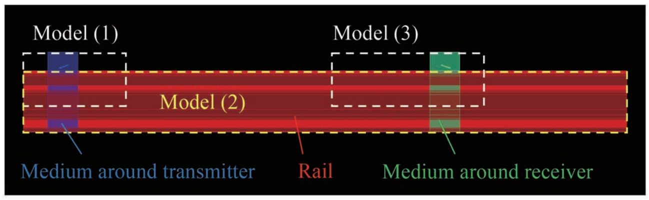

(b) Analysis area of each calculation part (side view)

Fig. 7 Partitioned FEM analysis model [6]

Table 2 Analysis conditions (Part 2)
(a) Fixed conditions

Size of transmitter and receiver	25 mm square
Angle of transmitter and receiver	6°
Distance from transmitter to cracks	200 mm
Distance from transmitter and receiver to top surface	10 mm
Type of cracks	Horizontal and transverse cracks (depth of 20 mm and 30 mm)
Horizontal distance between transmitter and receiver	950 mm
Type of input wave	Wave burst
Input wavenumber	3

(b) Relationship between frequency of input wave and number of elements in each FEM model

Input frequency		100 kHz	120 kHz
Number of elements, approx.	Model (1)	140 million	250 million
	Model (2)	30 million	30 million
	Model (3)	200 million	350 million

rails. The frequency distribution of the received wave was broader when the input wavenumber was three than when it was 12. Figure 9 shows the schematic shape of the cracks inserted into the rail model. As an artificial horizontal crack, an internal slit with a width of 30 mm and a length of 50 mm was provided at a depth of 7 mm from the top surface of the rail head. On the other hand, as an artificial transverse crack, a semicircular slit was provided at depths of 20 and 30 mm, extending vertically under the center of the horizontal crack.

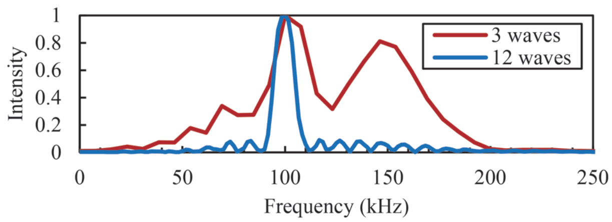

Fig. 8 Frequency distribution of received waves propagating through no cracked rail (input frequency: 100 kHz, normalized each maximum value as 1.0) [6]

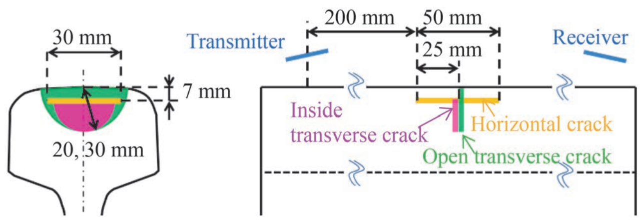

Fig. 9 Shape of artificial horizontal and transverse crack inserted in rail model

Furthermore, an artificial transverse crack opening to the top of the surface was provided at the same depth. For both cracks, the slit is 1 mm thick. Unless otherwise noted, the simple terms "horizontal crack" or "transverse crack" refers to the artificial cracks shown in Fig. 9. In the case of transverse crack, a semicircular slit that exists below the horizontal crack is described as "inside transverse crack" and a semicircular slit that opens at the top of the rail head is described as the "open transverse crack."

3.2 Results of FEM analysis

Figures 10 and 11 show the ultrasonic propagation in a model without cracks in the rail and a model with a horizontal crack and an inside transverse crack with a depth of 30 mm in the rail at an input frequency of 100 kHz. Figure 10 shows the state of the ultrasonic waves immediately after it reaches the crack. Figure 11 shows the state of the ultrasonic waves after they almost penetrate the crack. Compared with the model with cracks, the model without cracks shows the state from transmission at the same time. As found in Fig. 10 (a), it is confirmed that several ultrasonic waves stably propagate in the rail model, in which there is no crack. On the other hand, as found in Fig.10 (b), several ultrasonic waves are blocked by cracks in the cracked rail model. Comparing Fig. 10 with Fig. 11, it was confirmed that the number of propagating waves increases in Fig. 11. This seems to be due to an increase in mode changing and reflection during propagation inside the rail. Comparing Fig. 11(a) with Fig. 11(b), in the case of the models with cracks, only the first five to six waves of the series of propagating waves decrease in displacement. We assumed that this is because the preceding wave in a series of waves that eventually reached the receiver was greatly affected by cracks.

Figure 12 shows examples of received waveforms at input fre-

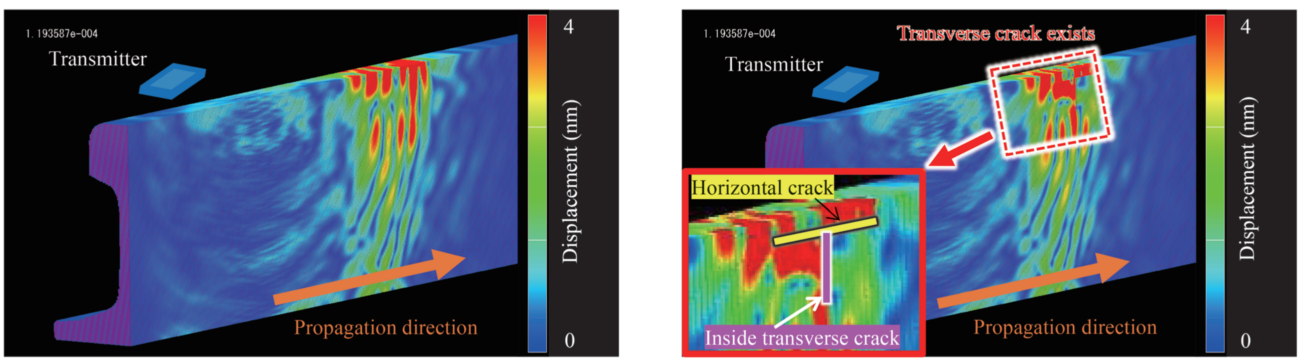

(a) No cracks **(b) Horizontal and inside transverse cracks**

Fig. 10 Propagation of ultrasonic waves reaching the crack in the rail

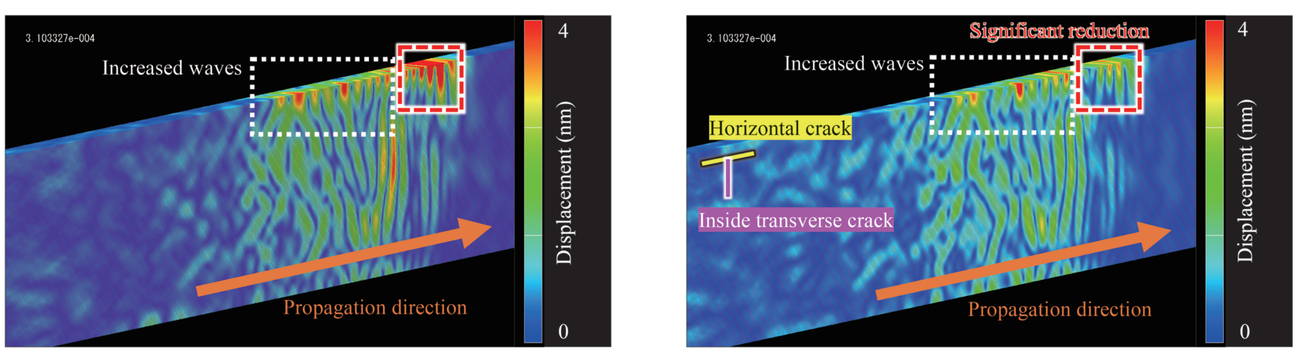

(a) No cracks **(b) Horizontal and inside transverse cracks**

Fig. 11 Propagation of ultrasonic waves after the crack transmission in the rail

quencies of 100 kHz and 120 kHz. Regardless of the type of crack, the wavenumber of all received waveforms became greater than three, the input wavenumber. In addition, the model with cracks showed that the amplitude of the first three waves (in the range by the red arrows in Fig. 12) was reduced compared to the amplitude of the fourth and subsequent waves. We can say that the characteristics in Fig.12 are generally consistent with the characteristics shown in Figs. 10 and 11, which visualize the state of ultrasonic propagation. Thus, we set a time range of 3 periods from the point at which the absolute extreme value of 0.01 or higher was first reached in the received waveform without cracks. The maximum amplitude of the waveform in this time range was then organized as the peak intensity. Figure 13 shows the relationship between crack conditions and peak intensity, with the peak intensity extracted for the entire received waveform and the peak intensity extracted over a time range. Figure 13 (a) shows no significant change at any input frequency under the condition of only a horizontal crack and the condition of horizontal and transverse cracks. In contrast, Fig. 13 (b) shows a different change in the peak intensity. In the case with an input frequency of 100 kHz, the decrease in peak intensity was about 0.15 at horizontal and inside transverse crack depth of 20 mm and about 0.2 at a depth of 30 mm compared to the condition where there was only a horizontal crack. In addition, we confirmed that the peak intensity was further reduced by about 0.1 under the condition of a horizontal crack and an open transverse crack. Therefore, by setting the threshold value to about 0.6, it is highly likely that we can judge the part below the threshold to be the location where the transverse crack with a depth of 20 mm or greater will exist. In the case with an input frequency of 120 kHz, the decrease of the peak intensity was about 0.045 at an open transverse crack depth of 20 mm and about 0.14 at that of 30 mm compared to the condition where the crack was only a horizontal crack. The change in peak intensity depending on the presence or absence of a transverse crack was small. Therefore, it may be difficult to set an accurate threshold to distinguish between the presence and absence of horizontal cracks and detect transverse cracks with a depth of 20 mm or deeper compared to the case with an input frequency of 100 kHz.

Furthermore, by comparing the frequency distribution of the received waves for each crack condition, we examined the possibility of detecting transverse cracks by focusing on changes in frequency distributions. Figure 14 shows the frequency distribution of the received wave under each crack condition. In both cases, with the input frequency of 100 and 120 kHz, there were two peaks around 100 kHz and 130 to 150 kHz. In addition, we confirmed that the peak at 130-150 kHz decreases according to the size of the horizontal and transverse cracks. By focusing on the reduction characteristics of this peak, it may be possible to determine the kind of crack.

There are still many parameters, such as the width, length, position of the horizontal crack, and the angle of the transverse crack progress. We plan to study further by FEM analysis.

4. Conclusions

We created FEM analytical models for contactless ultrasonic transmission and reception on the rail with various cracks. We then performed ultrasonic propagation simulations using FEM analysis models we developed, to examine the possibility of detecting the transverse crack of the rail head using guided waves. The results obtained in this study are summarized as follows.

(1) We performed ultrasonic propagation simulations using FEM analysis models in which a slit is inserted from the top surface of the rails. The results showed that ultrasonic waves with an input

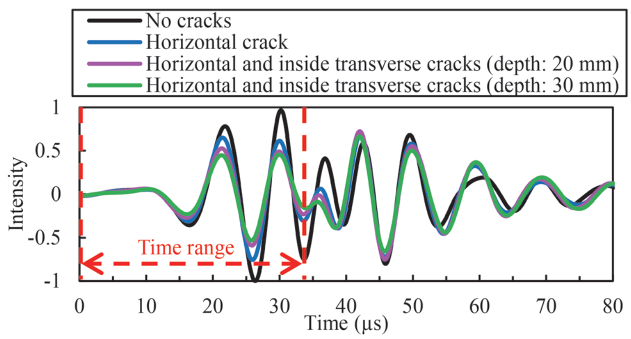

(a) Input frequency: 100 kHz

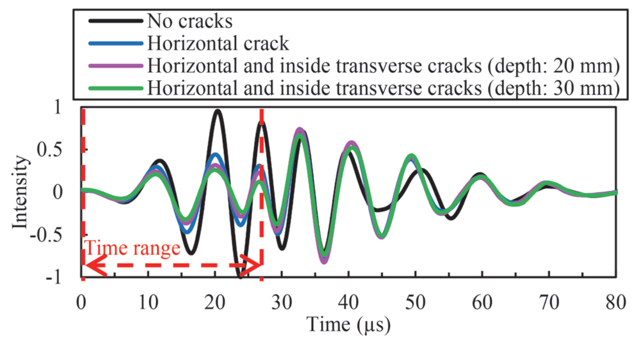

(b) Input frequency: 120 kHz

Fig. 12 Example of received waveform (Part2)

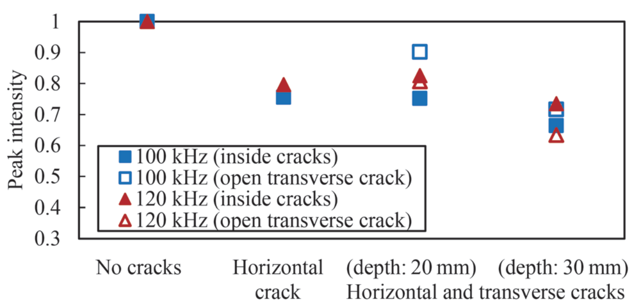

(a) The Peak intensities are extracted for the entire waveform

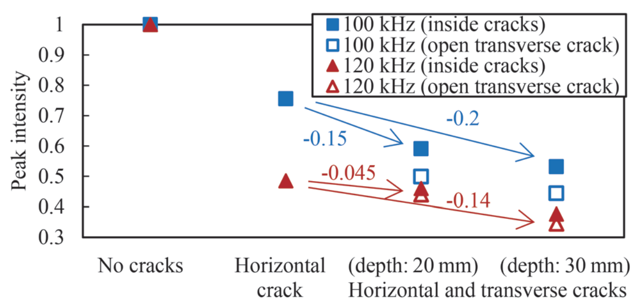

(b) The Peak intensities are extracted in the time range

Fig. 13 Relationship between crack conditions and peak intensity [6]

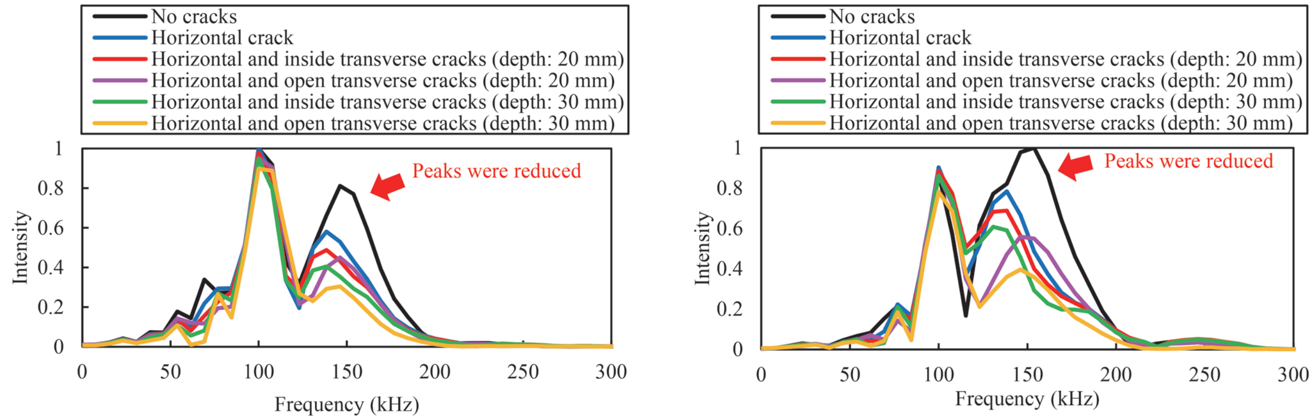

(a) Input frequency: 100 kHz **(b) Input frequency: 120 kHz**

Fig. 14 Frequency distribution of the received waves

frequency of 100 to 150 kHz are suitable for detecting transverse cracks with a depth of 20 to 30 mm.

(2) From the results of (1), we performed ultrasonic propagation simulations using FEM analysis models in which artificial horizontal and transverse cracks were inserted in the rails at an input frequency of 100 and 120 kHz. The results showed that the first few propagating waves were significantly affected by cracks. We confirmed that the peak intensity of only the first three waves of the received waveform decreased with the depth of the transverse crack under the horizontal crack. We also confirmed that the peak intensity was reduced in the case with an input frequency of 100 kHz rather than 120 kHz. By setting the threshold value to about 60% for the peak intensity under the condition of no cracks and extracting points below this threshold, it is possible to detect transverse cracks with a depth of 20 mm or more. In addition, by comparing the frequency distribution of the received waves, it was suggested that it may be possible to distinguish between horizontal and transverse cracks.

(3) Based on the results of this study, we plan to conduct further studies in the analysis and proceed with the construction of the system for detecting transverse cracks in rail heads using guided waves.

References

[1] Bayissa, W. L. and Dhanasekar, M., "High speed detection of broken rails, rail cracks and surface faults," *CRC for Rail Innovation (An Australian Government Initiative)*, 2011.

[2] Hayashi, T., Miyazaki, Y., Kataoka, K., and Takikawa, M., "Application of ultrasonic guided waves to rail inspection," *M&M Material Mechanics Conference*, Vol. 2007, pp. 72-73, October 2007 (in Japanese).

[3] Hosoda, M., Aizawa, H., and Yamamoto, R., "Rail broken detection system from vehicle as an alternative to track Circuits," *RTRI Report*, Vol. 36, No. 3, pp. 17-22, 2022 (in Japanese).

[4] Chong, M. L., Joseph, L. R., and Younho, C., "A guided wave approach to defect detection under shelling in Rail," *NDT&E International*, Vol. 42, pp. 174-180, April 2009.

[5] Hayashi, T., Won-Joon, S., and Joseph, L. R., "Guided wave dispersion curves for a bar with an arbitrary cross-section, a rod and rail example," *Ultrasonics*, Vol. 41, No. 3, pp. 175-183, May 2003.

[6] Konaya, Y., Hosoda, M., and Yamamoto, R., "Simulation of guided wave propagation to cracked rail using FEM models," *Proceeding of the Railway Engineering Symposium*, Vol. 27, pp. 71-78, July 2023 (in Japanese).

[7] Hayashi, T. and Kawashima, K., "Extraction of a single mode from multiple modes of lamb wave and its application to defect detection," *Transactions of the Japan Society of Mechanical Engineers. A*, Vol. 67, No. 664, pp. 83-89, December 2001 (in Japanese).

[8] Kawashima, K., "Ultrasonic nondestructive characterization of materials," *Transactions of the Japan Society of Mechanical Engineers. A*, Vol. 67, No. 655, pp. 16-23, March 2001 (in Japanese).

Authors

Yuki KONAYA
Researcher, Rail Maintenance and Welding Laboratory, Track Technology Division
Research Areas: Non-destructive Inspection of Rails, Rail Welding

Mitsuru HOSODA, Ph.D.
Senior Researcher, Rail Maintenance and Welding Laboratory, Track Technology Division
Research Areas: Non-destructive Inspection of Rails

Ryuichi YAMAMOTO, Ph.D.
Senior Chief Researcher, Head of Rail Maintenance and Welding Laboratory, Track Technology Division (Former)
Research Areas: Non-destructive Inspection of Rails, Rail Welding

Development of a Steam Weeding Technique with Excellent Weed-controlling Effect and Usability

Hikaru TANIGAWA
Track Structures and Geotechnology Laboratory, Track Technology Division (Former)

Tomoyoshi USHIOGI **Masateru IKEHATA**
Comfort Science and Engineering Laboratory, Human Science Division

Takahisa NAKAMURA
Track Structures and Geotechnology Laboratory, Track Technology Division

Currently, mowers are widely used for weed control along railway tracks. However, this method has some issues. For example, one of issues is that weeds regrow quickly after being cut during summer. Therefore, there is a need for more effective and efficient weed control methods. To address this need, we developed a specialized piece of steam weeding equipment. This equipment consists of a general-purpose steam cleaner and newly developed handheld nozzles. To verify the effectiveness of the developed equipment, it was tested in areas with vigorous weed growth. The test showed that this equipment provided effective usability with less labor and time. Furthermore, it was also confirmed that large weed regrowth was reduced by 70% after one year compared with mowers.

Key words*: *mowing, steam weeding, handheld nozzle, thermal denaturation, general-purpose steam cleaner

1. Introduction

Railway field from outside the tracks to the boundary of the field is overgrown with weeds (Fig. 1), so bush cutter (mowing) is used as part of railway environment management. Mowing can temporarily remove weeds; however, weeds regrow in a relatively short period during summer. Mowers are vibrating tools, which have restrictions on the working time to prevent health problems. Thus, the amount of daily work is limited (consecutively 30 minutes, and totally 2 hours per day in Japan). Health problems, such as workers temporarily losing their hearing owing to the noise of mowing, have been reported [1]. Other issues include the presence of signaling and communication cables for train operation, which requires advance searching for preventing the cables from being cut by the rotating blade of the mowing.

Other weeding methods include the spraying of herbicides, which chemically inhibit the photosynthesis and growth of weeds. The spraying of herbicides is highly effective, but the risks of the scattering or runoff of herbicides off-site need to be considered, and their use needs to be limited depending on the environment along the railway tracks. Thus, there is a demand for a weeding method that is safer and has a lower environmental impact while ensuring ease of application and effectiveness.

Therefore, we focused on “steam weeding,” which uses heat to kill weeds by causing thermal denaturation of their proteins. We decided to develop a steam weeding method that is easy to apply and extremely effective.

As this method uses steam (water), there are no environmental impacts, as is the case with spraying herbicides. This method is also expected to kill ungerminated seeds [2], which cannot be achieved by mowing or spraying of herbicides.

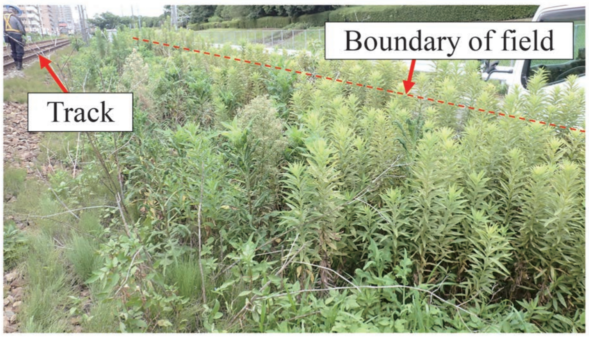

Fig. 1 Example of overgrown weeds on railway field

2. Development of the steam weeding method

2.1 Configuration of the steam weeding equipment

Figure 2 shows the equipment for the developed steam weeding method. The equipment consists of one general-purpose steam cleaner and two sets of newly developed handheld nozzles. As shown in Fig. 3, all the necessary items, which include a plastic tank filled with water for refills, can be loaded and transported on a truck with a surface area of around 3 m^2.

Steam weeding was originally developed in the agricultural field as a technique for sterilizing and disinfecting soil. It generally uses tap water, so the steam generation source (boiler) is large. A large quantity of water is required (around 1000 L/h), and a boiler engineer’s license is required for operation.

However, this equipment is impractical for use in a railway environment, where the use of tap water is difficult and practical application requires limiting the water consumption to the number of tanks with a capacity of approximately 20 L. Therefore, we first selected a boiler with a water consumption rate that would be suitable for steam weeding in a railway environment. By investigating domestic commercially available products, we selected a general-purpose steam cleaner with a water consumption rate of 72 L/h, which is less than a tenth of the amount generally used in the agricultural field. The selected product does not require any qualifications for operation and can be started with a 100 V power source.

Larger models than the selected product were excluded because they consume more water (over 1000 L/h), require qualifications for operation, and need a 200 V power source. Smaller models which consume significantly less water (steam volume) at only a few liters per hour, were excluded because we concluded they would be unsuitable for removing the large weeds that grow on railway field.

2.2 Investigation of the shape of the handheld nozzle

We investigated the handheld nozzle based on the performance of the boiler. Work aimed at sterilizing and disinfecting soil in agricultural contexts involves covering the area of farmland to be treated with a sheet of a certain size and filling the area under the sheet with steam for several hours. Transposing this method to a railway environment, in areas which contain other facilities like electricity poles, would make the process time-consuming depending on the type of facilities in each location. There are also concerns that sheets may be blown away by wind. Therefore, we developed a handheld nozzle method that could respond in a flexible manner to the condition of the facilities and could process a unit work area (area of a cover part) within 10 seconds, considering the mowing time as a reference.

Figure 4 shows the developed handheld nozzle. The developed product is designed to release and retain steam supplied from the boiler through a hose inside the cover, ensuring heating efficiency while reducing water consumption (steam volume). The cover has lattice-shaped ribs (convex parts) that serve as a path for steam diffusion when densely grown weeds are covered to enable efficient heating.

We also investigated the shape of the steam outlet along with the cover. Figures 5 and 6 show the initial and final specifications of the steam outlet shape and their heating characteristics, respectively. The initial specification had a cover area of 0.16 m^2, with general slit shape used to exhaust steam downward from the top of the cover. The final specification involved inserting a cylindrical pipe into the weeds and spraying steam sideways near the ground surface toward the roots of the weeds. The cover area was also expanded 3.1 times (0.49 m^2) to improve speed of work.

The heating characteristics were measured by placing thermocouples (total of five points) on the ground surface at the four corners and center of the cover, and the temperature increased almost uniformly at all five points. The five-point average value is shown in both figures. Additionally, the thermal denaturation of proteins will definitively occur at 60°C. A study on the thermal denaturation of the cell membrane structures at high temperatures [3] reported that the cell membrane rapidly expands in volume at approximately 50°C. Research has also reported that immersion in water at 60°C for 2 seconds will cause stems and leaves to die. Therefore, 60°C was set as a benchmark at which weeds will die because of stem and leaf cell death. The study that tested the effect of the product on seeds in farmland [2] confirmed that the seed killing effect was observed at 90°C.

As shown in Fig. 5, the initial specification reached a temperature of 60°C in approximately 1 second, but insulation by the weeds in the top section delayed the process by 14 seconds to attain a temperature of 90°C. On the other hand, as shown in Fig. 6, the final specification reached a temperature of 90°C in approximately 5 seconds.

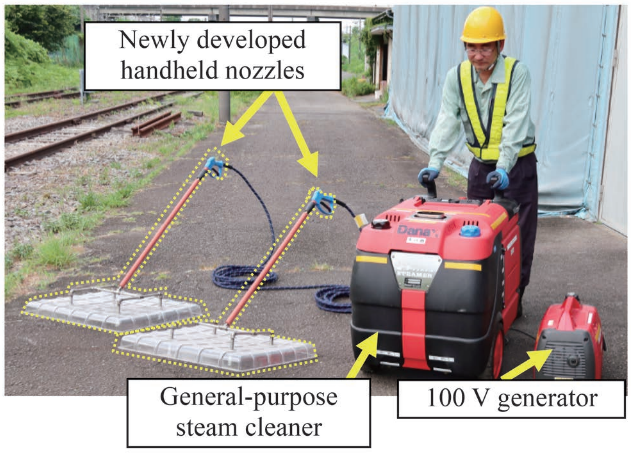

Fig. 2 Equipment for the developed steam weeding method

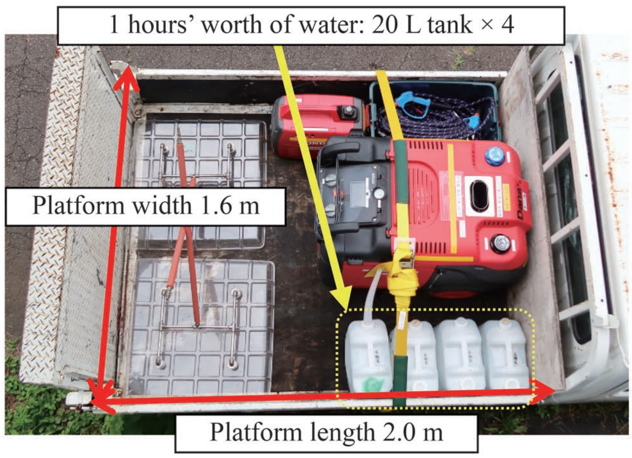

Fig. 3 Loading of the equipment and water on a truck

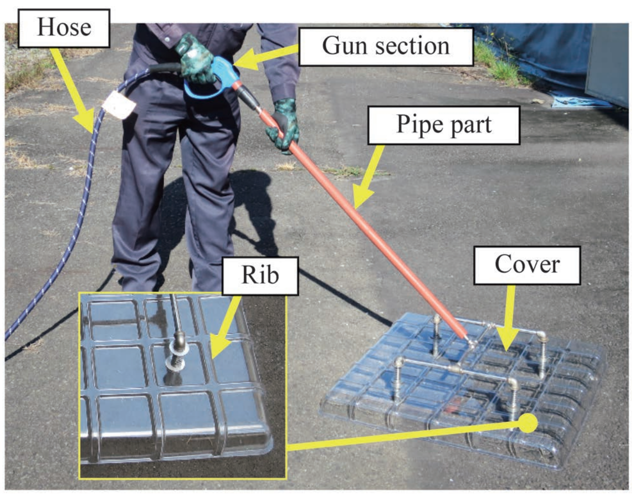

Fig. 4 Appearance of the developed handheld nozzle

We also evaluated the working environment in terms of noise by measuring the working noise of the equipment (equivalent sound level L_{Aeq}). The results indicated a value of 59.7 dB (1.5 m height) at ear level of the worker holding the handheld nozzle, 67.6 dB (ground level) 100 mm away from the cover of the handheld nozzle

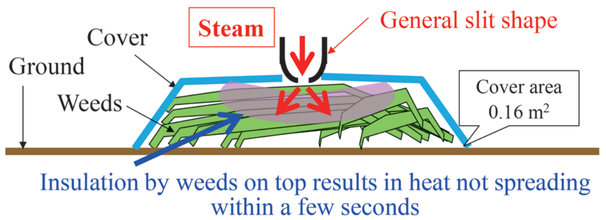

(a) Steam outlet shape

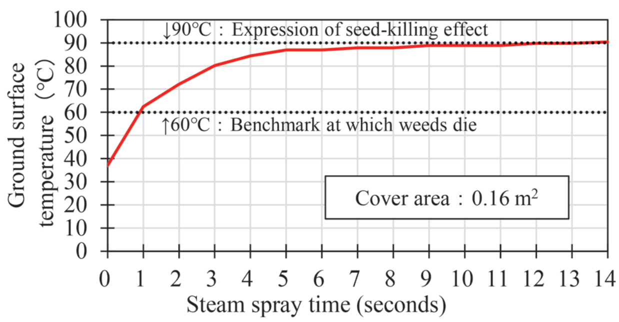

(b) Heating characteristics in areas with overgrown weeds

Fig. 5 Steam outlet shape and heating characteristics of the initial specification

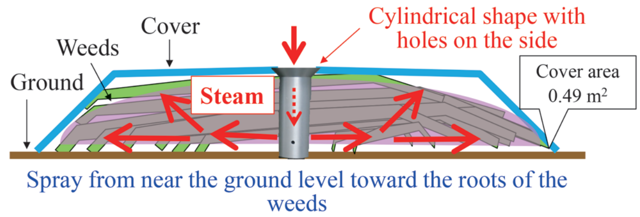

(a) Steam outlet shape

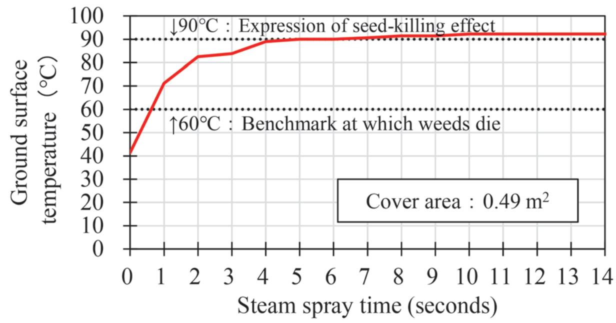

(b) Heating characteristics in areas with overgrown weeds

Fig. 6 Steam outlet shape and heating characteristics of the final specification

when spraying steam, and 67.0 dB (1.5 m height) 1 m away from the boiler during water heating. These values are sufficiently low not to disrupt conversations during work.

3. Effect of steam weeding application timing on weed regrowth

3.1 Experimental method

In order to determine the effect that timing of steam weeding (weeding season) had on weed regrowth, we conducted a test setting weeding method and weeding season as parameters.

We conducted the test in a location where *Imperata cylindrica*, a perennial weed of the *Poaceae* family, commonly grows. We prepared test plots measuring 2.2 m × 1.5 m, and weeding work was performed from spring to autumn in each test plot. The weeding season and weeding method were considered as parameters. The weeding method involved not only steam weeding but also mowing for comparison.

Mowing was done manually using shears to prevent seeds from scattering to other test plots and to keep the grass height within the plot constant after weeding. Actual work using a bush cutter involves raising the blade to a certain height above the ground surface to prevent flying stones as a result of contact with the blade. Crushed stone (maximum particle size of 63 mm) used for ballast beds may fall and scatter on railway field, so the target weed height for the shears was set at 63 mm from the ground surface. During mowing, the cut parts were disposed of as industrial waste.

During steam weeding, we used a handheld nozzle, as shown in Fig. 5. Given the relationship between the timing of this test and development of the handheld nozzle, the steam injection time was set at 5 seconds. As with herbicide spraying, steam weeding involves the stems and leaves being left to die and wither naturally in place without being separated from the roots, so they were left behind. As shown in Fig. 7, the weeds, which were compressed in place immediately after steam weeding, died after a few hours while still compressed.

The measured items were the maximum plant height and vegetation coverage of each test plot. The maximum plant height was normalized by dividing the value by the maximum value during the test period. The vegetation coverage was the ratio of the area occupied by weeds in the plot (Fig. 8) and was visually measured (excluding dead weeds). The experimental results were calculated by multiplying the normalized maximum plant height by the vegetation coverage, and this was considered as the weed regrowth extent. The measurements were recorded after the weeding work (next day, and 1-2 weeks later), and then at approximately monthly intervals.

3.2 Results and discussion

Figure 9 shows the measurement results of the weed regrowth extent. The weed regrowth extent was not 0 on the weeding day (Day 0) in the mowing results because weeds with a target height of less than 63 mm that were not mowed remained in the plot. The mowing results showed that regrowth began immediately after the weeding regardless of the work timing. For summer work, complete regrowth occurred approximately 60 days after weeding.

The steam weeding results showed that weed regrowth was suppressed for approximately 15 days after weeding in the spring and summer, and the number of days until complete regrowth tended to be longer than that with mowing. For autumn work, mowing results in about 50% regrowth, whereas steam weeding only resulted in about 10% regrowth. Steam weeding was more effective than mowing for all seasons.

The difference in regrowth was attributed to the fact that mowing avoids the sprouts near the ground surface, which regrow immediately, whereas steam weeding involved heat acting on the entire stem and leaves of the weeds, including the sprouts. Additionally, as shown in Fig. 7, steam weeding resulted in weeds covering the ground and blocking sunlight, which may have delayed regrowth

(a) Immediately after work

(b) Three hours after work

Fig. 7 Plot condition after steam weeding

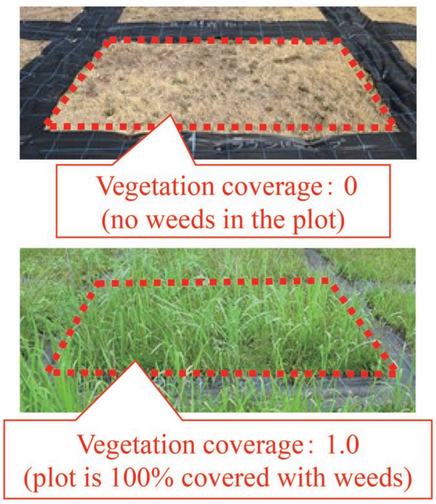

Fig. 8 Measuring vegetation coverage

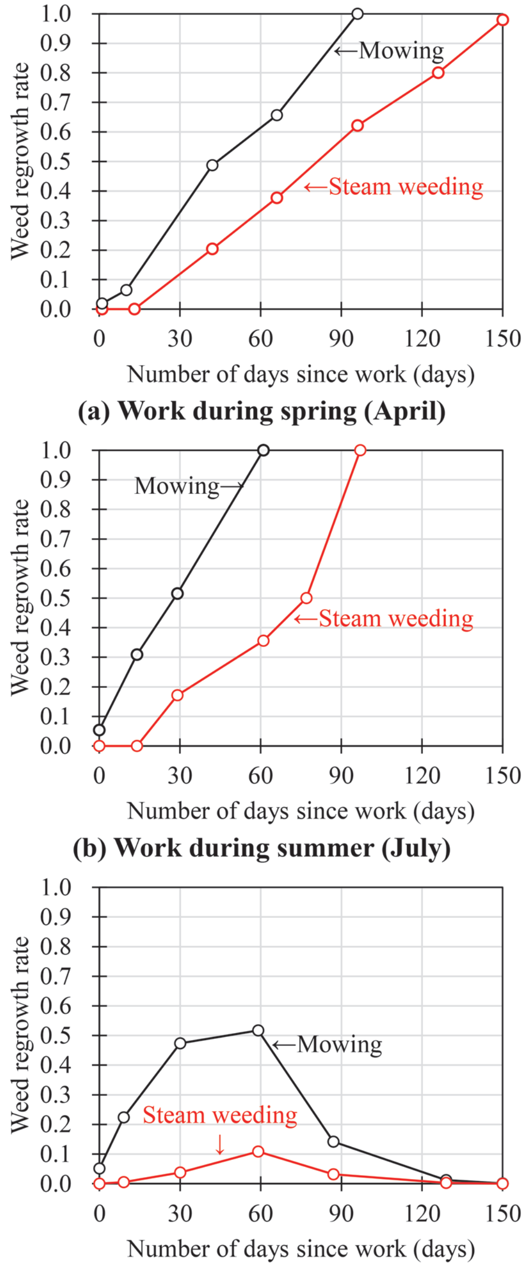

(a) Work during spring (April)

(b) Work during summer (July)

(c) Work during autumn (September)

Fig. 9 Measurement results of weed regrowth extent

owing to the shading effect. This experiment was not conducted in a railway environment, so a field test was subsequently conducted to verify the effectiveness of the equipment along a commercial line.

4. Verification of effectiveness of the proposed method

We confirmed the workability and weeding effect of the final developed equipment by conducting a field test along a commercial line. The field test was conducted in an area where the large weed *Solidago altissima* grows in clusters during the summer (July). Additionally, we set up a field where mowing was conducted in an adjacent location as a comparison. *Solidago altissima* is a perennial weed of the *Asteraceae* family that is known to form large communities and can be difficult to control [4].

The work speed, excluding post- and pre-work, were 4.0 m^2/min per mowing. The work speed was 5.0 m^2/min per handheld nozzle for steam weeding, confirming that the work speed was 1.25 times faster than mowing.

When looking at the work site approximately three months after the work (October), the mowed plots (Fig. 10) showed *Solidago altissima* regrowing in about 80% of the area where weeding was conducted, with flowering being observed. In contrast, in the steamed plots (Fig. 11) *Solidago altissima* regrowth was limited to approximately 10% of the work area with no flowering. As in the previous section, regrowth was thought to have been hampered because steam weeding acts on all stems and leaves on the ground surface, and no new sprouts that could regrow remained. As in the previous section, the steam-weeding effect observed was greater than for mowing, but was also greater than the summer results in the previous section. This was thought to be due to the effect of different weed species as the test in the previous section was conducted in an

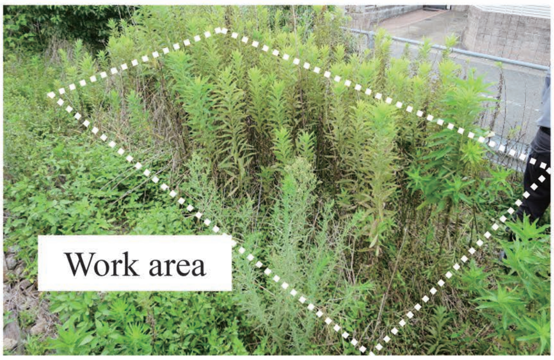

(a) Before work

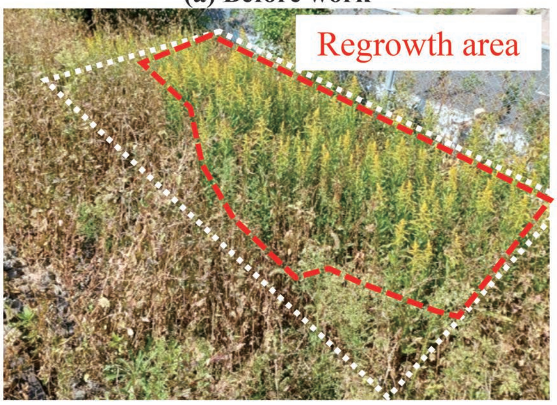

(b) Approximately three months after work

Fig. 10 Condition of plots after mowing

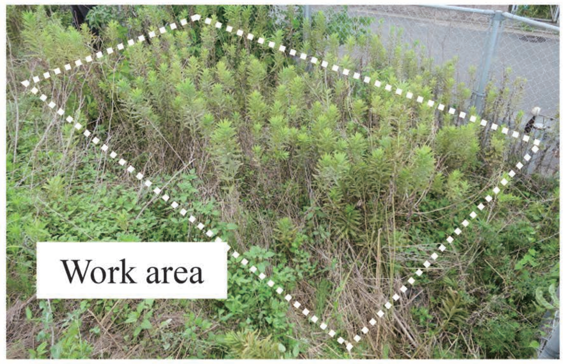

(a) Before work

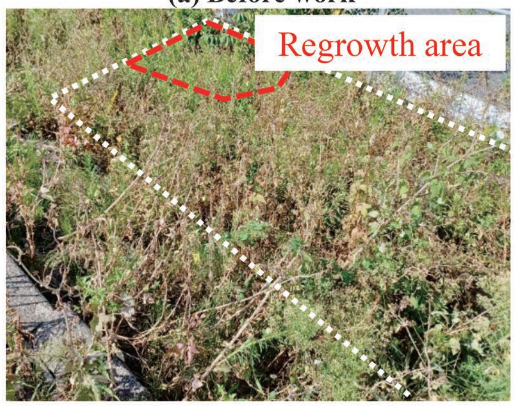

(b) Approximately three months after work

Fig. 11 Condition of plots after steam weeding

area where there was an overgrowth of *Imperata cylindrica*.

Furthermore, long-term effects were confirmed by measuring the number of remaining *Solidago altissima* plants in an arbitrary 1 m^2 area one year later. The number of plants in the plot subjected to mowing was 89 plants/m^2 compared to 25 plants/m^2 in the plot where steam weeding was conducted. This confirms that the number of remaining large weed plants one year after application had decreased by approximately 70%. Research indicates that mowing needs to be conducted at least three times a year to control *Solidago altissima* [4], but one steam weeding work session reduced the number of remaining plants one year later. This is because steam weeding was effective in killing seeds along with stems and leaves on the ground.

The abovementioned results were obtained in the summer, but steam weeding is expected to have a similar effect in other seasons as the method is expected to achieve effects against seeds that cannot be achieved by mowing.

Work was also conducted on the same day in other locations to those shown in Fig. 10 and Fig. 11, and the number of plants was measured one year later in the same manner. Similar results were obtained for regrowth. The number of remaining plants after one year was 109 plants/m^2 for the plot where mowing was conducted, and 24 plants/m^2 for the plot where steam weeding was conducted. Overall, we confirmed a reduction of approximately 80% in other locations.

5. Weeding efficiency estimation

We considered the work efficiency of the weeding method by estimating the work time for mowing and steam weeding from the work rate obtained in the field test. We assumed a general work area of 300 m^2 and calculated the time required from the start to the end of the work. For mowing, we assumed a work party of 5 people, including three workers to operate three mowers and two workers to search for signaling and communication cables laid within the site and to collect cut grass. For steam weeding, the equipment consisted of one boiler and two handheld nozzles, so we assumed a work party of 3 people, including two operators for the handheld nozzle operators and one boiler monitor/water supplier. The measurement results from the previous section were used as a reference to estimate the work time: 4.0 m^2/min per mowing and 5.0 m^2/min per handheld nozzle.

Figure 12 shows the work time estimation results. Mowing required advance work to search for cables and follow up work to collect the cut grass. Thus, the total time required was 72 minutes.

Meanwhile, the time required for steam weeding was 22 minutes less, for a total work time of 50 minutes. The results showed that steam weeding improved the work rate by 44% compared to mowing while reducing the number of workers required from 5 to 3, or by 60%. The breakdown of work showed however that the time required for actual weeding using steam was longer than actual mowing owing to the use of three mowers for two handheld nozzles. However, when taking into account preparation and cleaning, the overall work time was shorter for steam weeding.

6. Conclusions

We developed a steam weeding method that combines a general-purpose steam cleaner with a newly developed handheld nozzle. Our equipment provides a practical, environmentally friendly solu-

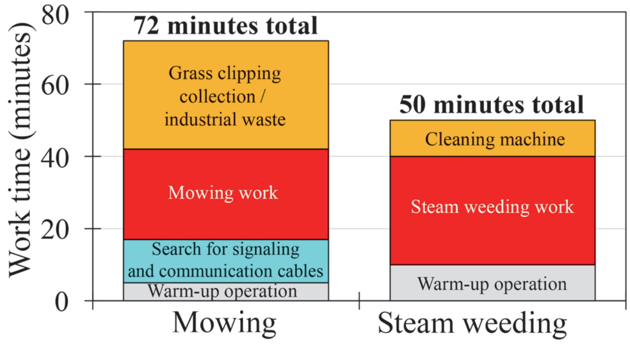

Fig. 12 Work time estimation results

tion for weeding in a railway environment. It reduces labor, improves work efficiency, and delivers better long-term weed control compared to conventional mowing methods. The equipment successfully controls large weeds with just one treatment per year, compared to multiple interventions needed with mowing, representing a significant advancement in railway weeding technology.

While our current research focused on areas outside actual railway tracks, we have begun developing an extension of our method that can be towed along the tracks to control weeds growing between them. This adaptation promises to further improve weeding in the railway environment.

Acknowledgment

We would like to thank all the individuals involved at the Kyushu Railway Company for their cooperation in conducting the field test and the follow-up observations in this study. We would like to express our sincere gratitude for their assistance.

References

[1] Mitarai, M. and Sicat, J. C. V., “Noise Characteristics of Farm Machinery and the Resulting Temporary Threshold Shift,” *Japanese Journal of Farm Work Research*, Vol. 33, No. 2, pp. 81-89, 1998 (in Japanese).

[2] Nishimura, A., Asai, M., Shibuya, T., Kurokawa, S. and Nakamura, H., “A steam-treatment technique for weed-seeds disinfestation in arable fields,” *Journal of Weed Science and Technology*, Vol. 59, No. 3, pp. 167-174, 2014 (in Japanese).

[3] Iwasaki, S. and Sugiura, Y., “Liquid Crystals and Membrane Structure,” *SEIBUTSU BUTSURI*, Vol. 15, No. 4, pp. 164-170, 1975 (in Japanese).

[4] Hattori, T., Akamatsu, H., Asami, K. and Takeda, Y., “Ecological Studies on Grassland Vegetation in Riverbed I. Effects of Cutting on Growth and Floristic Composition of *Solidago altissima* Community,” *Humans and Nature*, No. 2, pp. 105-118, 1993 (in Japanese).

Authors

Hikaru TANIGAWA
Assistant Senior Researcher, Track Structures and Geotechnology Laboratory, Track Technology Division (Former)
Research Areas: Ballastless Track, Ballasted Track

Masateru IKEHATA, Ph.D.
Senior Chief Researcher, Comfort Science and Engineering Laboratory, Human Science Division
Research Areas: Genotoxicology, Cell Biology, Microbiology

Tomoyoshi USHIOGI
Senior Researcher, Comfort Science and Engineering Laboratory, Human Science Division
Research Areas: Chemical Engineering

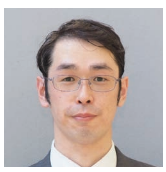

Takahisa NAKAMURA, Dr.Eng.
Chief Researcher, Track Structures and Geotechnology Laboratory, Track Technology Division
Research Areas: Ballasted Track, Roadbed Structure

Design Method for Power Generation Systems for Diesel Vehicles Using a Permanent Magnet Synchronous Machine and a Full-Bridge Rectifier

Minoru KONDO
Traction Systems Laboratory, Vehicle Technology Division

This paper describes a design optimization method for power generation systems for diesel vehicles consisting of a permanent magnet synchronous machine, a full-bridge rectifier and phase shift capacitors inserted between them. By combining an analysis method for the proposed systems and a multi-objective optimization method, a trial design optimization was carried out with the aim of minimizing indicators related to the size and weight of the system. Furthermore, the performance of the optimized design was verified by numerical simulations, and it was confirmed that the design achieved the required performance while satisfying the constraints of the system.

Key words: *permanent magnet synchronous machine, full-bridge rectifier, power generation system, multi-objective optimization*

1. Introduction

Diesel electric vehicles and hybrid vehicles for non-electrified lines use DC power generation systems with generators directly connected to the engines. Diesel electric locomotives and other vehicles use systems with brushless synchronous machines and full-bridge rectifiers (FBR) [1]. On the other hand, hybrid vehicles often use systems with induction machines or permanent magnet synchronous machines (PMSMs) controlled by Pulse width modulation (PWM) converters [2, 3, 4].

Currently, power generation systems using PMSMs are controlled by a PWM converter. However, PMSMs can be combined with FBRs because they can generate a magnetic field themselves with the rotor, just like brushless synchronous machines.

In general, PMSMs are more efficient than induction machines. In addition, FBRs are simpler than PWM converters (PWM converters include FBRs inside), and are small, lightweight, and inexpensive. Therefore, a power generation system that combines a PMSM and an FBR is expected to be highly efficient, small, and lightweight.

However, when simply combining a PMSM with an FBR, the amount of generated power is smaller than when controlled by a PWM converter. The reason for this is that in an FBR, the phases of the voltage and current on the AC side are roughly the same, and the system operates at a power factor of 100%. Therefore, we have devised a DC power generation system (Fig. 1) that changes the operating power factor of the PMSM by inserting a capacitor (hereafter referred to as a phase-shift capacitor) between the PMSM and the FBR, and have confirmed its basic performance by simulations [5, 6, 7].

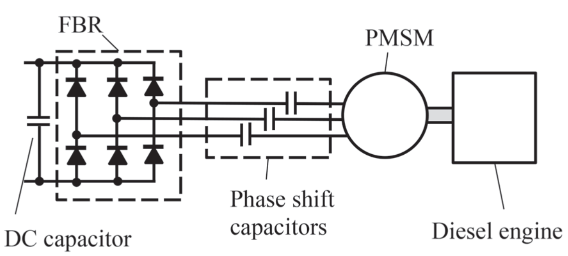

Fig. 1 Configuration of a DC power generation system using a PMSM and an FBR

In this power generation system, if the capacitance of the phase-shift capacitor is designed so that the inductance of the PMSM and the phase-shift capacitor form a series resonant circuit, a constant DC voltage is obtained regardless of the load [5, 6]. In this power generation system, the generated voltage and achievable power output strongly depend on the design of the PMSM and the design of the capacitance of the phase-shift capacitor. However, it has not been clarified how to determine these design parameters. Therefore, we propose a design method that combines a multi-objective optimization method [8, 9] with the analysis method we have developed for this power generation system. In the method, the machine constants of the PMSM and the capacitance of the phase-shift capacitor are set as design variables, and we optimize the objective indicators related to the size and weight of the system, such as the maximum current during operation and the kVA capacity of the phase-shift capacitor. Since diesel vehicles are equipped with many parts, minimizing the size and weight of the parts is particularly important, optimization is sought with the aim of reducing size and weight.

In this paper, we outline the design method and apply it to a specific design problem to demonstrate its effectiveness.

2. Power generation system to be designed

2.1 Analytical model of power generation system

The circuit diagram of the power generation system to be designed in this paper is shown in Fig. 1. In this circuit, the capacitors inserted between the PMSM (the generator) and the FBR are called phase-shift capacitors, and the capacitor connected to the DC side of the FBR is called a DC capacitor. The voltage equations for the PMSM and the power generation system are given by (1) and (2), respectively, and the d-axis current during operation can be calculated by (3) [7, 10],

$$\begin{pmatrix} v_d \\ v_q \end{pmatrix} = \omega \left\{ \begin{pmatrix} 0 \\ \psi_m \end{pmatrix} + \begin{pmatrix} 0 & -L_q \\ L_d & 0 \end{pmatrix} \begin{pmatrix} i_d \\ i_q \end{pmatrix} \right\} \tag{1}$$

$$\begin{pmatrix} v_{dr} \\ v_{qr} \end{pmatrix} = \begin{pmatrix} v_d \\ v_q \end{pmatrix} + \frac{1}{\omega} \begin{pmatrix} 0 & 1/c_r \\ -1/c_r & 0 \end{pmatrix} \begin{pmatrix} i_d \\ i_q \end{pmatrix} \tag{2}$$

$$i_d = \frac{-\omega^2 c_r \psi_m}{2\left(\omega^2 c_r L_d - 1\right)} + \frac{\sqrt{\omega^4 c_r^2 \psi_m^2 - 4\left(\omega^2 c_r L_d - 1\right)\left(\omega^2 c_r L_q - 1\right) i_q^2}}{2\left(\omega^2 c_r L_d - 1\right)} \tag{3}$$

where Ψ_m is the permanent magnet magnetic flux (Wb), L_d is the d-axis inductance (H), L_q is the q-axis inductance (H), v_d is the d-axis voltage (V), v_q is the q-axis voltage (V), i_d is the d-axis current (A), i_q is the q-axis current (A), ω is the angular frequency (electrical angle) (rad/s), c_r is the phase shift capacitor capacitance (F), v_{dr} is the rectifier d-axis voltage (V), and v_{qr} is the rectifier q-axis voltage (V). The generated power can be calculated from these quantities using (4).

$$v_d i_d + v_q i_q \tag{4}$$

In general, the torque of a PMSM increases monotonically with respect to the q-axis current, so by changing the q-axis current and calculating each quantity, it is possible to calculate each quantity when the torque changes, and to examine the relationship between the quantities. In the following, the characteristics of the power generation system are calculated using the above formula. This power generation system is characterized by forming a resonant circuit with the inductance of the PMSM and the phase shift capacitor, and basically operates at a rotation speed above a resonant rotation speed. The capacitance c_r of the phase shift capacitor can be calculated using the following formula with the resonant angular frequency ω_r corresponding to the resonant rotation speed.

$$c_r = \frac{1}{\omega_r^2 L_q} \tag{5}$$

In addition, when designing electrical equipment, the voltage to ground of each part is an issue in terms of insulation design, and the voltage depends on the grounding method. In this system, the main candidates are grounding at the neutral point (neutral grounding) and grounding at the negative pole (negative grounding). The grounding points are shown in Fig. 2.

In the case of negative grounding, the advantage is that the design of the inverter for DC EMUs can be used without modification. The advantage of neutral grounding is that the maximum voltage to ground of each part can be reduced. The maximum voltage to ground at the generator terminal is less than the sum of the positive pole voltage and the peak value of the phase-shift capacitor voltage, so the maximum voltage to ground for each part to be taken into account in the insulation design is roughly as shown in Table 1, depending on the grounding method.

In this paper, the design is based on neutral grounding, which can reduce the maximum voltage to ground. For optimization, a constraint is set so that the maximum voltage to ground calculated by the formula in Table 1 does not exceed the limit value of the ground insulation used in each part. Note that in the analysis, a sinusoidal AC is assumed, even though the AC voltage of the rectifier has a roughly rectangular voltage waveform. Therefore, the fundamental wave component contained in the rectangular wave is the value of the AC voltage calculated in the analysis. Therefore, the DC voltage of the rectifier can be calculated from the AC voltage of the rectifier. In that case, if the DC voltage (which is equal to the DC voltage of the traction inverter) is V_{dc} and the effective value of the fundamental wave component of the rectifier AC voltage (between terminals) is V_{ac}, the following relationship holds:

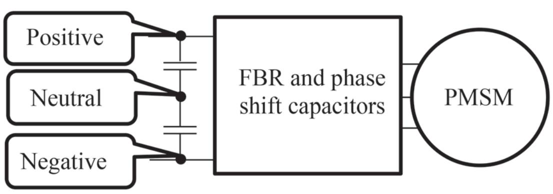

Fig. 2 Grounding location in DC power generation systems

Table 1 Grounding method and voltage to ground of terminals

Grounding method	FBR terminals	Generator terminals
Negative	V_{dc}	$V_{dc}+V_{cp}$
Neutral	$V_{dc}/2$	$V_{dc}/2+V_{cp}$

V_{dc} : Maximum voltage of DC link
V_{cp} : Maximum peak value of phase shift capacitor

$$V_{dc} = \left(\pi/\sqrt{6}\right) V_{ac} = \left(\pi/\sqrt{6}\right)\sqrt{v_{dr}^2 + v_{qr}^2} \tag{6}$$

Therefore, the DC voltage for a certain current vector can be calculated using (1), (2), and (6).

2.2 Design problem

To verify a design method for a power generation system, it is necessary to set it a specific design problem. Therefore, we designed a power generation system assuming a hybrid vehicle or a diesel-electric vehicle. First, we assumed the following design conditions:

- Maximum engine output: 2000 rpm-300 kW.
- Maximum engine speed: 2100 rpm.
- Idling speed of the engine: 800 rpm.
- Engine speed at which the engine is highly efficient (high efficiency speed): 1400 rpm.
- Maximum output at 1400 rpm: 220 kW.
- Generator's ground insulation: for 1500 V overhead lines.
- Rectifier ground insulation: for 600 V overhead lines
- Maximum DC voltage: 650 V.
- Number of poles of the PMSM: 12.

The maximum output of the engine was determined by referring to a diesel engine with a maximum output of approximately 300 kW that is widely used in Japan. The high efficiency speed was determined by referring to the bench test results of the reference engine. The maximum output at the speed was also determined by referring to the test results. When using an engine to drive a generator, it is desirable to set the target output at less than 90% of the actual output capacity of the engine to control the rotation speed, so that the maximum output determined as a design condition is a value smaller than the actual output capacity of the engine. The insulation design of the generator is assumed to be for 1500 V DC overhead lines, which is widely used for conventional lines in Japan. Furthermore, referring to existing diesel electric vehicles, the upper limit of the DC voltage was set to 650 V with neutral grounding. In this case, the voltage to ground is a half of 650 V, so there is no problem with the ground insulation of the rectifier at 600 V. The number of poles in the PMSM was set to 12, which is the maximum number of poles that can be achieved with a 36-slot stator core and integral-slot winding that is commonly used for railway traction motors in Japan.

3. Method for designing power generation system using multi-objective optimization

3.1 Overview of the proposed design method

The essential elements that make up this power generation system are a PMSM, phase shift capacitors, and an FBR. Of these, the size of the PMSM is thought to be roughly determined by the output. On the other hand, the dimensions and weight of the phase shift capacitors depend on the required capacitance, the maximum current and voltage during operation, etc. The dimensions of the rectifier also depend on the current and voltage during operation. In the design of a normal traction inverter or a PWM converter, the current and voltage during operation are mostly determined by the voltage of the power source and the output. However, in this power generation system, these quantities are determined by the characteristics of the PMSM and the capacitance of the phase shift capacitors. Therefore, whether the power generation system can be made smaller and lighter depends strongly on the characteristics of the PMSM and the capacitance of the phase shift capacitors. Therefore, in the design of this power generation system, the aim is to make the power generation system small and lightweight, and the design variables are the parameters representing the characteristics of the PMSM and the capacitance of the phase shift capacitors. The capacitance is calculated from the q-axis inductance of the PMSM and the resonant angular frequency using equation (5), and the upper and lower limits of the resonant angular frequency can be set from the engine rotation speed. Therefore, the resonant angular frequency is used as the actual design variable rather than the capacitance. Then, the objective functions to be aimed for in the design is the maximum current during operation related to the rectifier capacity, and the kVA capacity related to the dimensions and weight of the phase shift capacitors.

Since there are two objective functions, this problem is a multi-objective optimization problem. When there are two or more objective functions, a trade-off relationship may occur between them. In that case, the goal is to obtain a set of Pareto optimal solutions, rather than a single optimal solution (a solution means a combination of design variables). In the case of multi-objective optimization, a ranking function is used as an index to select the optimal solutions. The ranking function is a function that indicates how many solutions exist for a certain solution that are superior in all objective functions. The set of solutions for which the ranking function has a value of zero are Pareto optimal solutions. In the design of this system, the trade-off relationship between the maximum current and the kVA capacity of the phase-shift capacitor is clarified by the Pareto optimal solutions, and then the final design is selected from among these solutions.

3.2 Design variables, objective functions, and constraints

This section explains how we set up the optimization problem. First, the design variables that determine the characteristics of this power generation system are shown in Table 2.

Table 2 also shows the lower and upper limits that define the range in which the design variables vary in the optimization. The basic characteristics of a PMSM are expressed by three variables: the permanent magnet magnetic flux, the d-axis inductance, and the q-axis inductance. However, the saliency ratio, which is the ratio of the q-axis inductance to the d-axis inductance, depends on the shape of the rotor core and cannot be varied significantly. Therefore, we decided to use the saliency ratio as a design variable instead of the q-axis inductance, and to vary it within the range of 1 to 3, which is considered feasible from our experience. The upper limit of the permanent magnet magnetic flux was set to the value where the peak value of the terminal voltage of the induced voltage generated at the maximum rotation speed of 2100 rpm is 1500 V, and the lower limit was set to 1/10 of this value. The d-axis inductance value was set to a sufficiently wide range of lower and upper limits by referring to the inductance of past prototype PMSMs. The resonant rotation speed needs to be sufficiently higher than the idling rotation speed and lower than the high efficiency speed, so the lower limit was set to the resonant angular frequency corresponding to 900 rpm which is higher than the idling rotation speed, and the upper limit was set to the resonant angular frequency corresponding to the high efficiency speed of 1400 rpm. Next, the objective functions, which are the objective of optimization, are shown in Table 3.

Table 2 Design variables

Design variables	Unit	Lower limit	Upper limit
Permanent magnet magnetic flux	Wb	0.0804	0.8038
D-axis inductance	mH	0.1	10
Saliency ratio	—	1	3
Resonant angular frequency	rad/s	565.5	879.6

Table 3 Objective functions

Objective functions	Unit
Maximum current	A
kVA capacity of phase shift capacitor	kVA

Table 4 Constraints

Constraints	Unit	Lower limit	Upper limit
Output (high efficiency speed)	kW	220	—
Output (maximum output speed)	kW	300	—
DC voltage (high efficiency speed)	V	—	650
DC voltage (maximum output speed)	V	—	650
AC peak voltage to ground (high efficiency speed)	V	—	1500
AC peak voltage to ground (maximum output speed)	V	—	1500
Absolute value of the current vector	A	Ψ_m/L_d	$2\Psi_m/L_d$

As mentioned above, the kVA capacity of the phase shift capacitor and the maximum current related to the size of the rectifier are set as the objective functions. The kVA capacities are calculated for two operating points by calculating the phase shift capacitor voltage at each operating point using the capacitance and current, then multiplying the voltage by the current. The larger of these values is set as the phase shift capacitor kVA capacity of the objective function. Furthermore, the constraints are shown in Table 4.

First, since it is essential that the required output powers are achievable, this term is set as a constraint. When performing specific calculations, the value of the q-axis current that can achieve the required output is numerically obtained using (1) to (4). Then, the various quantities are calculated using this q-axis current and (1) to (4) etc. The upper limit of the DC voltage constraint is set to 650 V. As described later, optimization is performed to minimize the current, so the DC voltage basically tends to be as high as possible under the constraints. Therefore, it is sufficient to set only the upper limit, and there is no need for a lower limit. The constraint for the AC voltage to ground is set so that the maximum voltage to ground of the generator calculated in Table 1 is 1500 V or less. The maximum voltage to ground of the rectifier is automatically satisfied if the DC voltage constraint is satisfied, so there is no need to set it as a constraint. Finally, a constraint is set on the absolute value of the current vector during operation to ensure that the characteristics of the obtained PMSM are realizable. The lower limit value listed in Table 4 is the calculation formula for the current value corresponding to the magnetomotive force of the magnet and strongly correlated with the magnet quantity. This value was set as the lower limit because a design with a larger magnetomotive force of the magnet is likely to result in an excessive amount of magnet. Conversely, if the current vector is too large, the magnets are more likely to be demagnetized, so the upper limit was set at twice the lower limit, based on experience.

3.3 Multi-objective optimization results

As mentioned above, this optimization problem is a multi-objective optimization problem. It is known that genetic algorithms are suitable for such optimization problems, and this time we use NSGA-II [8, 9], which uses a genetic algorithm. The optimization calculation program was implemented using pymoo [8], a multi-objective optimization library written in Python. Figure 3 shows the results when the maximum population size was 100 and the number of calculation generations was changed to 100, 500, 1000, 1500, and 2000.

Figure 3 shows the Pareto optimal solutions obtained as a result of the multi-objective optimization, which show the trade-off relationship between the maximum current and the kVA capacity of the phase shift capacitor. Since both objective functions aim to be minimized, the individuals (solutions) on the lower left are better. The Pareto front, which is the curve drawn by the Pareto optimal solutions, has a convex shape to the lower left. A solution in the lower left of the figure that can simultaneously reduce two objective functions is a solution that cannot be obtained by single-objective optimization. In the 100th generation, there were individuals with a large maximum current despite a small phase-shift capacitor kVA capacity, and conversely, individuals with a large phase-shift capacitor kVA capacity and a small maximum current, but as the generations progressed, there was a tendency for individuals to concentrate in the lower left position. Since the values of the design variables and the objective functions are not significantly different between the individuals concentrated in the lower left, it is considered that each of these individuals has a design that is satisfactory. Therefore, among the results in the 2000th generation, the design of the individual with the smallest maximum current between the individuals concentrated in the lower left was selected as a design value. The design values are shown in Table 5. The design values in Table 5 are the values of the design variables of the selected individual, and the q-axis inductance is a value calculated using the d-axis inductance and the saliency ratio.

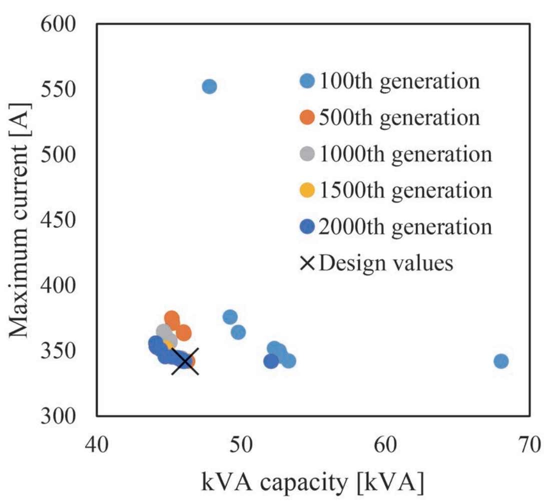

Fig. 3 Pareto optimal solutions

Table 5 Selected design values

Items		Unit	Values
Design Variables	Permanent magnet magnetic flux	Wb	0.379
	D-axis inductance	mH	0.643
	Q-axis inductance	mH	1.474
	Saliency ratio	—	2.293
	Resonant angular frequency	rad/s	565.5
Objective functions	Maximum current	A	341.8
	kVA capacity of phase shift capacitor	kVA	46.1

4. Verification of designed power generation system

4.1 Verification by analysis

This section describes how we checked the performance of the power generation system specified by the design values obtained in the previous chapter to verify the validity of the design. First, the calculation results of the current and voltage values at each operating point for the design values obtained using analytical formulas are shown in Fig. 4. The current vector curves when the load is changed at the two rotation speeds are shown in Fig. 5. Finally, changes in the current (phase current RMS value) and the voltage (terminal voltage RMS value) versus the output are shown in Fig. 6.

As can be seen in Fig. 4, both the current and voltage during operation are larger at maximum output. As shown in Table 5, the current value at maximum output is 341.8 A, and the DC voltage value is 650 V, which was given as an upper limit constraint. The generator voltage is not much different from the rectifier AC voltage, and it is thought that the voltage of the phase shift capacitor is kept low to reduce the kVA capacitance of the phase shift capacitor. Secondly, in Fig. 5, we also show the curves corresponding to the maximum torque per ampere (MTPA) [10, 11], which is the operating state where the torque per current is maximum. In this design, the operation is relatively close to the MTPA at both rotation speeds, and we can expect operation at an operating point with low current and high efficiency. However, at the maximum output rotation speed, the output is approaching the output limit where the q-axis current does not increase any further. Since the possibility of reaching the output limit point increases as optimization proceeds, it is better to keep the output constraint condition at a large value during optimization because the design of the actual machine must have a margin. In Fig. 6, there is a tendency for the rectifier voltage not to

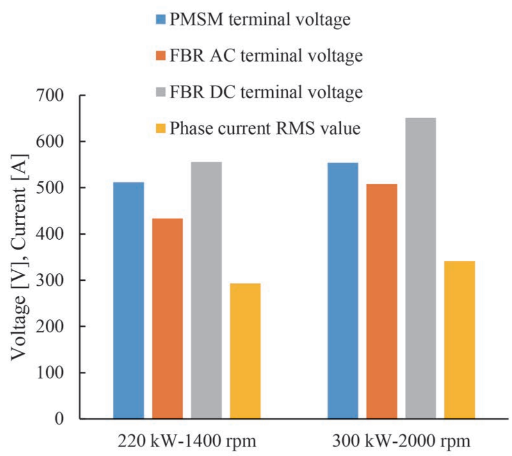

Fig. 4 Operating current and voltage

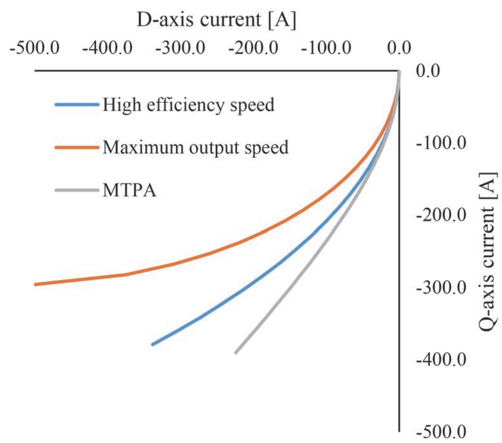

Fig. 5 Current vector loci when load changes

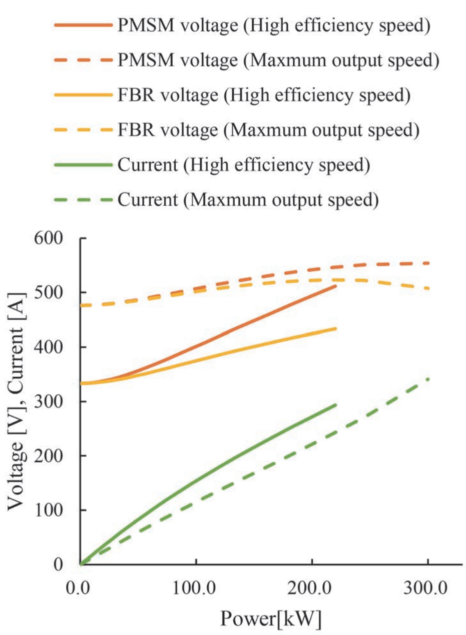

Fig. 6 Current and voltage versus load

change significantly even if the load increases at each rotation speed, so it is thought that a drive system can be built without problems by combining this power generation system with an ordinary traction inverter for DC overhead lines.

4.2 Verification by simulation

A simulation is then carried out using a circuit simulator to confirm the operation of the power generation system including the rectifier. A DC capacitor must be placed on the DC side of the rectifier. The capacitance of the DC capacitor sometimes has a significant effect on the operation of the power generation system. This time, we used a configuration in which two 1 mF DC capacitors are connected in series. The circuit simulator used is SystemModeler [12], which is a simulation environment that uses the Modelica language [13]. Figure 7 shows the model used for the simulation.

In Fig. 7, “smpm” is an interior permanent magnet synchronous generator, which rotates at a constant speed due to the “constantSpeed” element. “IdealDiode” and “IdealDiode1” are diodes, and the notation “m=3” indicates that there are three phases. In other words, “IdealDiode” and “IdealDiode1” represent six diodes, and a FBR is constructed. “Capacitor1,” located between the diodes and the generator, is also written as “m=3,” indicating phase-shift capacitors for three phases. The resistor at the top is a load resistor, and the capacitors below are the DC capacitors. Between these and the diodes are elements written as “star” and “star1,” and the three phases are connected to the DC section by this star-connection element. The neutral point of the DC section is grounded to the ground element, which is used as a reference for the potentials. The simulation results shown below were carried out under two operating conditions: maximum output at the high efficiency speed (1400 rpm, 220 kW) and maximum engine output (2000 rpm, 300 kW). The load was adjusted by the load resistance value. Figure 8 to 10 show the calculation results for maximum output at the high efficiency speed (1400 rpm, 220 kW). The simulation was run for 0.2 seconds, and each figure plots the last 0.008 seconds.

Figure 8 shows the current and voltage of the PMSM. The cur-

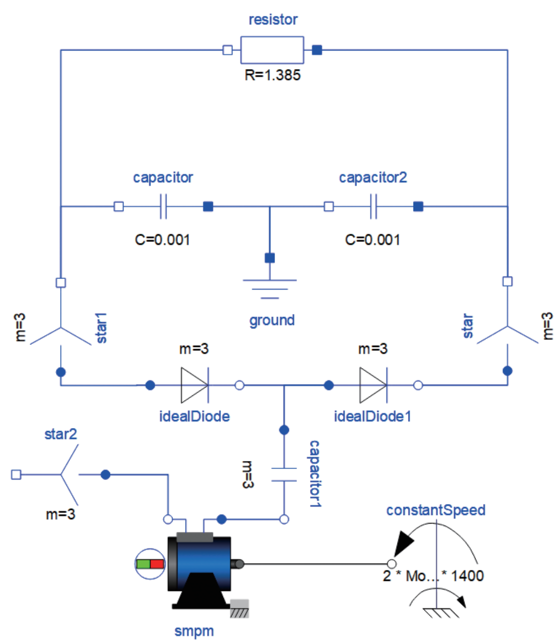

Fig. 7 Simulation model

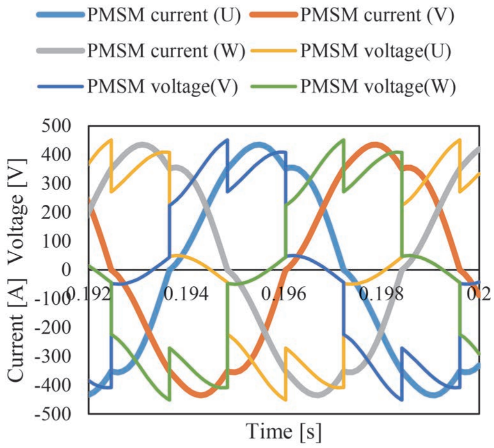

Fig. 8 Generator current and voltage calculation results (1400 rpm-220 kW)

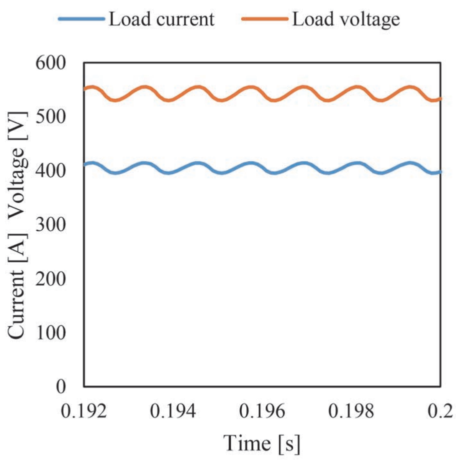

Fig. 9 Load resistance current and voltage calculation results (1400 rpm-220 kW)

rent value is roughly a three-phase symmetrical sinusoidal wave, but the voltage value changes suddenly at the timing of diode switching. Figure 9 shows the current and voltage of the load resistance. There are six pulsations per cycle, which is characteristic of a FBR, but both the current and voltage are almost constant. The average current is 404 A, the average voltage is 542 V, and the generated power is about 220 kW, which is roughly consistent with the analysis results. As shown in Fig. 10, the terminal potential of the PMSM is less than 600V, which is low enough in relation to the voltage limit.

The calculation results at the maximum engine output (2000rpm, 300kW) are shown in Fig. 11 to 13. Again, the simulation was run for 0.2 seconds, and the final 0.008 seconds are plotted.

At maximum output, as in the case of high efficiency speed, the generating system operates as expected, and the generator current value is almost consistent with the analysis. The average current and voltage of the DC side are 493 A and 606 V, which are slightly lower than the analysis, but are roughly consistent. The voltage to ground of each part meets the constraints with a margin and is within a range that does not pose any problems in terms of the insulation configuration. Although the constraint on the AC voltage to ground was set at 1500 V, the design was such that insulation systems for 600 V would be acceptable from the viewpoint of voltage to ground.

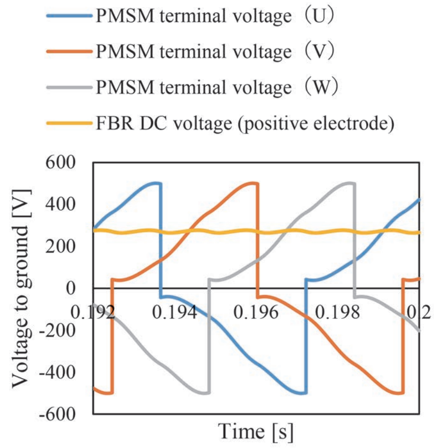

Fig. 10 Voltage to ground calculation results (1400 rpm-220 kW)

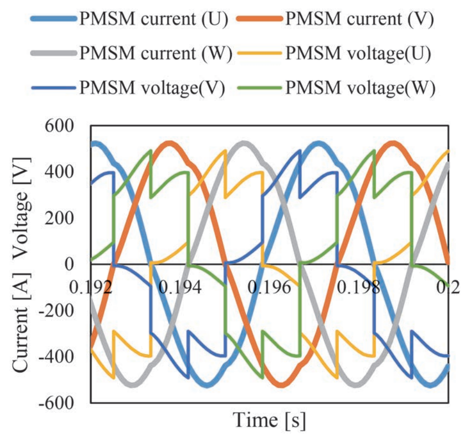

Fig. 11 Generator current and voltage calculation results (2000 rpm-300 kW)

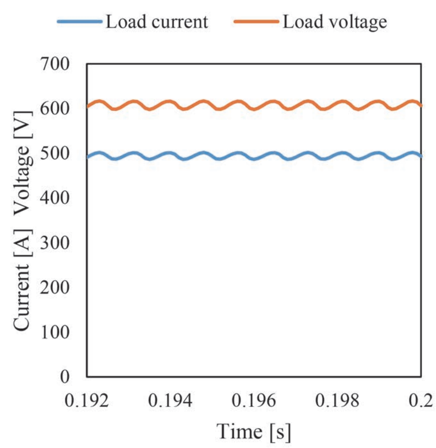

Fig. 12 Load resistance current and voltage calculation results (2000 rpm-300 kW)

5. Conclusion

In this paper, we proposed a method for designing a power generation system in which a phase-shift capacitor is inserted between a PMSM and an FBR, by setting the machine constants of the

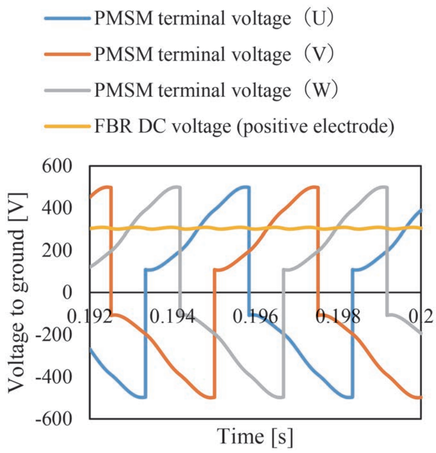

Fig. 13 Voltage to ground calculation results (2000 rpm-300 kW)

PMSM as design variables and performing multi-objective optimization to reduce the current capacity of the rectifier and the kVA capacity of the capacitors. The application of this method to the design of a diesel-electric vehicle enabled us to obtain a combination of machine constants that simultaneously reduces both the current capacity of the rectifier and the kVA capacity of the phase shift capacitors using a multi-objective optimization method. Furthermore, we performed a simulation to confirm the performance of a system using a PMSM with the optimized machine constants and confirmed that the design objectives of securing the target output and the limit of voltage to ground could be achieved, thus demonstrating the effectiveness of the proposed design method. Note that in this study, the machine constants of the PMSM were treated as design variables, but in general, the machine constants are determined as a result of the design and are not freely determined. It is also known that the values of the machine constants vary depending on the operating current due to the influence of magnetic saturation in the iron core. In the future, we plan to conduct a further design study of the PMSM and confirm whether the target machine constants and system operation can be achieved.

References

[1] Nakagawa, T., Morita, E., Nishizawa, H., and Numazaki, M., “Improvement of diesel electric locomotive traction system,” presented at the *7 th World Congress on Railway Research*, Montreal, Canada, June 4-8, 2006.

[2] Watanabe, R., “Overview of the GV-E400 series new diesel-electric railcars (mass-production prototype cars),” *Japanese Railway Engineering*, Vol. 59, No. 1, pp. 5-8, 2019.

[3] Umeshita, K., Yasumori, K., “Outline of battery-mounted diesel electric hybrid vehicle “YC1 Series”,” *Japanese Railway Engineering*, Vol. 59, No. 3 pp. 13-15, 2019.

[4] “JR Central launches hybrid train with remote monitoring,” *Railway Gazette International*, 23 March, 2022.

[5] Kondo, M., “Comparison of Two Types of DC Power Generation Systems with Permanent Magnet Synchronous Machines and Full-Bridge Rectifiers Using Resonant Circuits,” *IEEJ Journal of Industry Applications*, 2022, Vol. 11, No. 4, pp. 573-581, 2022.

[6] Kondo, M., “DC Generation System with Permanent Magnet Synchronous Machine and Series Resonant Circuit,” Papers of Technical Meeting, *IEE Japan*, MD-21-081/RM-21-045/VT-21-006, pp. 33-38, 2021 (in Japanese).

[7] Kondo, M., “Analyses on DC power generation systems consist of an IPMSM and a series resonant circuit,” Papers of Technical Meeting, *IEE Japan*, MD-23-076/RM-23-044//VT-23-006, pp. 27-32, 2023 (in Japanese).

[8] Blank, J., and Deb, K., “pymoo: Multi-Objective Optimization in Python,” in IEEE Access, vol. 8, pp. 89497-89509, 2020.

[9] Deb, K., Pratap, A., Agarwal, S. and Meyarivan, T. “A fast and elitist multiobjective genetic algorithm: nsga-II,” *Trans. Evol. Comp*, 6(2): 182-197, April 2002.

[10] Morimoto, S., Takeda, Y., Hirasa, T. and Taniguchi, K., “Expansion of Operating Limits for Permanent Magnet Motor by Current Vector Control Considering Inverter Capacity,” *IEEE Transactions of Industry Applications*, Vol. 26, No. 5, pp. 866-871, 1990.

[11] Jahns, T.M., Kliman, G.B., Neumann, T.W., “Interior Permanent-Magnet Synchronous Motors for Adjustable-Speed Drives,” *IEEE Transactions of Industry Applications*, Vol. IA-22, No. 4, pp. 738-747, 1986.

[12] Wolfram system modeler, https://www.wolfram.com/system-modeler

[13] Modelica, https://modelica.org

Author

Minoru KONDO, Ph.D.
Senior Chief Researcher, Head of Traction Systems Laboratory, Vehicle Technology Division
Research Areas: Traction System Design, Condition Monitoring

Numerical Analysis Method for Analyzing Seismic Vehicle Behavior Up to and After Derailment

Keiichi GOTO
Structural Mechanics Laboratory, Railway Dynamics Division

Kohei IIDA
Vehicle Mechanics Laboratory, Railway Dynamics Division

Munemasa TOKUNAGA
Structural Mechanics Laboratory, Railway Dynamics Division

The authors are conducting research with the aim of establishing a numerical analysis method capable of evaluating vehicle behavior before and after derailment of a train set during an earthquake. In this paper, as a basic study, an analysis method is proposed that can represent seismic vehicle behavior before and after the derailment of a single vehicle in a stationary state. Then, in order to consider the coupling of multiple vehicles, the proposed method is also extended to include dynamic models for connecting members between vehicles such as couplers and inter-car yaw dampers. Furthermore, the influence of the interaction between vehicles on the derailment limit is investigated through trial calculations.

Key words*: *earthquake, derailment, train set, coupler, inter-car yaw damper

1. Introduction

In recent years, there have been derailments of Shinkansen and other trains due to frequent large earthquakes as shown in the reference [1]. The derailment of high-speed trains may lead to large scale damage. Thus, countermeasures for tracks and vehicles [2, 3] are being developed to prevent derailed vehicles from running too far off the tracks or on to adjoining tracks with oncoming trains. However, taking an experimental approach to study this phenomenon is difficult. There are studies which analyze vehicle behavior during an earthquake, including post-derailment [4] using numerical analysis methods. However, such studies only express the phenomenon by replacing the shapes of the rails and wheels with simple shapes such as rectangles. As such, currently, there is no established method to assess the behavior of vehicle in the moments leading up to and after derailment.

The objective of this study is therefore to establish such an analysis method capable of evaluating the behavior of vehicles before and after derailment during an earthquake. As a basic study to achieve this objective, we propose an analysis method that can represent vehicle behavior of a single stationary vehicle before and after derailment. In addition, we extend the proposed model by considering the dynamic models for connecting members between vehicles such as couplers and inter-car yaw dampers [5, 6], making it possible to represent the behavior of a multi-car train. Moreover, we will examine the influence of the interaction between vehicles on derailment behavior by trial calculation.

2. Proposed analysis method of train behavior during an earthquake

In this section, we explain the proposed analysis method that can represent the behavior of a stationary single car train during an earthquake in the moments leading up to and after derailment. We then extend this model by considering the dynamic model for the connecting members between vehicles, making it possible to represent the behavior of a multiple-car train. The present method is developed using the nonlinear structural analysis software Ansys LS-DYNA (R13.1.1) [7].

2.1 Methods for analyzing the behavior of single car train in moments leading up to and after derailment during an earthquake

2.1.1 Overview of the analysis method

Because the phenomenon in question during an earthquake can last for a long period time, from tens to a few hundred seconds, modelling it requires ensuring a certain level of accuracy while reducing the computational burden as much as possible. On the other hand, when evaluating the vehicle behavior that is of interest in this study, it is critical to properly account for the contact phenomenon between complex shapes of parts on the vehicle side and the track side, as typified by wheel / rail contacts.

Thus, in this study, we base the modeling of the vehicle on the multibody dynamic theory, which provides a low computational load and has been verified as appropriate for the evaluation of the behavior of railway vehicles during an earthquake [8]. In addition, we developed a method to represent the contact phenomenon between a vehicle and track parts (e.g. the rail and the track slab) before and after derailment using rigid finite elements. We show the constructed model in Fig. 1. As a basic study, in the present study we constructed a model that includes the vehicle, track (rail, track slab, CA mortar, concrete roadbed) and the superstructure, assuming a situation where a single car train is stopped on a slab track on an elevated bridge.

2.1.2 Modeling the vehicle

Figure 2 shows the dynamic model of the vehicle. In the model, we considered a carbody of a vehicle, bogie frames, and wheelsets as rigid bodies and connected these rigid bodies with springs and dampers. In an actual vehicle, stoppers are installed between vehicle

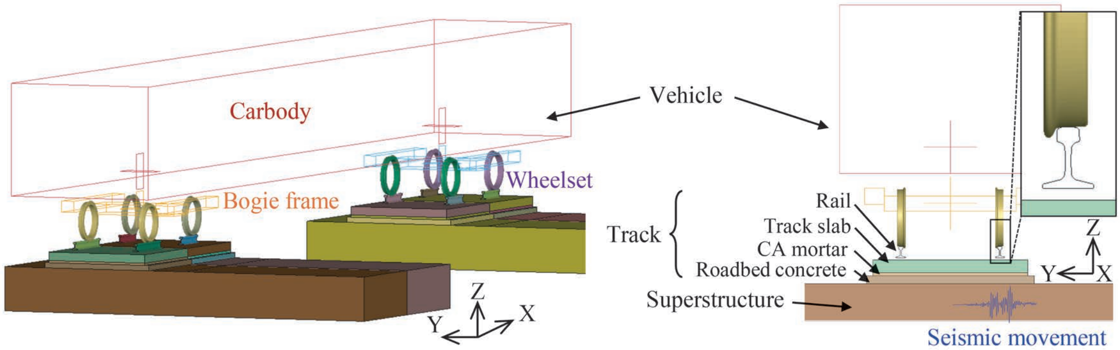

Fig. 1 Analysis model based on the proposed method

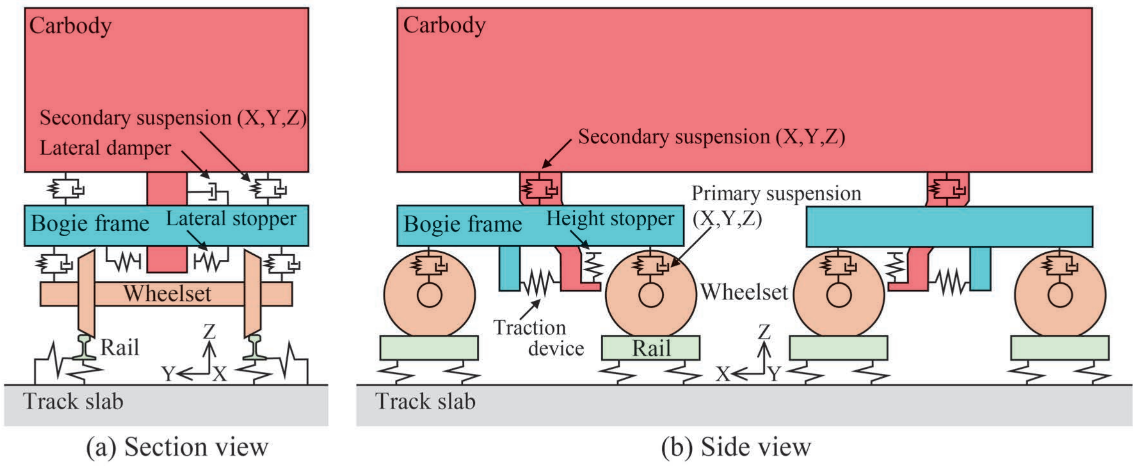

Fig. 2 Dynamic model of the vehicle

components to suppress the occurrence of significant relative displacement. We therefore included this in our model. The right and left wheels, which are part of the wheelset, are modeled separately using rigid finite elements (average element length of approximately 10mm), which replicate the wheel shape in detail to represent the contact. We do so to represent the contact with the rail and the fall onto the tack slab after derailment (see Fig. 1). It should be noted that since we assume that the vehicle is in a stationary state, we constrained the wheelset rotational degree of freedom in the circumferential direction of the wheel (Y axis rotation: the coordinate system is shown in Fig. 1 and Fig. 2).

2.1.3 Modeling the track and the superstructure

As for the track and the superstructure, we modeled each of them individually just below each wheelset using rigid finite elements to represent their shapes, as shown in Fig. 1. We used rigid bonding between the track slabs, CA mortars, roadbed concrete, and the superstructure. We used linear springs and dampers that are equivalent to fastening devices, to connect the rails to the track slabs. We replicated the shape of the rails in detail to account for the contact with the wheels. Input of seismic movement was set as forced displacement to the superstructure.

2.1.4 Modeling the wheel and track contact

We performed three-dimensional contact calculations between the finite elements that replicate each shape in detail to model the contact between the wheel and the rail and also the contact between the wheel and the track slab after derailment. We represented modeling of the contact force in the normal direction of the contact surface using the penalty method. Coulomb friction (with friction coefficient set to 0.3) was used to model the contact force in the tangential direction of the contact surface. It should be noted that, in this study, we do not take into consideration the influence of the creep force generated by the rotation of the wheels, since we assume that the vehicle is in a stationary state.

2.2 Method for the analysis of a multiple-car train during an earthquake

2.2.1 Overview of the analysis method

In this section, we improve the single-car train analysis method established in Section 2.1 to a method capable of computing the behavior of a multiple-car train during an earthquake by inserting a dynamic model that expresses the connecting members between vehicles, which allows the connection of multiple vehicles. Figure 3 shows an example of the connecting members between vehicles in a Shinkansen train [6]. Couplers and inter-car yaw dampers are considered as the connecting members in this study, as shown in the figure. The details of this dynamic model are explained below.

2.2.2 The dynamic model of the coupler

Figure 4 shows the conceptual diagram for the dynamic model

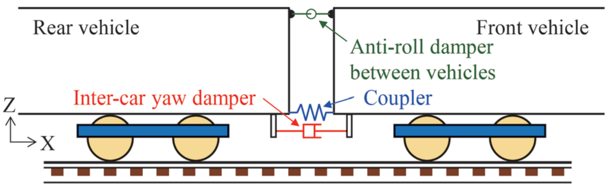

Fig. 3 Example of connecting members between vehicles in a Shinkansen

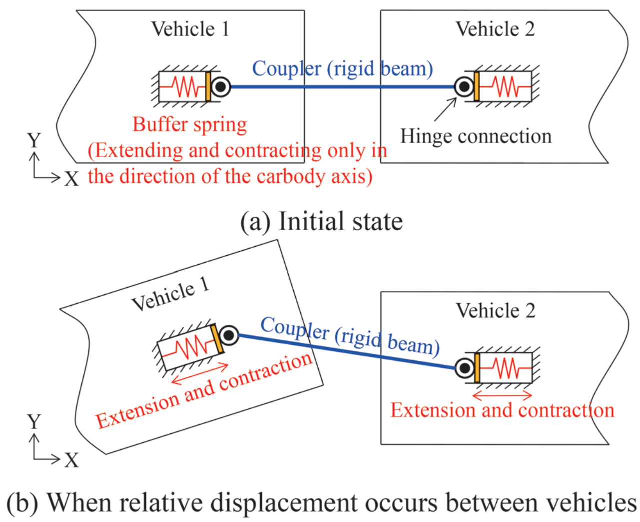

Fig. 4 Dynamic model of the coupler

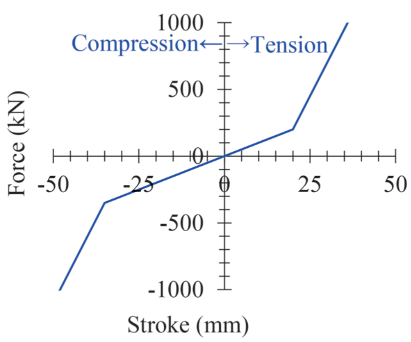

Fig. 5 Characteristics of the buffer spring in the model

of the coupler. We constructed the dynamic model of the coupler using a hinge connection between the non-linear spring, which represents the characteristics of the buffer fixed onto each carbody, and the rigid bar, which connects the buffers on each carbody. We assume that the buffer springs always follow the movements of the carbody, expanding and contracting only in the direction of the carbody axis. In addition, we use a multilinear model where the spring characteristics are defined by the force and the stroke. Figure 5 shows the characteristics of the buffer springs used in this study. Based on the characteristics of the shock absorber springs used in Shinkansen [9], we set ours as a bilinear type, which has higher rigidity on the extension side.

2.2.3 The dynamic model of the inter-car yaw damper

Figure 6 shows the conceptual diagram for the dynamic model

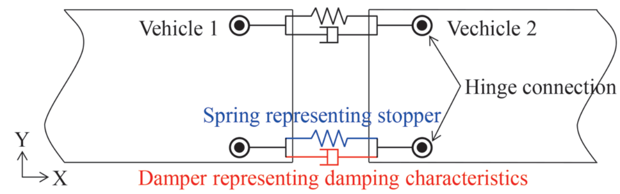

Fig. 6 Dynamic model of inter-car yaw damper

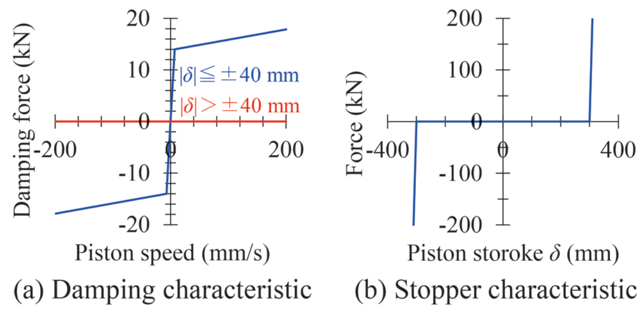

Fig. 7 Characteristics of the inter-car yaw damper in the model

of the inter-car yaw damper. We constructed the inter-car yaw damper by arranging in parallel a damper representing damping characteristics and a spring representing the stopper characteristics and connecting both ends by hinges to an arbitrary position on each vehicle.

Figure 7 shows the damping characteristics and the stopper characteristics of the inter-car yaw damper used in this study. We set the damping characteristics referencing the catalog [10]. However, for the inter-car yaw damper we characterized, no damping force is generated when the piston stroke δ exceeds the threshold (in this study the threshold is ±40 mm), as shown in Fig. 7(a). We do so because there is a system that releases the hydraulic pressure so that no damping force is generated when the yaw damper piston stroke becomes large when turning a curve. It should be noted that we assume that the damping force returns when the piston stroke value is back within the threshold after the threshold has been exceeded. For the characteristic of the stopper spring, we assume that the stopper will operate when the piston stroke exceeds 300 mm, as shown in Fig. 7(b).

3. Evaluation of the influence of the interaction between vehicles on the derailment limit

In this section, we consider the influence of the interaction between vehicles on the derailment limit that occurs due to the presence of the connecting members. We do this by conducting an excitation test of a three-car train set using the analysis method proposed in Section 2.

3.1 Analysis method

Figure 8 shows the analysis model that we used for the examination. The multiple-car train set analysis model consists of three coupled vehicles (hereinafter, multiple-car model), which is constructed by lining up three vehicles of the single-car model in a stationary state and inserting the dynamic model of the connecting

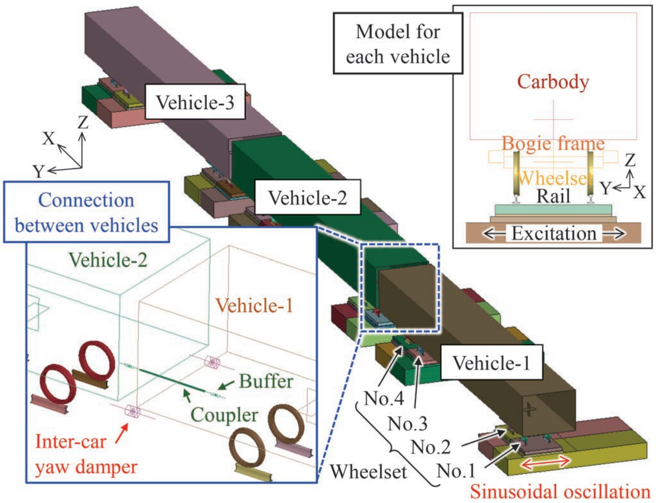

Fig. 8 The three-car analysis model used in the present examination (Example of when excitation is applied only to Vehicle-1)

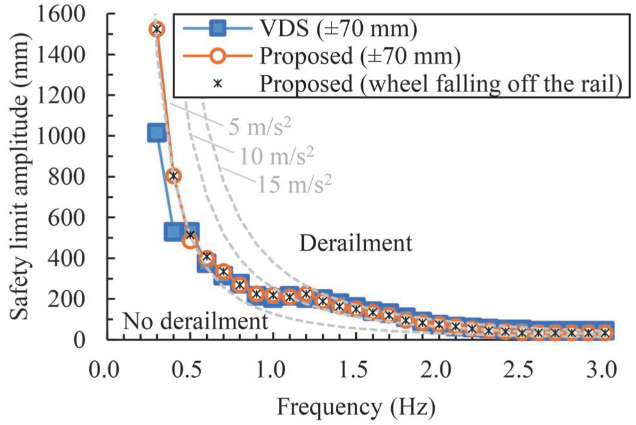

Fig. 9 Derailment limit diagram for five sinusoidal oscillations (single car model)

members (the couplers and the inter-car yaw dampers) between each vehicle, as described in the previous section. We used the dynamic model and the characteristics of the connecting members as described in Section 2.2.

For the excitation condition, three different cases are considered: when the same excitation is applied to all three vehicles, when the excitation is applied only to Vehicle-1 (lead-vehicle), when the excitation is applied only to Vehicle-2 (middle-vihicle). An extreme excitation condition was deliberately set to evaluate the influence of the interaction between vehicles, although these are not conditions that can occur in reality. The excitation was performed by inputting five periods of sinusoidal oscillations in the lateral direction (Y-axis direction: see Fig. 1 and Fig. 8 for the coordinate system) with a constant frequency and amplitude. The sinusoidal wave frequency was between 0.5 Hz and 3.0 Hz and increased by 0.1 Hz and the amplitude was increased by 5 mm to determine whether derailment occurred. The relative lateral displacement of ±70 mm between wheel and rail [11] was used as the criterion for derailment during an earthquake. This value is at present the threshold to determine the criterion for derailment during an earthquake. Here, the computation time for the three-car train model was about 45 minutes per case when using parallel computing at 0.5 Hz (15 seconds duration) on a dual-core desktop computer.

In addition to the above, we also performed a sinusoidal oscillation analysis with only one vehicle to evaluate the difference in vehicle behavior with the multiple-car model. Furthermore, we performed an oscillation analysis under the same conditions (five sinusoidal oscillations between 0.3 Hz and 3.0 Hz) as the Vehicle Dynamics Simulator (VDS) [8] to verify the validity of our proposed method. The validity of VDS has been verified by comparison with the results of a full-scale shaking table test [12]. We compared the results with those of the proposed method. Here, VDS simulates the vehicle movement up until just before derailment and the computation ends when one of the wheels reaches the derailment criteria explained above.

3.2 Results of the examination

3.2.1 Verification of validity of the proposed method

Figure 9 shows the comparison between the VDS derailment limit diagram of the single-car model and our proposed method. Here, the derailment limit diagram shows the vibration amplitude just before reaching derailment for each excitation frequency. In the figure, we also show the lines for each acceleration amplitude (5 m/s^2, 10 m/s^2 and 15 m/s^2) to serve as a guide to know which combination of frequency and amplitude corresponds with which level of acceleration input. From the figure we can confirm that the limit value is slightly different between the VDS and our proposed method at 0.3 Hz and 0.4 Hz, respectively, but the values are well matched for the other excitation frequencies. Therefore, this fact leads us to say that a derailment limit diagram that is equivalent to that of VDS can be computed using our proposed method.

In additionally, Fig. 9 shows not only the results when the derailment criterion is set at a relative lateral displacement of ±70 mm between wheel and rail, but also the results when the wheels fall off the rail. From the figure, it can be seen that the overall results of both cases are the same. This means that derailment occurs in most cases when the relative lateral displacement between wheel and rail reaches ±70 mm. This indicates the validity of the conventional derailment criterion.

3.2.2 Evaluation of the influence of the interaction between vehicles

Figure 10 shows the time-history waveform of vehicle response for Vehicle-1 in the three-car train model (excitation applied only to the Vehicle-1, the excitation frequency: 0.5 Hz, the excitation amplitude: 520 mm) in a way that compares with the single-car model. Focusing on the relative vertical displacement between wheel and rail as shown in Fig. 10 (a), a significant increase in response over time can be observed only in the single-car model while almost no relative vertical displacement occurs in the multiple-car model. It can be seen that, in the single-car model, a displacement of around -180 mm occurs around 12 seconds. This is due to the derailment of the wheelset, it can be seen that our method can represent the sequence of vehicle behavior before and after derailment. In addition, it is possible to confirm that displacement rapidly increases around 12 seconds before derailment for the lateral displacement shown in

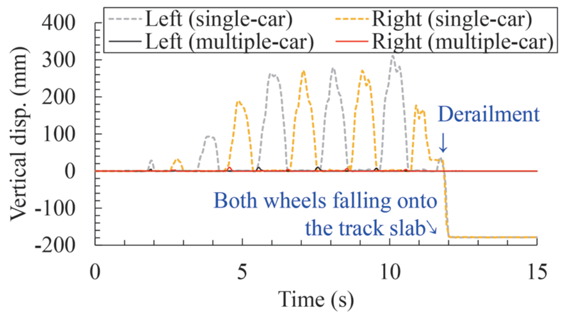

(a) Relative vertical displacement between wheel and rail

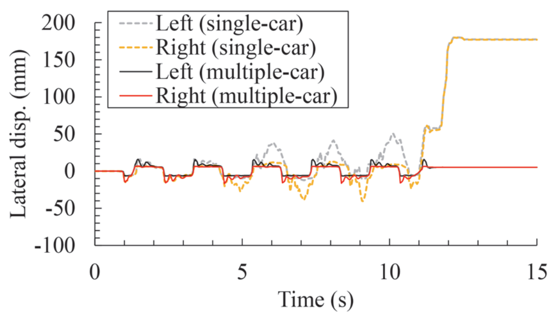

(b) Relative lateral displacement between wheel and rail

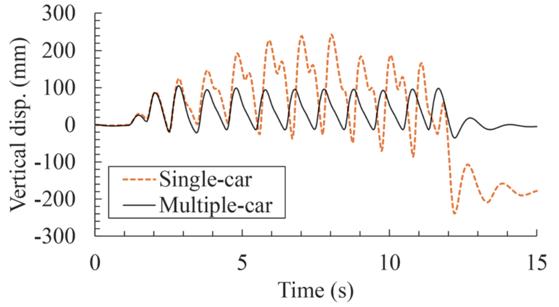

(c) Vertical displacement of the center of gravity of the carbody

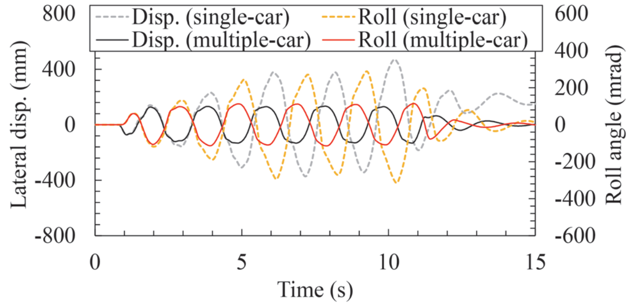

(d) Lateral displacement and roll angle of the center of gravity of the carbody

Fig. 10 Comparison of vehicle behavior in the single-car model and multiple-car model (when excitation is applied only to Vehicle-1, excitation frequency: 0.5 Hz, excitation amplitude: 520 mm)

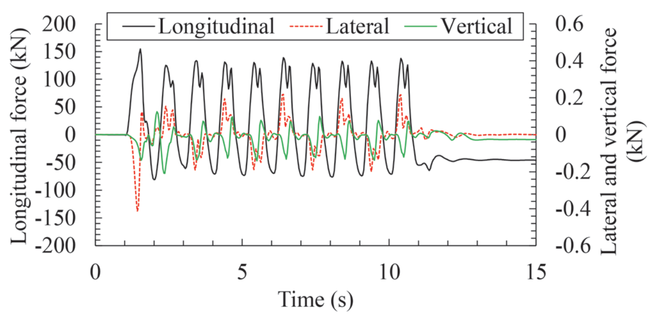

Fig. 11 Time-history waveform of the buffer spring

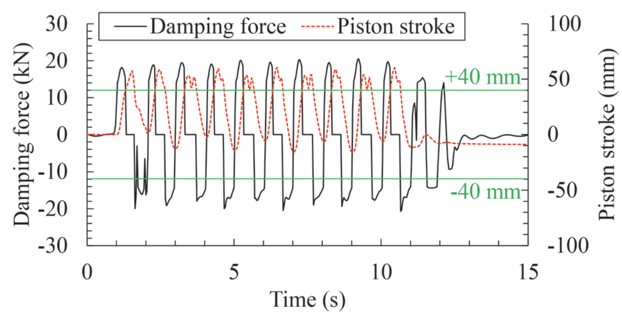

Fig. 12 Time-history waveform of the inter-car yaw damper

Fig. 10 (b).

Next, we focus on the vertical displacement of the center of gravity of the carbody in Fig. 10 (c) as well as the lateral displacement of the center of gravity of the carbody and roll angle in Fig. 10 (d). From the figures, it is possible to verify a phenomenon in which the amplitude in each response increases gradually over time in the single-car model. In contrast, in the multiple-car model, the vertical and lateral responses are generally in agreement up to around 3 seconds when the first sinusoidal wave ends, then after that the amplitude in each response remains constant overall over time. In addition, it is also possible to see the difference in oscillation periods between the multiple-car model and the single-car model, where the oscillation period in the multiple-car model is shorter than that of the single-car model.

Figure 11 shows the time-history waveform of the buffer spring on Vehicle-1 side in the coupler between Vehicle-1 and Vehicle-2 in the multiple-car model (excitation applied only to Vehicle-1, excitation frequency: 0.5 Hz, excitation amplitude: 520 mm). The time-history waveforms are shown by separating into longitudinal, lateral and vertical directions (X-axis, Y-axis, and Z-axis in Fig. 8, respectively). Focusing on the longitudinal direction, it can be seen that the force amplitude on the positive side (extended side) is larger than on the negative side (compressed side). This corresponds to the excitation condition under which a pull force is generated between vehicles; that is, the relative discrepancy between vehicles increases on both Vehicle-1 and Vehicle-2 by oscillating only Vehicle-1. It should be noted that forces on the lateral and vertical directions are extremely small in contrast to the force on the longitudinal direction. This is because the forces other than those in the longitudinal direction of the carbody are absorbed by the hinge (see Fig. 4), which is the connection point between the coupler and the buffer spring, instead of the buffer spring.

Figure 12 shows the time-history of the damping force of the inter-car yaw damper between Vehicle-1 and Vehicle-2 and the piston stroke in the multiple-car model (excitation applied only to Vehicle-1, excitation frequency: 0.5 Hz, excitation amplitude: 520 mm). In the figure, we also show the ±40 mm threshold line of the piston stroke, at which point there is no damping force due to oil

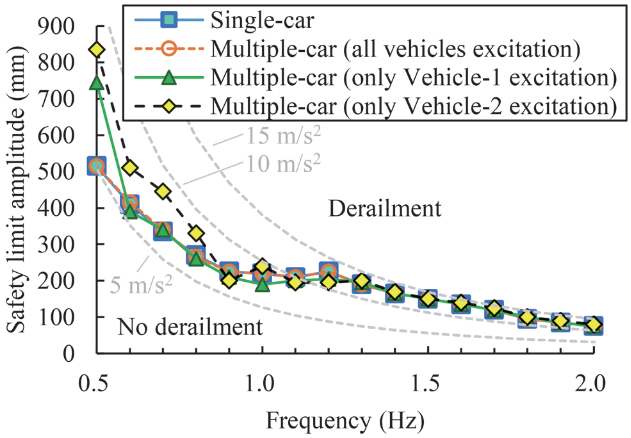

Fig. 13 The influence of the interaction between vehicles on the derailment limit

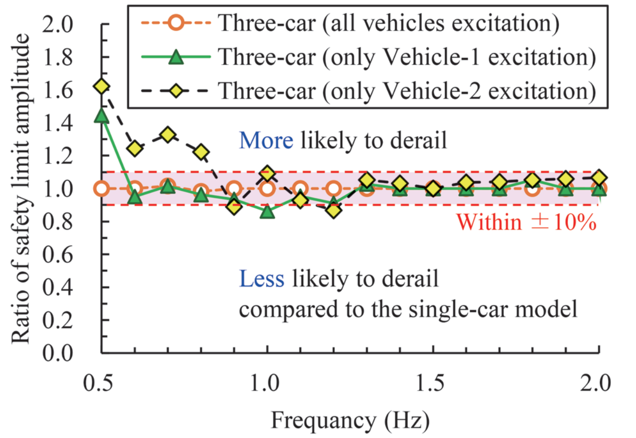

Fig. 14 Ratio of derailment limit amplitude in contrast to the single-car model

pressure release. The figure shows that the piston stroke exceeds the +40 mm line multiple times and that the damping force becomes zero at these instances. It can also be seen that the damping force occurs again when the piston stroke enters the ±40 mm range afterwards.

To evaluate the influence of the interaction between vehicles on the derailment limit, Fig. 13 shows a comparison of derailment limit diagram for oscillating frequency between 0.5 Hz and 2.0 Hz for the following cases: excitation in the single-car model, excitation in-phase excitation of all cars in the multiple-car model, excitation of only Vehicle-1 (lead-vehicle) in the multiple-car model, and excitation of only Vehicle-2 (middle-vehicle) in the multiple-car model. It should be noted that derailment occurred on the vehicles that were excited under all excitation condition. We also show a diagram that converts Fig. 13 into the ratio of a single-car derailment limit amplitude in Fig. 14 so that it is easier to capture the influence of the interaction between vehicles. This diagram means that, when the amplitude ratio is larger than 1.0, it is harder to derail compared to the single-car case and that, when the amplitude ratio is smaller than 1.0, it is easier to derail compared to the single-car case. From both figures, it is possible to see that the results of the excitation of only one car is mostly consistent with those of the in-phase excitation of the multiple-car train. This result is consistent with those in existing study [6]. It can also be seen that, when oscillation is added only to the first car (lead-vehicle) in the multiple-car model the limit value is mostly the same compared to the single-car model while the value tends to decrease slightly when it is 1.2 Hz or below. In contrast, in the case of excitation of only Vehicle-2 (middle-vehicle) in a multiple-car train, the limit value is reduced at some excitation frequencies but, overall, the limit value tends to increase compared to the case of only one car. In the figure, we show the range in which the ratio of the derailment limit between the single-car model and the multiple-car model is ±10%. It can be confirmed that it is generally within this range. In the present study we deliberately set extreme excitation conditions to make it easier to understand the impact of interaction between vehicles. In the case of a real earthquake, the degree of influence is expected to be even smaller.

The examination results shown above are only an example. It should be noted that it may be possible that the influence of the interaction between vehicles on derailment limits may differ greatly depending on the characteristics of the vehicle and the characteristics of the connecting members between vehicles.

4. Conclusions

This study aimed to establish an analysis method that can evaluate the behavior of vehicles during an earthquake in the moments leading up to and after derailment. As a basic study towards this objective, this paper proposes two methods: one which can analyze vehicle behavior before and after derailment in a single stationary state, the other which can express the behavior of a multiple-car train. In addition, we examined the influence of the interaction between vehicles on the derailment limit during an earthquake using the proposed method. We summarize our study as follows:

(1) We proposed an analysis method that combines a multi-body for representing vehicle motion and rigid finite elements for representing the contact between vehicle members and track members. This method can efficiently calculate the behavior of a single-car train in a stationary condition during an earthquake before and after derailment.

(2) We proposed a new dynamic model that represents the coupler and the inter-car yaw damper, which are the connecting members between vehicles, and we incorporated this model into the single car method explained above for the sake of representing the behavior of a train set during an earthquake.

(3) We examined the influence of the interaction between vehicles on the derailment limit through the analysis of the three-car train modeled by the above method. In the case of in-phase excitation of all vehicles in a multiple-car train, the derailment limit is mostly the same as the single-car case. In the case of excitation of only the middle car in the multiple-car train, the derailment limit is on an increasing trend compared to the single-car case.

The findings explained above are only an example. It is expected that the influence of the interaction between vehicles on derailment limits may differ greatly depending on the characteristics of the vehicle, the characteristics of the connecting members between vehicles, the excitation conditions and other factors. To clarify the extent of these influences, the validity of the analysis method constructed in this study have to be verified. Moreover, it is necessary to conduct various parametric studies under real world conditions. In the future, we plan to study vehicle behavior after derailment since the interaction between vehicles has a large influence on the behavior of the vehicle after derailment.

References

[1] Ogura, M., "The Niigata Chuetsu Earthquake – Railway Response and Reconstruction," *Japan Railway & Transport Review*, No. 43/44, pp. 46-63, March, 2006.

[2] Kumagai, N., "Preparing for Major Earthquakes," *Japan Railway & Transport Review*, No. 60, pp. 34-41, October, 2012.

[3] Asanuma, K., Sogabe, M., Watanabe, T., Okayama, J. and Wakui, H., "Development of Ballasted Ladder Track Equipped with a Vehicle Guide Device," *QR (Quarterly Report of RTRI)*, Vol. 50, No. 4, pp. 233-240, November, 2009.

[4] Goto, K., Sogabe, M., Tanabe, M., Watanabe, T. and Tokunaga, M., "Simple Method for Analyzing Contact between Wheelset Members and Track Structures Using MBD," *QR (Quarterly Report of RTRI)*, Vol. 59, No. 1, pp. 55-62, February, 2018.

[5] Miyamoto, M., "Coupler of Railway Vehicle," *The Japan Society of Mechanical Engineers*, Vol. 103, No. 982, pp. 595-597, September, 2000 (in Japanese).

[6] Miyamoto, T., Ishida, H., Sogabe, M., Kawanishi, T. and Murono, Y., "Analysis on Running Safety of Train Quaked by Seismic Motion," *RTRI Report*, Vol. 21, No. 12, pp. 41-46, December, 2007 (in Japanese).

[7] Ansys, Inc., *LS-DYNA R14 Theory Manual*, 2024. https://ftp.lstc.com/anonymous/outgoing/web/ls-dyna_manuals/R14/LS-DYNA_Manual_Theory_R14.pdf

[8] Miyamoto, T., Ishida, H. and Matsuo, M., "Running Safety of Railway Vehicle as Earthquake Occurs," *QR (Quarterly Report of RTRI)*, Vol. 38, No. 3, pp. 117-112, September, 1997.

[9] Hayase, T. and Chonan, S., "Numerical Analysis on Buckling Train Set," *The Japan Society of Mechanical Engineers*, Vol. 66, No. 646, pp. 213-221, June, 2000 (in Japanese).

[10] KYB Corp., Rolling Stock Equipment, p. 7,

[11] Railway Technical Research Institute, ed., *Design Standards for Railway Structures and Commentary (Displacement Limits)*, Maruzen Publishing Co., Ltd., Tokyo, Japan, pp. 67-69, 2006 (in Japanese).

[12] Miyamoto, T., Matsumoto, N., Sogabe, M., Shimomura, T., Nishiyama, Y. and Matsuo, M., "Full-scale Experiment on Dynamics Behavior of Railway Vehicle against Heavy Track Vibration," *Journal of Environment and Engineering*, Vol. 2, No. 2, pp. 419-428, March, 2007.

Authors

Keiichi GOTO, Ph.D.
Senior Researcher, Structural Mechanics Laboratory, Railway Dynamics Division
Research Areas: Dynamic Interaction between Vehicle and Bridge, Vehicle Running Safety during Earthquake, Numerical Simulation

Munemasa TOKUNAGA, Ph.D.
Senior Researcher, Structural Mechanics Laboratory, Railway Dynamics Division
Research Areas: Bridge Dynamics, Vehicle Bridge Interaction, Seismic Design, Structural Health Monitoring

Kohei IIDA, Ph.D.
Senior Chief Researcher, Head of Vehicle Mechanics Laboratory, Railway Dynamics Division
Research Areas: Numerical Simulation of Railway Vehicle, Running Safety during Earthquake, Specification of Vehicle Characteristics

PAPER

Wheel–rail Tangential Contact Force Model for Analyzing Vehicle Dynamics under Running in Rainy Conditions

Daisuke YAMAMOTO
Computational Mechanics Laboratory, Railway Dynamics Division

This paper describes a wheel–rail tangential contact force model for analyzing vehicle dynamics under running in rainy conditions. So far, vehicle dynamics analyses have only been conducted in dry conditions. In this study, we investigate and propose a wheel–rail tangential contact force model for analyzing vehicle dynamics under running in rainy conditions. The proposed model combines Kalker's linear rolling contact theory with the relationship between adhesive coefficient and velocity measured in running experiments. The validity and generality of the proposed model was confirmed by a measurement experiment of tangential contact force using a twin-disc sliding-frictional rolling machine.

Key words: *wheel–rail, relationship between adhesive coefficient and velocity, tangential contact force characteristics, vehicle dynamics analysis under running in rainy conditions*

1. Introduction

Vehicle dynamics analysis based on multibody dynamics theory is an example of Digital transformation (DX) in vehicle development. In recent years, DX in vehicle development is increasingly widespread, and repeated running tests on commercial lines are increasingly being replaced with DX. On the other hand, it is common in conventional analysis for wheel–rail to be studied only in dry conditions. One reason for this is explained next by looking at the process of vehicle dynamics analysis (Fig. 1).

The first step ① in this process is to determine a combination of wheel tread profile and rail cross-sectional shape. Then, assuming that the wheel and rail are a rigid body, contact geometry analysis in which the contact position of the two is determined geometrically is used to compute the wheel rolling radius and contact angle per amount of lateral displacement of the wheel and axle in step ②. In step ③, the contact ellipse between the wheel and rail is computed based on Hertz's contact theory, and the creep coefficient is selected from its aspect ratio by Kalker's linear rolling contact theory. In step ④, the relationship of the wheel–rail tangential contact force coefficient and slip ratio (hereinafter, tangential contact force characteristics) is defined. Finally in step ⑤, the dynamic behavior of a vehicle is calculated by sequential calculation using a vehicle model.

Here, the values in steps ① to ③ can be unambiguously determined when the target vehicle is selected. However, the wheel–rail tangential contact force characteristics in step ④ are closely related to the friction phenomenon still awaiting clarification, and therefore it is difficult to determine realistic characteristics. Specifically, in the case of dry conditions, if the wheel–rail friction coefficient is 0.3, a constant solution that is considered empirically valid can be obtained. However, if water-lubricated conditions are created between the wheel and rail, as would occur under running in rainy conditions, it can be intuitively understood that the friction coefficient will become smaller due to water interposing the wheel and rail, though it is difficult to demonstrate this as a trustworthy numerical value. This is speculated to be one reason why conventional wheel–rail analysis is only studied in dry conditions.

Therefore, if the wheel–rail tangential contact force characteristics under running in rainy conditions is clarified, not only would it be possible to analyze running stability and running safety of a vehicle in realistic more conditions, which include both wet and dry conditions, it would also be possible to quantitatively analyze the running performance of a vehicle during acceleration and deceleration, when wheel–rail tangential contact force characteristics are velocity dependent. Furthermore, diversified vehicle dynamics analysis can be realized with a model that does not require major modification of existing general vehicle dynamics analysis codes developed by engineers and researchers.

In order to diversify the vehicle dynamics analysis, two directions are recognized from an overview of research on wheel–rail tangential contact force characteristics under water-lubricated conditions. One of them is to identify and model the mechanism of wheel–rail tangential contact force characteristics. To this end, useful findings have been obtained through experiments simulating actual phenomena and theoretical studies [1, 2]. However, although these findings have been effectively utilized to analyze wheel–rail tangential contact force characteristics in rainy conditions measured on commercial lines, they have not yet been used to estimate wheel–rail tangential contact force characteristics at arbitrary times and locations.

The other direction is the development of a method effectively adopting tangential contact force characteristics experimentally identified in the analysis of vehicle dynamics with an emphasis on practicality, which is also related to this paper. In past studies [3, 4], a method was proposed using curve fitting to formulate the relationship between the wheel–rail tangential contact force coefficient measured on-board during running tests and the slip ratio for wheel–rail tangential contact force characteristics, and an example of a wheel–rail tangential contact force model based on running tests was presented. However, it has been indicated that because the

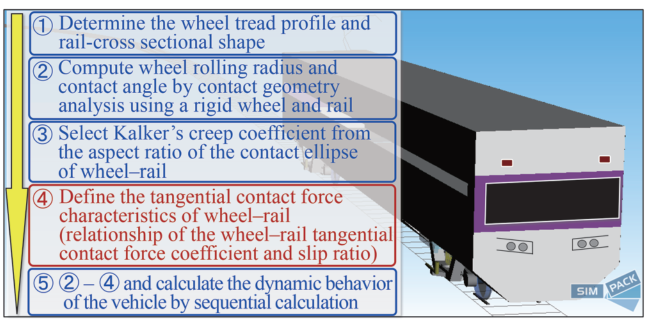

Fig. 1 General process of analyzing vehicle dynamics

wheel–rail tangential contact force characteristics were identified based on data measured on the vehicle, they are not consistent with the principle of Coulomb friction when, for example, the wheel–rail friction is not constant over a measurement section. For this reason, in the case that this method applies directly to the vehicle dynamics analysis over relatively long-distances, there is room for discussion [5]. Thus, realistic wheel–rail tangential contact force characteristics that can be applied to analyzing vehicle dynamics in rainy conditions were not clear.

In this paper, in order to construct a numerical analysis environment in which vehicle dynamics analysis can be performed realistically to reflect running in rainy conditions, a wheel–rail tangential contact force model that can be implemented in general analysis of vehicle dynamics based on multibody dynamics is proposed, focusing upon a "relational expression of adhesive coefficient and velocity" based on the results of running tests on commercial rail lines.

2. Proposal of wheel–rail tangential contact force model

2.1 Construction of wheel–rail tangential contact force model

In our measurement results of tangential contact force using a twin-disc sliding-frictional rolling machine, we confirmed that repeatedly generating slip conditions on a contact surface will result in surface characteristics being activated and tangential contact force demonstrating an increasing tendency; and, regardless of the size of the contact surface between test wheels, the tangential contact force will be a value consistent with Kalker's theoretical formula [6]. This tendency was also found with water-lubricated conditions on the contact surface, although the value of the tangential contact force was small due to the water lubrication.

In this study, based upon the above findings, a Wheel–rail tangential contact force model is constructed based on Kalker's linear rolling contact theory for the case where water is steadily introduced onto a wheel–rail contact surface free of dirt or solid objects.

2.2 Proposed wheel–rail tangential contact force model

Due to space limitations, the details of Kalker's linear rolling contact theory will be explained in this section with an emphasis on the composition of the tangential contact force model, referring to reference literature 7 and 8.

Figure 2 shows a schematic diagram of a wheel and rail in a contact state. Since the cross-sectional shape of the wheel and rail consists of a combination of multiple individual circular arcs, when a vertical load P equivalent to the wheel load is applied to the wheel, the two elastically deform near the contact surface, resulting in a state of surface contact. Here, when the cross-sectional shape of each is as smooth as its design shape, the wheel–rail contact surface assumes an oval shape according to Hertz's theory (this is referred to as a contact ellipse). Then, through the aspect ratio (a/b, b/a) of the contact ellipse, Kalker's non-dimensional creep coefficient, meaning the conversion value of the force in the tangential contact direction, is selected from a parameter table according to Kalker's linear rolling contact theory. Assuming the longitudinal, lateral, and spin non-dimensional creep coefficient to be respectively c_{11}, c_{22} and c_{23}, and the modulus of rigidity to be G, the tangential force in the longitudinal and lateral directions (T_x and T_y) are determined with (1) and (2). Here, due to the physical constraint that the tangential contact force acting on the contact surface between the wheel and rail must not be larger than the frictional force between them, the saturation value of the friction coefficient is determined in advance in numerical analysis, and then the correction coefficient ε shown in (3) is determined and multiplied by (1) and (2) respectively to correct the tangential contact force so that the tangential contact force remains asymptotically stable in relation to the saturation value of the friction force. Notably, (3) is referred to as Levi-Chartet's formula, and in Japan the saturation index β is generally 1.5 in analysis of vehicle dynamics. This value was derived statistically from a tangential contact force measurement experiment [9] conducted using a 1/5 scale model of an actual vehicle.

$$T_x = -ab\left(c_{11}\right)Gs_x \tag{1}$$

$$T_y = -ab\left(c_{22}\right)Gs_y - \left(ab\right)^{3/2}\left(c_{23}\right)G\omega_3 \tag{2}$$

$$\varepsilon = 1/\left\{1+\left(\sqrt{T_x^2+T_y^2}/\mu P\right)^{\beta}\right\}^{1/\beta} \tag{3}$$

where s_x, s_y and ω_3 represent the longitudinal, lateral and spin slip between the wheel and rail, and $ab(c_{11})G$ and $ab(c_{22})G$ respectively refer to the creep coefficient in the longitudinal and lateral directions. In addition, μ is the friction coefficient between the wheel and rail, and P is the wheel load. Then, in order to make Kalker's theoretical formula into a realistic tangential contact force model, this study focuses on the "relational expression of adhesive coefficient and velocity" formulated based on the measured values of running tests, as shown in Fig. 3. The equation shown in Fig. 3 is the adhesive coefficient planning formula for Shinkansen trains, but relational expressions for trains on conventional rail lines, diesel railcars, and locomotives have also been proposed [10], and have been collected together as an example of realistic tangential force characteristics for running in rainy conditions.

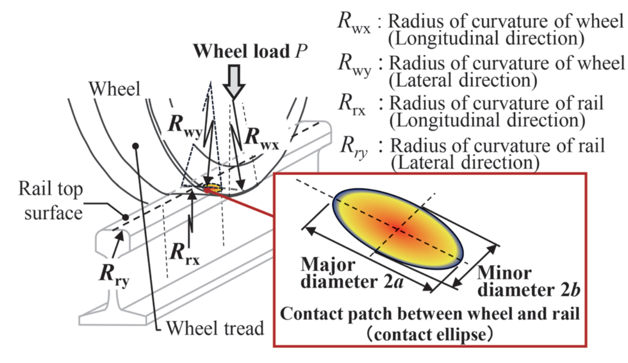

Fig. 2 Wheel and rail contact state

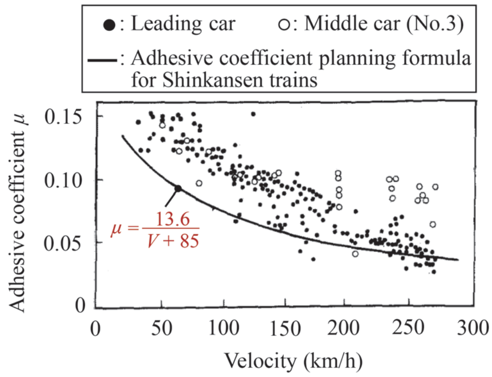

Fig. 3 Results of running experiments and relational expression of adhesive coefficient and velocity [11]

In this study, a wheel–rail tangential contact force model is constructed by substituting this "relational expression of adhesive coefficient and velocity" for μ in (3). This makes it possible to determine even a "relational expression of adhesive coefficient and velocity" for which there is no information on the slip ratio as the "relational expression of wheel–rail tangential contact force coefficient and slip ratio" essential for analyzing vehicle dynamics.

3. Verification of the validity of a wheel–rail tangential contact force model using a twin-disc sliding-frictional rolling machine

3.1 Overview

In order to verify the validity of the wheel–rail tangential contact force model, tangential contact force experiments were conducted simulating contact between wheel and rail by the contact of a pair of large cylindrical test wheels. Experimental results using the same test device showed that the wheel–rail tangential contact force characteristics did not change significantly under 18 ml/min. or higher water flow rate conditions [1]. Therefore, in order to sufficiently reduce variability in the tangential contact force coefficient, the water flow rate was set to 600 ml/min. Then, in order to reduce the uneven distribution of experimental errors caused by wear on the contact surface, a method was adopted in which the load and slip ratio were randomly set in the experimental sequence. This is because the same test wheels were repeatedly used under various experimental conditions.

The validity of this tangential contact force model was verified by the following procedure.

First, the tangential contact force coefficient measured with a slip ratio 0.8% or higher is defined as the friction coefficient. Then, the "relational expression between friction coefficient and circumferential velocity" is identified from these measured values, and then from substitution in (3) and (1), the "relationship between tangential contact force coefficient and slip ratio" is estimated. Finally, validity is verified by comparing the estimated equation with all tangential contact force coefficients not used in constructing the wheel–rail tangential contact force model, including conditions for a slip ratio of less than 0.8%.

Notably, tangential contact force changing in the lateral direction in response to increases and decreases in the tangential contact force in the longitudinal direction can be understood from the principle of the friction circle, and thus in this paper, evaluation is limited to the tangential contact force in the longitudinal direction.

3.2 Experimental device and experimental conditions

Experiments were conducted using "wheel–rail rolling contact equipment" (Fig. 4), which refers to one of the large-scale experimental devices owned by the Railway Technical Research Institute (RTRI). This test device consists of a combination of a 500 mm diameter wheel test wheel (the cross-sectional shape is the modified arc wheel tread profile) and rail test wheel (the cross-sectional shape of rail top surface is the JIS-50kgN rail). In order to simulate a wheel load acting between an actual wheel and rail, the wheel test wheel is pressed against the rail test wheel with a maximum force of 50 kN by a hydraulic actuator. The actual rail has a tie plate with 1/40 gradient laid underneath, so the rail contacts the wheel with an inward tilt towards the center of the track. In this test device, the wheel test wheel is tilted outward by about 1.4 degrees, which is the opposite of the actual arrangement, so that the contact state between wheel and rail is relatively consistent. The contact position between the wheel and rail was determined from conditions in which the wheelset is in neutral position, considering the gauge dimensions of conventional railway lines with no slack.

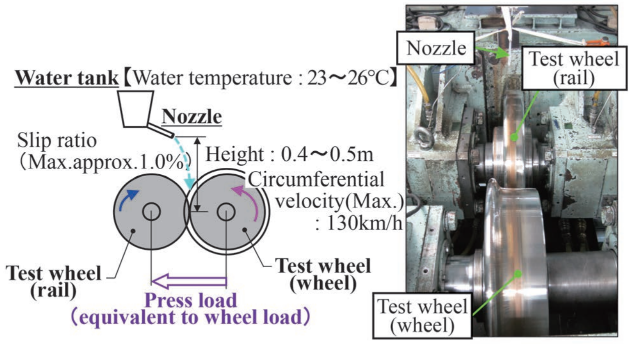

Fig. 4 Experimental device used in validity verification of tangential contact force model

Table 1 Main experimental conditions

Vertical load (kN)		1	5	15
Maximum contact pressure (MPa)		367.9	629	907.2
Size of contact ellipse based on Hertz theory (mm)	Half of major axis	1.75	3	4.22
	Half of minor axis	0.74	1.26	1.82
Circumferential velocity (km/h)		10, 20, 30, 40, 60, 90, 130		
Slip ratio (%)		Approximately 1.0 (Maximum)		
Water flow rate (ml/min.)		Approximately 600		
Water temperature (°C)		23〜26		

In experiments simulating rainy conditions, in order to keep the contact surface between the test wheels wet, water was freely applied onto the contact surface between the test wheels from a simple water tank attached 0.4 to 0.5 m above the contact position of the test wheels. The circumferential velocity of the test wheels was set to a maximum of 130 km/h, simulating that of a conventional rail line, and the slip ratio was limited to a maximum of approximately 1.0% in order to prevent damage to the contact surface of the test wheels. The water flow rate was approximately 600 ml/min, and the water temperature measured during experiments in 23 to 26°C. The main experimental conditions are shown in Table 1.

3.3 Identification of "relational expression of friction coefficient and velocity"

The average value of the tangential contact force coefficient for a consecutive 30 seconds or longer for each experimental condition was summarized as one point, and the "relationship between friction coefficient and circumferential velocity" identified from only for the tangential contact force coefficient under conditions of a slip ratio of 0.8% or more included in all summarized points is shown by x marks in Fig.5. Furthermore, the results (approximate formulas) of identifying the measured values by the least squares method using (4) and (5) described below are shown superimposed on the experimental results with a solid line of the same color.

The following two equations were selected as the reference equations to be used for identifying the "relational expression of friction coefficient and velocity" taking into consideration references [9, 10]. P_0 to P_4 are parameters determined by identification, and

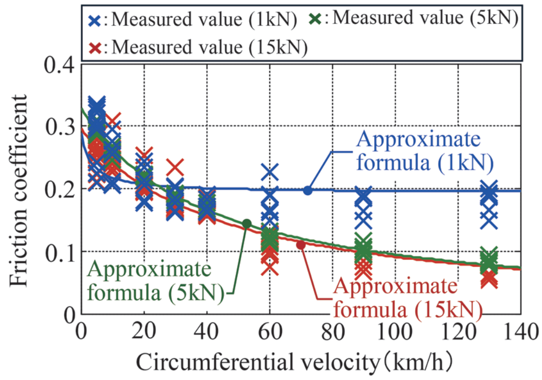

Fig. 5 Relationship of friction coefficient and circumferential velocity measured under conditions of a slip ratio of 0.8% or higher

V is velocity in units of km/h.

$$\mu = P_0\{(1+P_1V)/(1+P_2V)\} \tag{4}$$

$$\mu = P_3/(V+P_4) \tag{5}$$

From the experimental results shown in Fig 5, in the case of a load of 5 kN or more (contact pressure of 629 MPa), which is the same condition as the contact pressure between an actual wheel and rail, as the circumferential velocity of the test wheels increases, the amount of water ingress the contact surface gradually increases due to a mechanism similar to the hydroplaning phenomenon between the rubber tire of an automobile and a road surface, therefore the friction coefficient shows a decreasing tendency. This tendency is consistent with conventional findings. However, under conditions of a small load of 1 kN (contact pressure 367.9 MPa), when the circumferential velocity reaches 40 km/h or faster, a constant friction coefficient is reached of about 0.17, and no velocity dependency is found in the tangential contact force coefficient. Here, although the load is a small 1 kN, the contact pressure is not large enough for the wheel and rail to separate due to water penetrating their contact surface. Therefore, it is thought that water ingress in tiny gaps (volumes) caused by the surface roughness of the contact surface reached its upper limit, resulting in completely water-lubricated conditions, and the tangential contact force coefficient saturated at a constant value. Thus, considering the contact situation under water lubricated conditions, in the case of other load conditions as well, if the circumferential velocity reaches high-speed conditions exceeding 130 km/h, a tendency will be estimated of the friction coefficient saturating at a constant value.

Next, Table 2 shows the parameters identified as “relational expression of friction coefficient and velocity” according to (4) and (5).

As shown in Table 2, due to differences in the characteristics of

Table 2 Parameters of approximation formula for measured values

Vertical load (kN)	Maximum pressure 【measured value】	Identified parameters	Applied standard formula
1	367.9	P_0=0.29 P_1=0.2 P_2=0.3	Formula(4)
5	629	P_3=13.3 P_4=40.5	Formula(5)
15	907.2	P_3=13.1 P_4=44.2	Formula(5)

the equations used for identification, (4) and (5) agree well with expressing the respective characteristics of measured values under conditions of a load of 1 kN and a load of 5 kN or more. Furthermore, variations in measured values under parameter conditions for the approximation formulas for measured values in Table 2 are thought to be due to the contact situation changing because of slight unevenness caused by wear and plastic deformation on the contact surface during repeated experiments.

On the other hand, when the approximation formulas for loads of 5 kN and 15 kN are compared, the difference between the friction coefficients calculated by the two formulas is found to average a small 5.7%. Here, if the experimental results are evaluated and converted to an actual vehicle using the contact pressure as an index, and the combined wheel and rail are respectively the modified arc wheel tread profile wheel and the JIS-50kgN rail, then 5 kN load conditions correspond to a 20 kN wheel load, and 15 kN load conditions correspond to a 100 kN wheel load, and these are found to cover almost all load conditions of a typical railway vehicle.

Thus, it was found that tangential contact force characteristics, when the contact surface is in water-lubricated conditions, have a velocity dependency in which the tangential contact force coefficient becomes smaller as the circumferential velocity of the test wheels increases, if the contact pressure is the same as for a real vehicle. Then, the difference in friction coefficient calculated with the approximation formulas averages a small 5.7% within a range of load conditions simulating a typical railway vehicle. In particular, the latter findings seem useful in simplifying the coding of vehicle dynamics analysis, since no large errors in calculation results are produced even when not rereading the “relational expression of adhesive coefficient and velocity” in response to wheel load fluctuations in analysis of vehicle dynamics under typical running in rainy conditions, except when the wheel load is extremely small and continues steadily.

3.4 Verification of the validity of the wheel–rail tangential model

In other to verify the validity of this tangential contact force model, all measured values, including the tangential contact force coefficient measured under conditions of a small slip ratio of less than 0.8% not used to identify wheel–rail tangential contact force characteristics described in section 3.3, and this estimated tangential contact force model are compared. Figure 6 shows the results of comparing loads of 1 kN, 5 kN and 15 kN under five conditions of circumferential velocity from 10 km/h to 130 km/h. Each plot (x mark) represents the average value of the tangential contact force coefficient for 30 consecutive seconds for each experimental condition. The solid line represents the estimated equation. Both have the same colors, with blue, green, and red representing loads of 1 kN, 5 kN, and 15 kN, respectively.

In the case of a circumferential velocity of 10 km/h in Fig. 6 (a), under wheel–rail water lubricated conditions, the tangential contact force coefficient (x marks) gradually increases as the slip ratio increases from 0% to 0.3%, and when the slip ratio exceeds 0.3% or higher, a tendency will be demonstrated of the tangential contact force coefficient saturating at a constant value of 0.2 to 0.25. This tendency is found to be common under all load conditions. On the other hand, when the circumferential velocity increases, the saturation value of the tangential contact force coefficient gradually decreases under load conditions of 5 kN and 15 kN, but in the case 1 kN load conditions, if the circumferential velocity reaches 60 km/h or faster (Fig. 6 (c) to Fig. 6 (e)), although there will be variations even under slip ratio conditions under 0.8%, it is found that the average value of the tangential force coefficient (x marks) tends to saturate at about 0.17. Thus, a tendency for the tangential contact force coefficient to saturate at a constant value as the slip ratio increases is similarly found in past experiments [2], and thus these tendencies are considered valid.

Next, the relationship between measured values and the estimated equation are evaluated. From Fig. 6, the estimated equation obtained by this tangential contact force model shows a similar form regardless of the circumferential velocity and load conditions, and it is found that the average error of estimated values compared to measured values can be estimated accurately with a maximum of about 22% (Fig. 7). These average errors may be considered inevitable because they are caused by the difference between the approximation formula and measured values in the "relationship between friction coefficient and circumferential velocity" shown in Fig. 5. In other words, these results indicate that improving the accuracy of the approximation formula for measured values with variance is important in analyzing vehicle dynamics under more realistic conditions.

Thus, it was found that the wheel–rail tangential contact force model proposed in this study can estimate the relationship between experimentally measured tangential contact force coefficient and circumferential velocity from small to large ranges of slip ratios with a maximum average error of about 22%. Furthermore, although not included this in this paper due to space limitations, it was confirmed that the estimated and measured values agreed with similar accuracy under other circumferential velocity conditions, and even when experiments were conducted with different water flow rates, similar agreement was confirmed for when the contact surface was constantly under water-lubricated conditions.

From these experimental results, it was found that by understanding the wheel–rail relational expression of the friction coefficient and circumferential velocity, it is possible to estimate accurately the “relationship between the wheel–rail tangential contact force coefficient and slip ratio,” which is essential for analyzing vehicle dynamics, and the validity of this tangential contact force model was verified. Then, it was found that since the wheel–rail friction coefficient agrees with the adhesive coefficient measured in running tests on commercial rail lines, applying a “relational expression of adhesive coefficient and velocity” based on measured values from running tests on this tangential contact force model makes it possible to perform analysis of vehicle dynamics under realistic conditions of running in rainy conditions.

In addition, although it was mentioned above that when using the Levi-Chartet’s formula, it is common to set the saturation index β, which determines the degree of asymptotic approach to the friction force, to 1.5, it was confirmed that even if water-lubricated

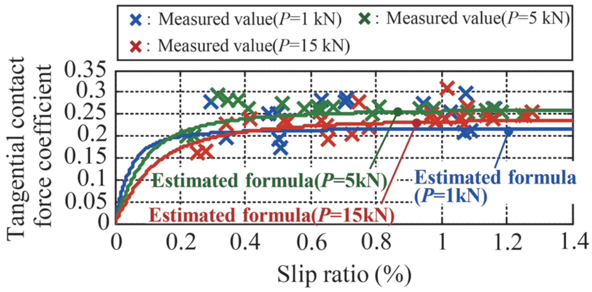

(a) Circumferential velocity 10km/h

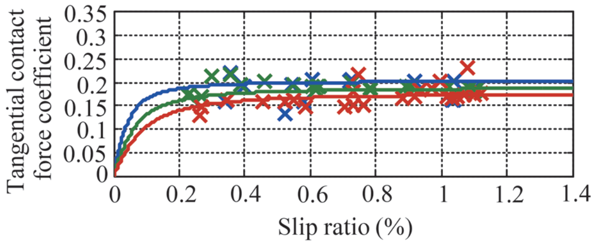

(b) Circumferential velocity 30km/h

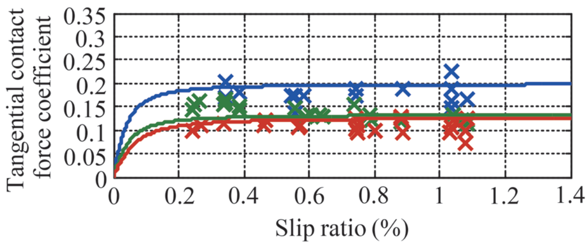

(c) Circumferential velocity 60km/h

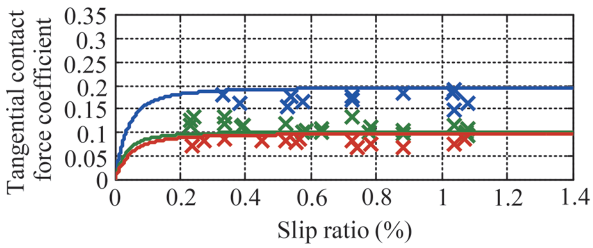

(d) Circumferential velocity 90km/h

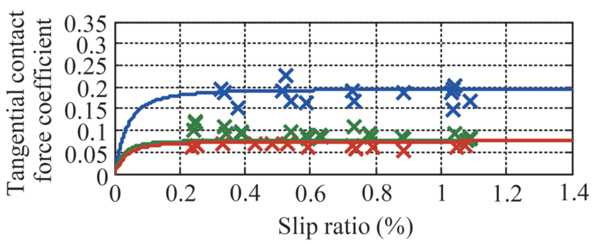

(e) Circumferential velocity 130km/h

Fig. 6 Comparison of tangential contact force model and measured values

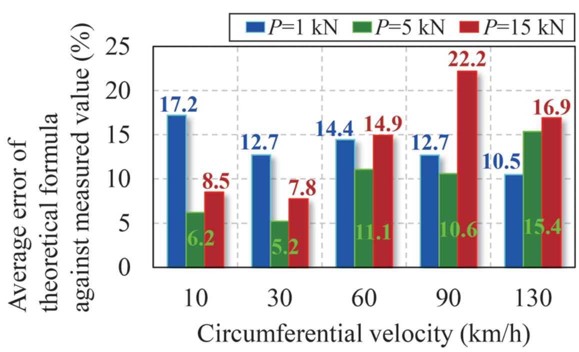

Fig. 7 Average errors in estimated values for measured values

conditions arise between wheel and rail, setting the saturation index β to 1.5 is appropriate.

4. Verification of generality of tangential contact force model

Finally, in order to verify the generality of this tangential contact force model, it is studied in comparison to the results of tangential contact force measurement experiments under water-lubricated conditions conducted by other researchers. Here, based on previous findings [1], experimental results published in major academic journals suggest that attention had been paid to changes in the shape of the contact surface of test wheels being used.

The experimental results in Fig. 8 [12] evaluate the relationship of the tangential contact force coefficient and slip ratio while supplying 3.0×10^{-4} m^3 of water every minute to the contact surface in tangential contact force experiments conducted with a combination of 660 mm and 550 mm diameter test wheels. The contact surface of the test wheels is flat, and one contact surface is "bulging" (convex). Circumferential velocity conditions are studied three ways (100, 150 and 200 km/h) under a maximum contact pressure of 785 MPa. In contrast, it was found that the estimated values obtained with this tangential contact force model assuming the same conditions as in experiments, such as the cross-sectional shape of the test wheels, had a maximum average error of 30.1% compared to measured values, and similar to Fig. 7, generally matched measured values regardless of circumferential velocity conditions. In particular, although the comparison under slip ratio conditions of 0.2% or less was insufficient, it was found that the estimated values and measured values in Fig. 8 are fairly consistent, even in slip ratio ranges of about 0.15% or less. Such results were similarly confirmed for other experimental results described in other literature 8.

Thus, it was confirmed that estimated values according to this tangential contact force model was also consistent with the experimental results conducted by other researchers, and similarly match even when the slip ratio range differs from Fig.6. From the above, it appears that this tangential contact force model has generality as a numerical analysis model for estimating tangential contact force characteristics when there are constant water-lubricated conditions between a wheel and rail.

5. Conclusions

In order to construct a numerical analysis environment capable of performing realistic vehicle dynamics analysis simulating running in rainy conditions, a Wheel–rail tangential contact force model (friction characteristics model) was proposed. Then, based on the results of comparing it to experimental results under various conditions, we could obtain the main conclusions below.

(1) By combining the "relational expression of adhesive coefficient and velocity" during rainy conditions identified in running tests on commercial rail lines with Kalker's linear rolling contact theory, a method was proposed for estimating the relationship between the tangential contact force coefficient and slip ratio between a wheel and rail simulating running in rainy conditions.

(2) "The relational expression of adhesive coefficient and velocity" under rainy conditions was experimentally clarified to be almost the same within the range of wheel load conditions for an actual vehicle. This was found to be useful for simplifying the coding of vehicle dynamics analysis.

(3) In order to verify the validity of this tangential contact force model, tangential contact force measurement experiments were conducted using a twin-disc sliding-frictional rolling machine. Based on the results, it was confirmed that the Levi-Chartet's formula with saturation index β of 1.5 is valid even under water-lubricated conditions, and it was shown that the estimated values according to this tangential contact force model can be estimated with a maximum average error of about 30% compared to measured values in the experiments used in this study.

Finally, this wheel–rail tangential contact force model can be utilized to analyze vehicle dynamics under constant water-lubricated conditions, except for when water droplets are scattered between a wheel and rail, such as when it starts or stops raining. Specifically, it would be possible to evaluate the running stability and running safety of a vehicle not only under running in rainy conditions, but also quantitatively evaluate running performance when a vehicle is accelerating and decelerating in situations where wheel–rail tangential contact force characteristics have velocity dependence. In particular, it is believed that it will be useful as it can be utilized to diversify the analysis of vehicle dynamics without having to make large-scale improvements to existing vehicle dynamics analysis codes developed by general engineers and researchers.

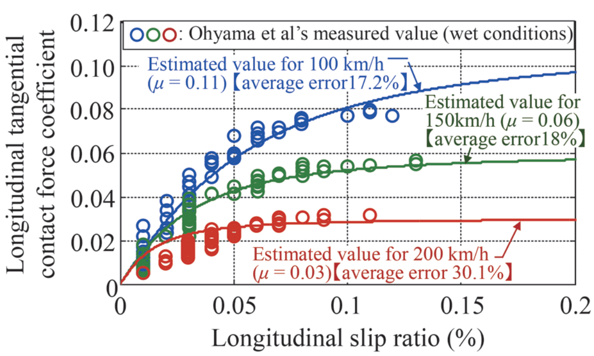

Fig. 8 Comparison of measured values in reference literature 12 and this tangential contact force model

References

[1] Yamamoto, D., Influence of Wheel Turning Trace on Wheel/Rail Tangential Contact Force Characteristics under Running in Rainy Conditions, *RTRI Report*, Vol. 36, No. 7, pp. 27-34, 2022 (in Japanese).

[2] Yamamoto, D., Evaluation of Relationship between Water Flow Rate and Tangential Contact Force of Wheel/Rail Using Twin-disc Rolling Machine, *RTRI Report*, Vol. 37, No. 4, pp. 1-7, 2023 (in Japanese).

[3] Polach, O., Creep forces in simulations of traction vehicles running on adhesion limit, *Wear*, 258, pp. 992-1000, 2005.

[4] Vollebregt, E. A. H., Numerical modeling of measured railway creep versus creep-force curves with CONTACT, *Wear*, 314, pp. 87-95, 2014.

[5] Yamamoto, D., Difference between running tests and laboratory experiments using twin-disc rolling machine regarding to wheel/rail tangential contact force characteristics, *Transactions of the JSME*, Vol. 90, No. 936, 2024 (in Japanese).

[6] Yamamoto, D., Estimation of Tangential Contact Force between Actual Wheel and Rail Using Twin-disc Rolling Machine, *RTRI Report*, Vol. 35, No. 9, pp. 29-34, 2021 (in Japanese).
[7] Kalker, J. J., *Three-dimensional elastic bodies in rolling contact*, KLUWER ACADEMIC PUBLISHERS, 1990.
[8] Yamamoto, D., A practical wheel / rail tangential contact force model combining the Levi-Chartet's formula and the relationship between adhesive coefficient and velocity for analyzing vehicle dynamics, *Transactions of the JSME*, Vol. 89, No. 922, 2023 (in Japanese).
[9] Matsudaira, T., On the method of preventing the hunting of railway vehicles, particularly of two-axle cars, *ORE Question C9*, C9/RP.2E, Utrecht, pp. 99-171, 1960.
[10] Electric Railway Handbook Editorial Committee, Electric Railway Handbook, Corona Publishing Co., Ltd., p. 389, 2007 (in Japanese).
[11] Watanabe, T., Domestic and international history and recent trends of research into idling and slip detection and re-adhesion control, *The journal of the Institute of Electrical Engineers of Japan*, Vol. 122, No. 9, pp. 613-617, 2002 (in Japanese).
[12] Ohyama, T., Maruyama, H., Slip and friction under high speed rolling contact (Effect of surface roughness under water lubricated conditions.), *Transactions of the JSME*, *Series C*, Vol. 48, No. 431, pp. 1005-1013, 1982 (in Japanese).

Author

Daisuke YAMAMOTO, Dr.Eng.
Senior Researcher, Computational Mechanics Laboratory, Railway Dynamics Division
Research Areas: Vehicle Dynamics, Contact Mechanics, Wheel–rail

Study on the Occurrence Conditions of Squeal Noise and High-frequency Noise in Railway Curved Sections

Takeshi SUEKI **Yasuhiro SHIMIZU**
Noise Analysis Laboratory, Environmental Engineering Division
Takuma NITTA **Kentarou TAKAI**
West Japan Railway Company

Squealing (below 10 kHz) and high-frequency noise (above 10 kHz) can occur when trains pass through curved sections of track. Measurements of these noises were carried out on commercial lines to understand how they are generated. It was found that these noises vary from wheel to wheel, having large dispersion. The analysis results showed that these noises are prominent when the outer wheel flanges are in contact with the outer rail at certain passing speeds. On the other hand, these noises are reduced when a train is running at equilibrium speed in curves.

Key words: *railway noise, curved section, squeal noise, high-frequency noise, flange contact*

1. Introduction

When trains run on a curved track, both wheels and rail often radiate noise with higher frequency than rolling noise which has frequency components of around 500-2,000 Hz at 160 km/h [1], for example. Noise generated in curved sections has tonal components, whereas rolling noise in straight sections usually has broadband components. The noise with higher frequencies in curved sections is generally called "squeal noise." In some cases, the noise with much higher frequency, above 10 kHz, is also observed at curved sections.

Squealing and high-frequency noises greatly contribute to overall wayside noise and may cause complaints from residents. A lot of research and studies have been carried out on noise in curved sections [2, 3, 4, 5]. However, the conditions under which this noise occurs are not fully understood.

There are two main railway systems in Japan. One is meter-gauged railways and the other is Shinkansen. Meter-gauged railways, sometimes called "conventional railways," have relatively small curve radii, level crossings, etc. Trains on meter-gauged railways in Japan run at 130 km/h or less, except for a few railways. Shinkansen is a high-speed railway system that has some designated features such as specialized rolling stock, large curve radii, no level crossings, and uses standard gauge, etc. Shinkansen trains generally run at 200 km/h or more. Squeal noise and high-frequency noise occur on both meter-gauged railways and Shinkansen lines.

In this report, squeal noise and the high-frequency noise were measured and their characteristics were investigated in commercial meter-gauged and Shinkansen lines. The conditions under which they occur were analyzed.

2. Categorization of noises in curved section

Squealing and high-frequency noises that occur exclusively in curves are generated by complex contact between the wheels and rails. In this study, these noises are categorized based on dominant frequencies as follows:

- Squeal noise (2-10 kHz) [2, 6]: Noise which is mainly generated when a train runs through sharp curves and is caused by relative slippage between wheel treads and rails. The main frequencies are from 2 kHz to 10 kHz. This type of noise is particularly noticeable on inner wheels and rails.
- High-frequency noise (above 10 kHz) [7]: This noise is mainly generated when a train runs through relatively gentle curves and is caused by contact between the wheel flange and the railhead. The main frequencies are above 10 kHz. This noise tends to be particularly salient on outer wheels and rails.

Although tendencies and frequencies of occurrence differ between meter-gauged and Shinkansen lines, squealing and high-frequency noises occur on both types of railway system as discussed in Chapters 3 and 4. It should be noted that the forms of occurrence cannot be strictly classified and may be mixed.

3. Squealing and high-frequency noise on meter-gauged railways

3.1 Outline of measurement set up on meter-gauged railway line

Figure 1 shows the outline of measurement points on a section of meter-gauged railway line. The section used for measurement is a curved section with a 404 m curve radius, superelevation of 98 mm, and no gauge widening. The track consists of ballasted track, Japanese 50-kg N type rail, concrete sleepers, and rail pad with 110 MN/m stiffness. The equilibrium speed in this curve is 68.7 km/h.

Two microphones were installed close to the track and on both the inner and outer rail sides to be roughly symmetrical across the track. The height of microphones was set roughly equal to wheel axle level at 450 mm height from the rail head on the outer rail side and -130 mm on the inner rail side. The position of the wheels relative to the rails in the transverse direction were also measured.

The trains used for the measurements were four types of commuter trains, consisting of four, six, seven, and eight cars. Measurements were made in a section located approximately 100 m from the station. Some trains accelerated through the section after having stopped at the station. Other trains passed through the section at a constant speed because they did not stop at the station. Trains which accelerated through the section are referred to as "local trains," while those which ran through it at a constant speed are referred to as "rapid trains." Local trains passed through the section below the equilibrium speed, while rapid trains travelled above the equilibrium speed.

All data was collected when weather conditions were either

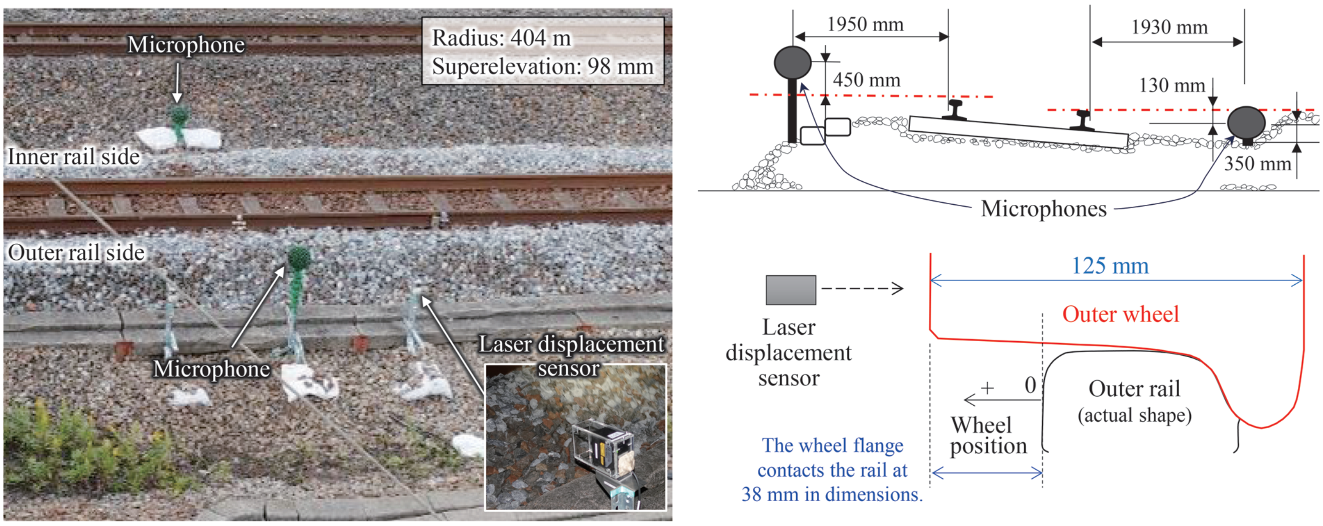

Fig. 1 Measurements in the meter-gauged railway line

sunny or clouded, which means that the rail surface was dry.

3.2 Representative results of noise measurements

Figures 2 and 3 show the spectrograms of noise for a local train and a rapid train passing through the section, respectively. The black lines in the lower part of the figures indicate the range over which train passes through the measurement section. It should be noted that in these results, 0 dB is set to averaged overall value of the measured noise, obtained by the microphone close to the outer rail, for all results when the wheels of all trains pass through the section.

3.2.1 Local train measurement results

Figure 2 shows the noise spectrogram for passage of a local train. This train was one of four types described in the section 3.1 and consisted of eight cars. The leading car of the train passed at 40 km/h and the trailing car at 60 km/h. The average speed was 51 km/h. All the cars of the local train passed through this section below the equilibrium speed.

As shown in Figs. 2 (a) and (b), the sound pressure levels (SPL) below 1 kHz were higher when trains passed through. They correspond to rolling noise. The levels were also higher at around 6-9 kHz at around 5 and 8 seconds, and those at around 19 kHz at around 9-13 seconds.

The lower frequencies were considered to be squealing noise, and the higher ones considered to be high-frequency noise. The number of seconds correspond to wheel passage. The component around 19 kHz was modulated with respect to time due to the Doppler effect.

Comparing the results for the inner and outer rail sides, the tendency appears to be that larger squealing noise is observed on the inner rail side, and the greater high-frequency noise on the outer rail side. However, the noise levels on the outer rail side in the frequency range of 5-15 kHz were greater than those on the inner rail side at 10-13 seconds, indicating that there were slight variations to levels in squeal and high-frequency noise tendencies depending on time.

As shown in Fig. 2, the level of high-frequency noise around 16 kHz remains at a high level from around 13 seconds to after the train has passed, albeit at a lower level that when the train was actually passing. It is thought that this may be a result of the rail becoming a source of and radiating sound.

3.2.2 Rapid train measurement results

Figure 3 shows the noise spectrogram for passage of a rapid train. This train consisted of eight cars, with a train speed of 76 km/h. The train type was the same as the local train descried in Section 3.2.1. Train speed was a constant since it did not stop but ran straight through the station. All cars passed through this section at a constant speed, which is above the equilibrium speed.

As shown in Fig. 3, the levels corresponding to rolling noise (below 1 kHz) of the rapid train were higher than those of the local train due to differences in speed. Squeal noise occurred at around 6 seconds (above 4 kHz) and 8 seconds (around 8 kHz).

The high-frequency noise, approximately 18 kHz, became particularly noticeable at 6 seconds, corresponding to the wheel passage considered to be the noise source. The frequency of high-frequency noise was modulated with respect to time due to the Doppler effect. Although the noise level fell after the wheel passage, a relatively high noise level continued as the train passed. This was due to the noise from the rail. The magnitudes of noise below 13 kHz, which occurred at around 6 seconds, were greater on the inner rail side than on the outer rail side.

3.3 Occurrence situations in the meter-gauged railway

The results described in the previous section indicate the occurrence of squeal noise and high-frequency noises was not uniform, even for the same train. This tendency was seen in other trains, not reported in this paper. Therefore, averaging alone is not suitable for explaining the phenomena.

This section therefore investigates conditions where squeal and high-frequency noise occur using a histogram to verify data distribution. To this end, the top 10% of data which seemed to express these noise were used.

Figure 4 shows two-dimensional histograms of the frequency spectrum of the noise when each wheel passes in front of the microphones. These histograms were derived from 140 trains, i.e. 3,332 wheel sets.

The level value distributions were almost constant and the most

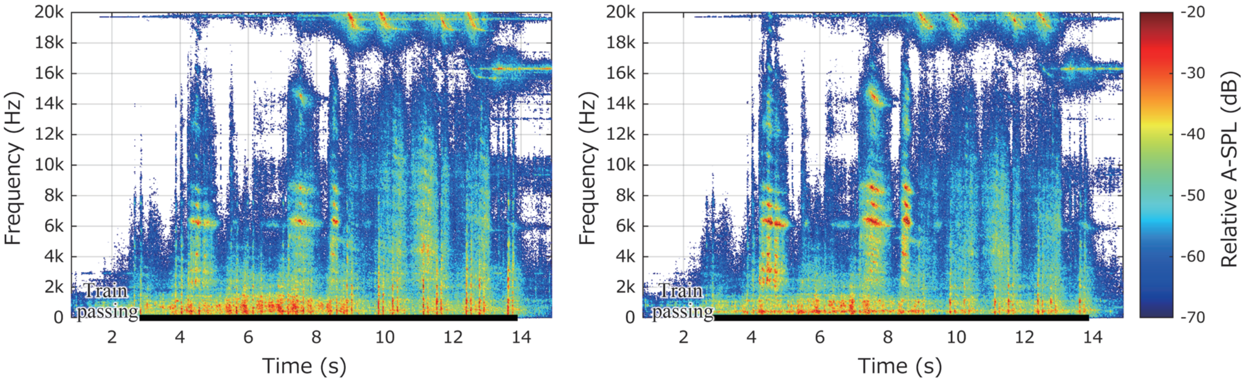

(a) Outer rail side (b) Inner rail side

Fig. 2 Noise spectrogram (local train, 8 cars, 40-60 km/h)

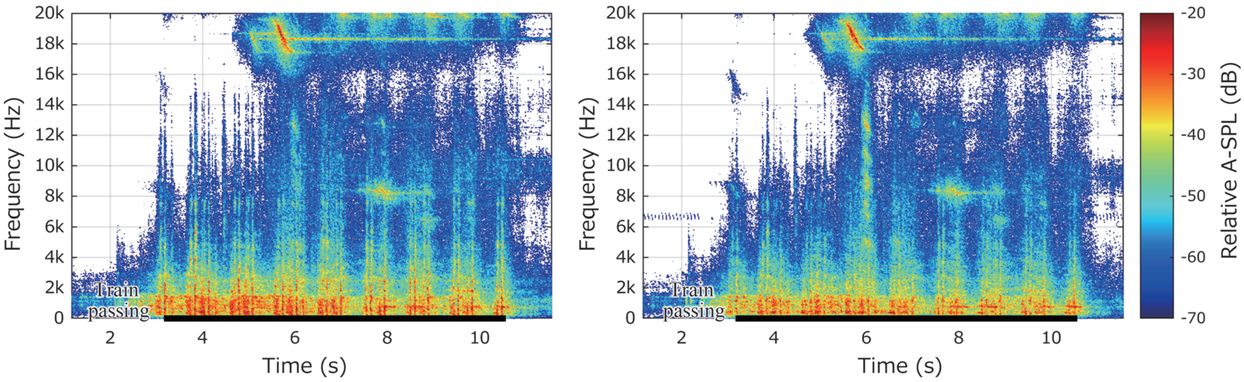

(a) Outer rail side (b) Inner rail side

Fig. 3 Noise spectrogram (rapid train, 8 cars, 76 km/h)

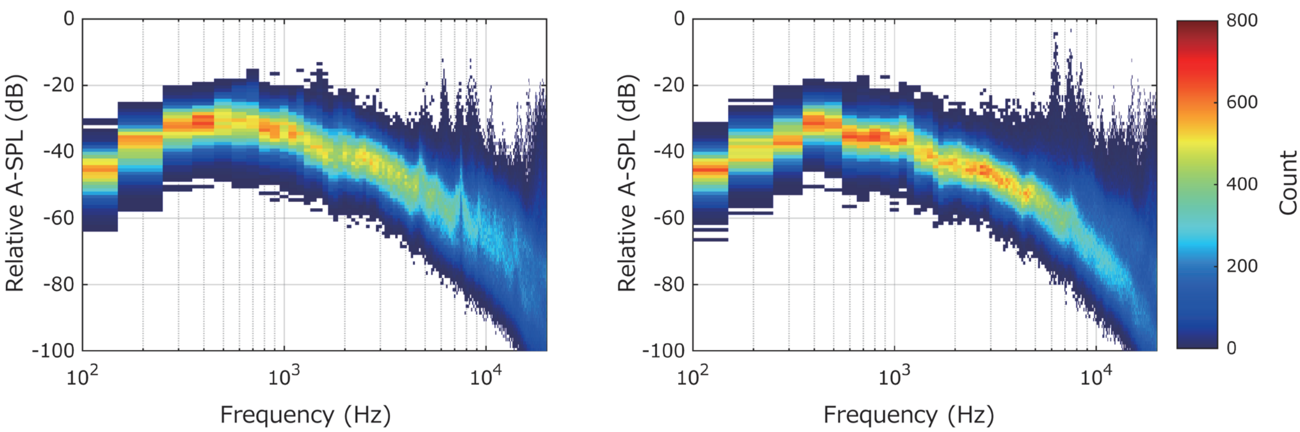

(a) Outer rail side (b) Inner rail side

Fig. 4 Two-dimensional histograms of the frequency spectrum of the noise (30-90 km/h)

counted values were in the middle of the distributions at frequencies below 4 kHz in Fig. 4. In contrast, the distributions above 4 kHz were wider, the most counted values were in the lower part of the distributions, and the values were also small. The distributions were especially wide at 6-7 kHz and 14-20 kHz, indicating that squeal noise or high-frequency noise occurred only on some wheels and varied greatly in magnitude from wheel to wheel.

Figure 5 shows the magnitude of the 6-7 kHz (representing squeal noise) and 14-20 kHz (representing high-frequency noise) components on the front wheel of each bogie. These figures were derived from the top 10% of data. The blank areas had no data. The horizontal axis shows wheel passing speed, and the vertical axis the lateral position of wheel measured by laser displacement sensor (see Fig. 1). The positions where the outer wheel flange contacts the outer rail are shown in Fig. 5 as the red lines. The outer wheel flange contacts the rail when wheel position exceeds 38 mm.

Figures 5 (a) and (c) indicate that squeal noise at 6-7 kHz is particularly noticeable when the train is running slightly below the

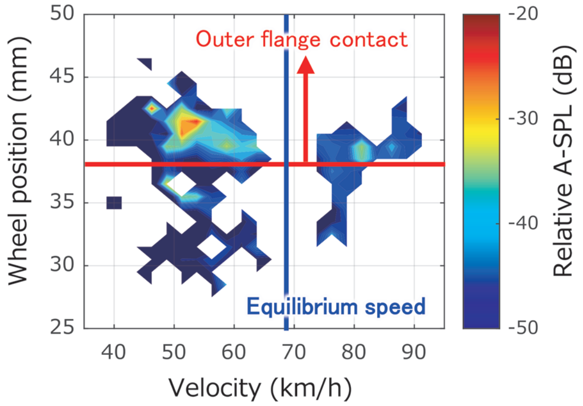

(a) Outer rail side, 6-7 kHz

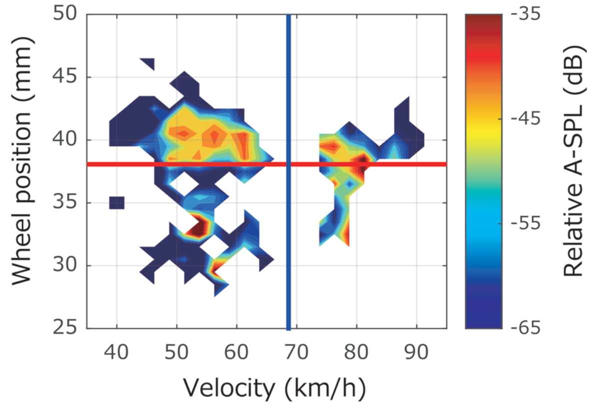

(b) Outer rail side, 14-20 kHz

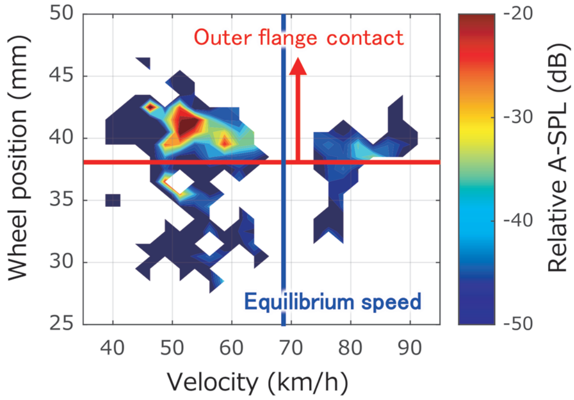

(c) Inner rail side, 6-7 kHz

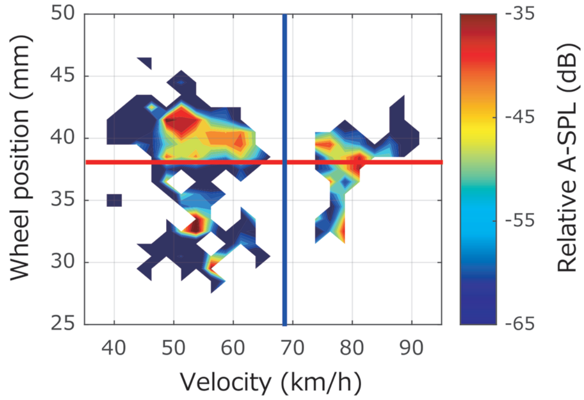

(d) Inner rail side, 14-20 kHz

Fig. 5 Magnitudes of noise with respect to wheel positions and velocity on the front wheel of each bogie

equilibrium speed, around 52 km/h, and when the outer wheel flange is in contact with the outer rail. Sound pressure level on the inner rail side is greater than that on outer rail side, indicating that the outer wheel coming into contact with the outer rail affects the noise that occurs on both the inner and outer rail sides. However, on condition that velocities are anywhere except around 52 km/h slightly below the equilibrium speed then even with outer rail/wheel flange contact, the 6-7 kHz component is small. When there is no contact between the outer wheel and the outer rail, the 6-7 kHz component is also small whatever the speed.

Figures 5 (b) and (d) show that in the high-frequency noise component, the sound pressure level is high when the outer wheel flange is in contact and the outer rail at speeds below and above the equilibrium speed. However, at speeds closer to the equilibrium speed, the sound pressure in the high-frequency noise range is slightly lower. The generation of high-frequency noise even when the equilibrium speed is exceeded, is a point which differs from what happens with squeal noise.

4. Squeal noise and high-frequency noise on Shinkansen lines

4.1 Outline of measurement set up on Shinkansen line

Figure 6 shows the set up for taking measurements on a Shinkansen line. The chosen section is a curved section on a viaduct with a curve radius of 3,500 m, 180 mm superelevation, and no gauge widening. The track consists of slab track, Japanese 60-kg type rail, and rail pads with 60 MN/m stiffness. The equilibrium speed in this curve is 236 km/h.

Two microphones, one on the inner rail side and one on the outer rail side, were installed close to the rail. The height of microphones was 180 mm below rail head level for the outer rail side and 455 mm above rail head level for the inner rail side. Although the positions of the microphones should have been installed in the same configuration as on the meter-gauged railway line as described in Fig. 1, it was impossible to put them symmetrically. The position of the wheels relative to the rails in the transverse direction were also measured.

Five types of Shinkansen train were used for making measurements. Three consisted of sets with eight cars and two with sixteen cars. Trains passed through this section at different speeds. In this test, trains passing through the section at speeds faster than the equilibrium speed are called “high-speed trains” (approximately 240-260 km/h), and those running below this speed are referred to as “low-speed trains” (approximately 150-230 km/h).

All measurements were taken in sunny or clouded weather conditions, so the rail surface was dry.

4.2 Representative results of noise measurements

Figures 7 and 8 show the spectrograms of noise for one low-speed train and one high-speed train, respectively. The black lines at the bottom of the figures indicate the range during which trains passed through the measurement section. In these results, 0 dB corresponds to the averaged overall values of measured noise, obtained

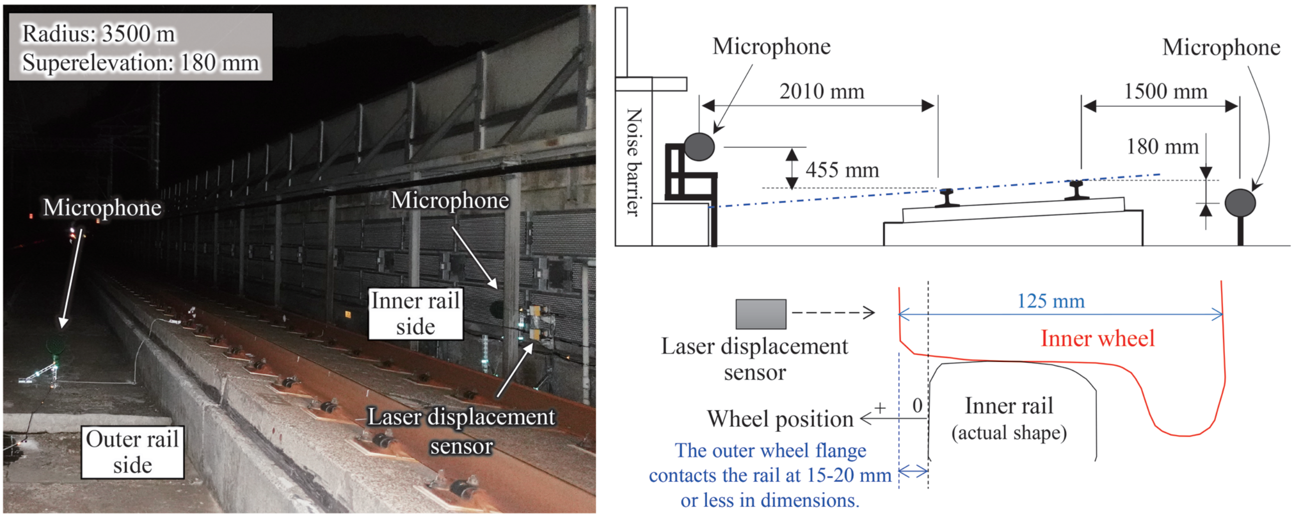

Fig. 6 Measurements in Shinkansen line

by the microphone close to the outer rail, for all results when the wheels of all trains pass the section.

4.2.1 Low-speed train measurement results

Figure 7 shows the spectrogram of the low-speed train. This train consisted of eight cars, and was running at a speed of 195 km/h.

As shown in Fig. 7, the noise levels below 4 kHz, especially around 2 kHz, were higher while trains passed by. The noise levels mainly corresponded to rolling noise caused by marks left on the rail after grinding. Their wavelength was approximately 30 mm and equivalent to 1.8 kHz at 195 km/h. Squeal noise occurred at frequencies of approximately 2 kHz, 5 kHz, and 10 kHz at around 4 s. At this time, the levels at these frequencies contained both rolling and squeal noises.

High-frequency noise occurred at frequencies of 12-17 kHz with passing trains. This means that it was generated around almost all wheels. The frequency of high-frequency noise was modulated with respect to time due to the Doppler effect. The levels of these frequencies remained high before and after trains passed by. They were also radiated from the rails, similar to the measurement at the meter-gauged railway described in the previous section.

The level difference of noise between inner and outer rail sides were not compared directly because these microphones were not installed symmetrically. A previous study [7] reported that high-frequency noise is predominant on the outer side of the rail, so there is a high possibility that the noise on the outer rail side is also greater than that of the inner rail side of the rail in this section.

4.2.2 High-speed train measurement results

Figure 8 shows the spectrogram for a high-speed train. The train consists of 16 cars, with a speed of 255 km/h.

As shown in Fig. 8, the levels below 4 kHz, especially around 2.5 kHz, were also greater when trains passed by. These correspond to rolling noise. The frequency due to the mark generated by rail grinding was 2.4 kHz at 255 km/h. High-frequency noise occurred only on some wheels at a frequency of approximately 14 kHz, unlike the low-speed trains. The components at these frequencies were modulated with respect to time due to the Doppler effect. Squeal noises were not observed in this train.

4.3 Occurrence situations in the Shinkansen line

Even on the Shinkansen, the occurrence of squealing and high-frequency noises were not uniform, even within the same train. This tendency was seen in other trains, not shown in this paper. Therefore, averaging alone was not suitable for explaining the phenomena.

In this section, as well as in the section 3.3, the occurrence conditions of squeal and high-frequency noises were investigated using a histogram to verify data distribution. Then, the top 10% of data which seemed to express these noise were used.

Figure 9 shows two-dimensional histograms of the frequency spectrum of the noise when each wheel passes in front of the microphones. Note that they were derived from 119 trains i.e. 5,435 wheel sets.

There tended to be small level variation at all frequencies because the most counted values were in the middle of the distribution and their values were high at the middle, except around 2 kHz, 4.5 kHz, and above 10 kHz. This indicated that the variation between trains was small in these frequency ranges except around 2 kHz, 4.5 kHz, and above 10 kHz. The frequency of around 2 kHz corresponded to rolling noise due to the marks of rail grinding, which varied respect to train velocity, leading to less count of the level. The frequency of around 4.5 kHz was affected by squeal noise, also leading to less count of the level. Those above 10 kHz corresponded to high-frequency noise. The distribution above 10 kHz were wide and most counted values at these frequencies were not high. This was due to that the occurrence of the high-frequency noise was varied.

Figure 10 shows the magnitudes of component of 8-10 kHz (representing squeal noise) and 10-20 kHz (representing high-frequency noise) on the front wheel of each bogie. These figures were derived from the top 10% of data. The blank areas had no data. The horizontal axis means the wheel passing speed, and the vertical axis means the lateral position of wheel, which was measured by the laser displacement sensor (see Fig. 6).

Here, the laser displacement sensor was installed on the inner rail side, unlike in Chapter 3. This meant the contact relationship was reversed. The positions where the outer wheel flange was in contact with the outer rail are shown in Fig. 10 as red lines. The

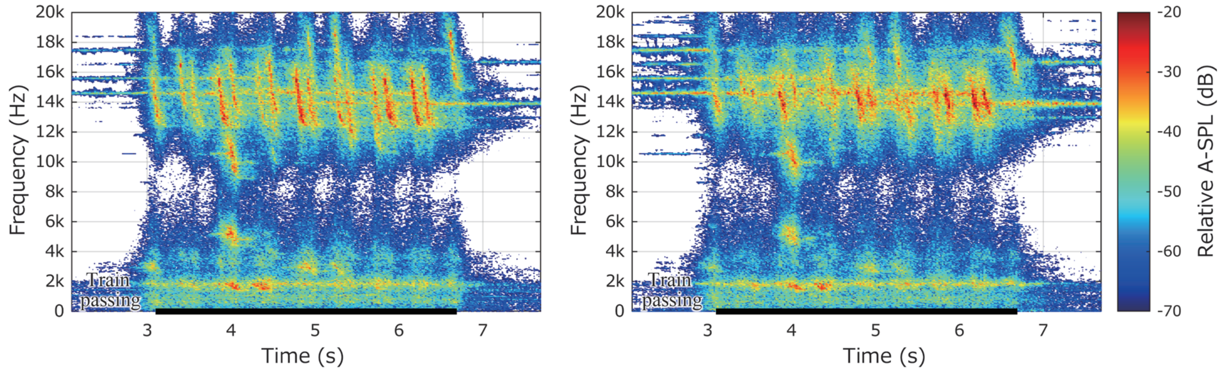

(a) Outer rail side (b) Inner rail side

Fig. 7 Noise spectrogram (low-speed train, 8 cars, 195 km/h)

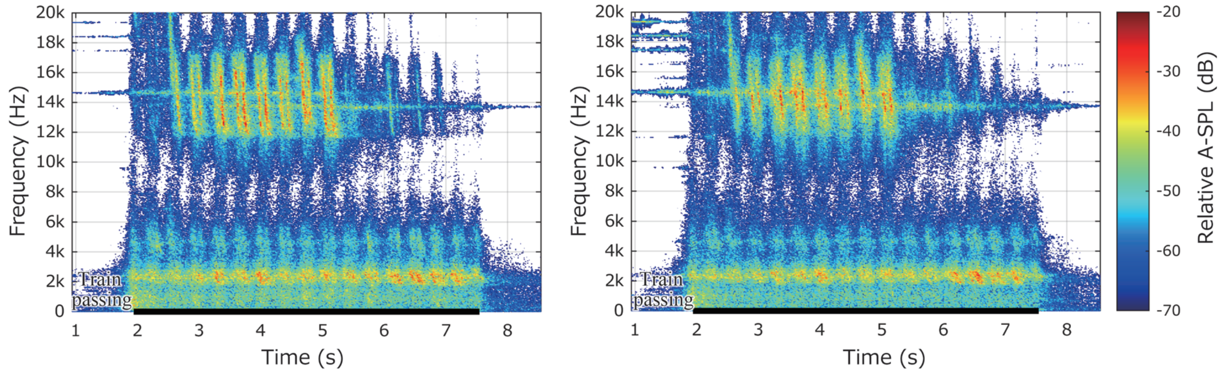

(a) Outer rail side (b) Inner rail side

Fig. 8 Noise spectrogram (high-speed train, 16 cars, 255 km/h)

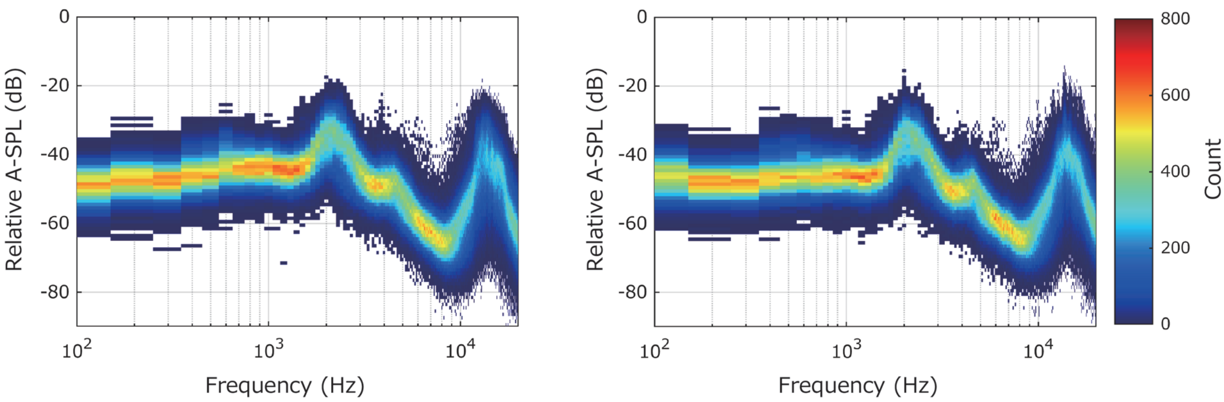

(a) Outer rail side (b) Inner rail side

Fig. 9 Two-dimensional histograms of the frequency spectrum of the noise (154-256 km/h)

outer wheel flange is in contact with the rail when wheel position is below 15-20 mm. It was noted that almost all front wheel flanges are in contact with the rail below equilibrium speed. However, some flanges of front wheels are not in contact with the rail above the equilibrium speed.

Figures 10 (a) and (c) show that noises in the frequency range of 8-10 kHz are also particularly noticeable on each side when the outer wheel flange is assumed to have come into contact with the outer rail and the passing speed was around 195 km/h, which is below the equilibrium speed. Noises in the frequency range of 8-10 kHz fell from 220 km/h to the equilibrium speed. Whereas these noises increased again above the equilibrium speed, their level remained below those of around 195 km/h. When the outer wheel flange was assumed not to have come into contact with the outer rail, the noises in the frequency range of 8-10 kHz were quieter.

Figures 10 (b) and (d) show that the level of noises in the frequency range of 10-20 kHz are great on each side when the outer wheel flange is assumed to have contacted the outer rail and passing speed was below the equilibrium speed. The noise in the frequency range of 10-20 kHz above the equilibrium speed was slightly small-

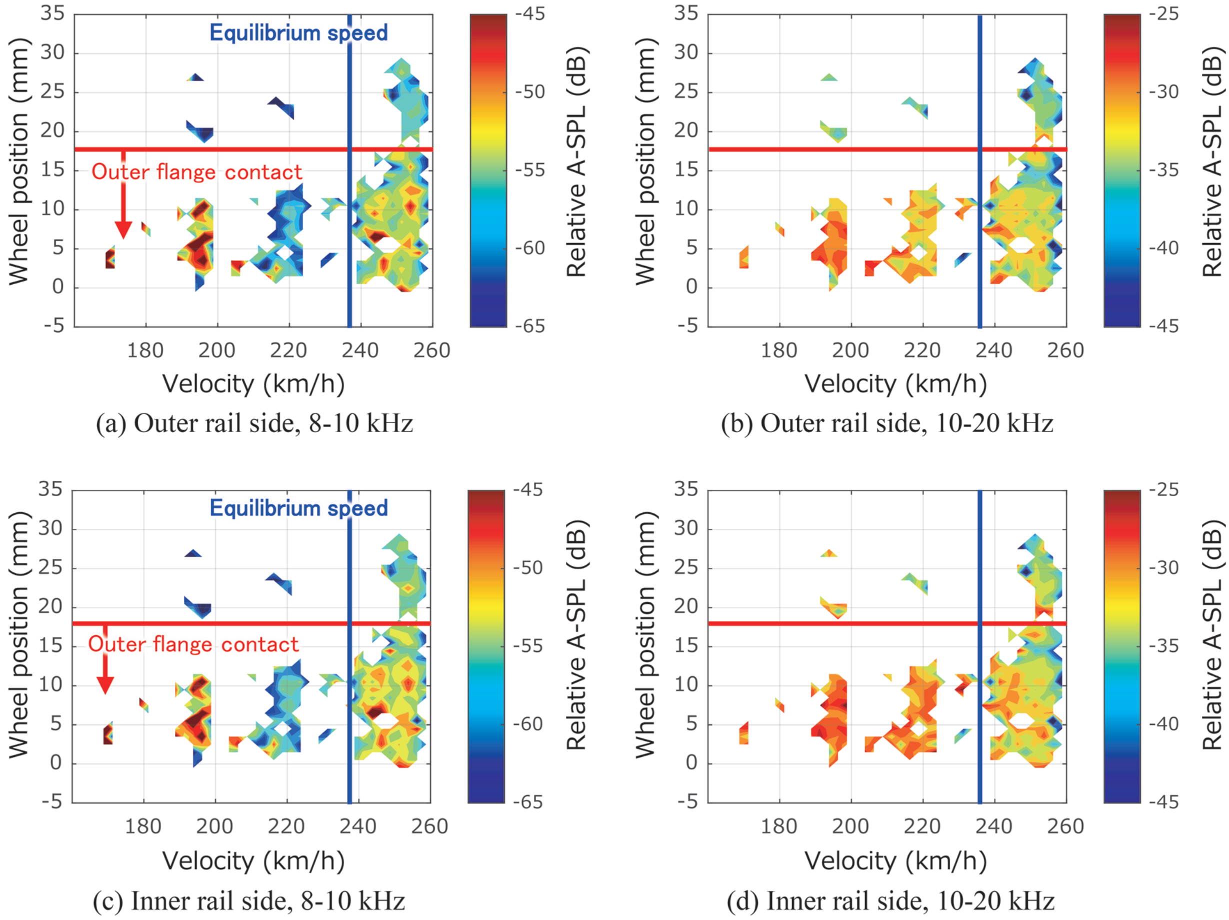

Fig. 10 The magnitudes of noise respect to wheel positions and velocity on the front wheel of each bogie

er than that below the equilibrium speed. When the outer wheel flange was assumed not to have contacted the outer rail, the noises in the frequency range of 10-20 kHz tended to be quiet. As shown in Figs. 7 and 8, high-frequency noise above 10 kHz was observed in almost all bogies of low-speed trains, whereas that noise was only observed in the part of bogies of high-speed trains. This could be due to that some wheel flanges did not contact the rail when the train speed exceeded the equilibrium speed.

5. Conditions related to occurrence of squealing and high-frequency noise in curves

Based on the results described in Chapters 3 and 4, it can be assumed that the conditions in which squealing and high-frequency noise occur in curves have following tendency, regardless of whether they are meter-gauged railways or Shinkansen.

- Squealing occurs easily when two conditions are met: trains are running at speeds slightly below the equilibrium speed and the outer wheel flanges are in contact with the outer rail. Squealing is observed both on inner and outer rail sides of curves. When comparing both, the noise on the inner rail side rail is predominant.
- The train speed at which squealing occurs easily, was around 52 km/h in the meter-gauged railway and 195 km/h on Shinkansen, respectively. These speeds correspond to -0.39 m/s^2 of the excess centrifugal acceleration in both the meter-gauged railway and Shinkansen.
- High-frequency noise is observed at both inner and outer rail sides of curves when outer wheel flanges are in contact with outer rail.
- The magnitudes of these noises tend to decrease when trains are running close to the equilibrium speed or when the outer wheel flanges are not in contact with the outer rail. These characteristics are common in both meter-gauged trains and Shinkansen trains.

6. Conclusions

We investigated squealing and high-frequency noise generated when trains pass through curved sections for meter-gauged trains and Shinkansen trains, respectively. Results gave insights about the conditions in which these noises are generated.

The conditions described in this report are based on estimations made from measurement results at two locations. It is necessary to obtain more samples to verify whether similar results can be obtained for all curves. It is also necessary to reveal mechanisms on these occurrence conditions. We plan to research these issues in the future.

References

[1] Thompson, D. J., *Railway noise and vibration: Mechanisms, modeling and means of control*, Elsevier Ltd., 2009.

[2] Monk-Steel, A. D., et al., “An investigation into the influence of longitudinal creepage on railway squeal noise due to lateral creepage,” *Journal of Sound and Vibration*, Vol. 293, pp. 766-

776, 2006.
[3] De Beer, F. G., et al., "Squeal noise of rail-bound vehicles influenced by lateral contact position," *Journal of Sound and Vibration*, Vol. 267, pp. 497-507, 2003.
[4] Remington, P. J., "Wheel/rail squeal and impact noise: What do we know? What don't we know? Where do we go from here?," *Journal of Sound and Vibration*, Vol. 116, No. 2, pp. 339-353, 1987.
[5] Thompson, D., Squicciarini, G., et al., "A state-of-the-art review of curve squeal noise: phenomena, mechanisms, modelling and mitigation," *Proceedings of IWRN12*, pp. 1-27, 2016.
[6] Sueki, T., Kawaguchi, T. et al., "Experimental study on curve squeal noise with a test train (Wheel measurement part)," *Proceedings of J-Rail 2018*, No. U00120, 2018 (In Japanese).
[7] Kawaguchi, T., Sueki, T., et al., "Railway noise above 10 kHz generated on a curved section of high-speed railway line," *Proceedings of Inter-noise 2018*, No. 1712, 2018.

Authors

Takeshi SUEKI, Dr.Eng.
Chief Researcher, Noise Analysis Laboratory, Environmental Engineering Division
Research Areas: Railway Noise

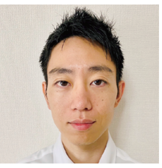

Takuma NITTA
Supervisor, Head of the Kanazawa Branch Environmental Measures Office, West Japan Railway Company
Research Areas: Railway Noise

Yasuhiro SHIMIZU
Assistant Senior Researcher, Noise Analysis Laboratory, Environmental Engineering Division
Research Areas: Railway Noise

Kentarou TAKAI
Supervisor, West Japan Railway Company
Research Areas: Railway Noise

Summaries of Papers in RTRI REPORT (in Japanese)

Evaluation of Durability of Vibration Isolation Materials and Vibration Characteristics of Track Structure in Floating Track with Under Sleeper Pads

Shota FUCHIGAMI, Yoshihiro MASUDA, Takatada TAKAHASHI

(Vol.39, No.2, 1-7, 2025.2)

Although a floating track with coil-spring units has excellent effects in reducing ground vibration, some cases have been reported in which rail corrugation occurs not only on the low rail but also on the high rail in some sharp curve sections. Therefore, we developed a floating track with under sleeper pads in order to reduce the occurrence of rail corrugation on high rails and the construction costs of the floating track with coil-spring units. In this paper, the fatigue durability and other properties of the vibration isolation materials (foamed EPDM and urethane) were evaluated, as well as the vibration characteristics of the track when a motorcar runs on the full-scale track.

Effect of Snow Properties on Shear Strength at the Base of Snowpack

Ryota SATO, Daisuke TAKAHASHI, Katsuhisa KAWASHIMA, Takane MATSUMOTO

(Vol.39, No.2, 9-14, 2025.2)

In this study, we investigated the effect of snow properties on the shear strength at the base of snowpack. The measurements of the shear strengths in the field showed that they ranged from 0.3 to 3.8 kN/m^2 with an average value of 1.5 kN/m^2. Despite the variation, it was confirmed that shear strength was positively correlated with dry snow density and snow hardness, and negatively correlated with liquid water content. In addition, in order to understand the shear strength of snowpack under rainfall or rapid melting of snow, we measured that of snowpack sprayed with water.

Dynamic Response Characteristics of Continuous Girder Bridge During Train Passage and a Simple Evaluation Method for Impact Coefficient

Munemasa TOKUNAGA, Manabu IKEDA

(Vol.39, No.2, 15-23, 2025.2)

This study organized and generalized the structural specifications of general railway continuous girders and then carried out comprehensive dynamic response analysis of continuous girders during train passage. The impact coefficient of the deflection of the continuous girder shows multiple peaks at the resonant speed for each natural vibration mode. When the number of spans is odd, the 1st and 3rd modes are amplified at the resonant speed, and when the number of spans is even, the 2nd mode is amplified at the resonant speed. Based on clarified dynamic response characteristics of continuous girder, a simple evaluation method of the impact coefficient with the applicable range up to 400 km/h has been proposed, and its validity has been demonstrated.

Method for Verifying the Restorability of Railway Viaducts Using the Recovery Time After an Earthquake as a Verification Index

Kimitoshi SAKAI, Kazunori WADA, Akihiro TOYOOKA

(Vol.39, No.2, 25-32, 2025.2)

We have proposed a method for evaluating the restorability of railway structures. In the proposed method, all earthquake motions expected within the design service life are used as the design earthquakes. In addition, the recovery time after an earthquake, which is directly related to early recovery, is used as the verification index. We also proposed a more practical method of expressing structural conditions with the same recovery time as a nomogram by performing calculations under various conditions in advance. The proposed method allows us to construct structures that are easy to recover in the same procedure as the conventional seismic design, and it is expected to shorten the recovery time after an earthquake.

Method for Verifying Local Buckling of Steel Plate Elements of Steel and Composite Structures

Manabu IKEDA, Yusuke KOBAYASHI

(Vol.39, No.2, 33-39, 2025.2)

In the design of steel and composite structures, it is important to accurately evaluate the buckling resistances of steel members. This paper first summarizes the basis and problems of the local buckling ultimate strength curves of steel plates in conventional design standards. In addition, the local buckling ultimate strength curves were revised on the basis of recent findings, and a trial design of composite beams was carried out using the revised local buckling strength evaluation method. The results confirmed that the revised method allows a more economical design for the upper flange of composite girders.

Proposal of Seismic Design Information of Poles Made of Aluminum Alloy in Overhead Contact Systems

Yuichi KONDO, Mizuki TSUNEMOTO, Takashi KANAIRO, Yuki NAKAJIMA

(Vol.39, No.2, 41-46, 2025.2)

Since aluminum alloy is lightweight with excellent corrosion resistance, installing poles made of aluminum alloy could improve workability and maintainability. However, the Seismic Design Guideline for Overhead Contact Systems and Commentary does not specify seismic design information of poles of aluminum alloy. Therefore, we conducted experiments and analyses of poles of aluminum alloy from the viewpoint of seismic design. Based on those results, we proposed the information of poles of aluminum alloy to enable seismic design in accordance with the Seismic Design Guideline for Overhead Contact Systems and Commentary.

Overview of Revised Design Standard and Commentary for Railway Structure (Steel and Composite Structures)

Yusuke KOBAYASHI

(Vol.39, No.2, 47-53, 2025.2)

Design Standard and Commentary for Railway Structures (Steel and Composite Structures) was revised in March of 2024. The revision not only reorganizes the previous design standards established mainly for each type of structure and material, but also introduces the latest verification techniques to make the design standards easier to use. The application of the revised design standard to design work will lead to realizing superior railway structures. This paper shows the overview of the revised Design Standard and Commentary.

Generation Mechanism of Localized Wear of Cu-impregnated Metalized Carbon Contact Strip

Yoshitaka KUBOTA, Takamasa HAYASAKA, Shinichiro KOGA, Hidehiko NOZAKI

(Vol.39, No.3, 1-9, 2025.3)

Localized wear of pantograph contact strips is an urgent problem to be solved, as it can lead to the fusion of the pantograph head and subsequent breakage of the overhead contact wire. However, the mechanisms underlying localized wear have not yet been clarified, and effective countermeasures have not been established. The aim of this study is to clarify the generation mechanism of localized wear in the copper-impregnated type of metalized carbon contact strip. Therefore, we analyzed actual worn strips using a micro Raman spectrometer and investigated the sliding wear behavior of contact strips with different degrees of graphitization of the carbon substrate using a block-on-ring-type wear tester.

Numerical Investigations on Validity of Method for Measuring Wheel-Rail Lateral Contact Position with Instrumented Wheelset Using Shear Strains Induced on Wheel Web

Takatoshi HONDO, Shoya KUNIYUKI, Hiroki YAMASHITA, Hiroyuki SUGIYAMA

(Vol.39, No.3, 11-16, 2025.3)

Instrumented wheelsets are widely used in the railway industry to measure wheel-rail interaction forces, which are crucial factors in assessing running safety. Information on the lateral contact position between wheel and rail is also an important factor in assessing wheel-rail contact conditions, such as the friction coefficient at the contact point. In the previous studies, the authors proposed a method for measuring the lateral contact position using an instrumented wheelset using shear strains on the wheel web and a signal processing procedure based on a frequency decomposition of the strain signal. In general, it is difficult to verify the measurement accuracy of the contact position under actual operating conditions of railway vehicles, since it is difficult to acquire comparative data of the contact position. In this paper, a numerical tool is developed to emulate the strain signals observed at the instrumented wheelset. This tool consists of a wheel deformation analysis based on finite element analysis and a vehicle dynamics simulation based on multibody dynamics. In addition, the proposed signal processing procedure is verified using the numerical tool.

Stability Analysis of Pantograph Under Sliding Condition Based on Excitation Test

Shigeyuki KOBAYASHI, Yuki AMANO, Yoshitaka YAMASHITA

(Vol.39, No.3, 17-22, 2025.3)

When railway vehicles run at low speeds, unstable vibrations may occur on the pantograph due to the high coefficient of friction. In order to reduce the maintenance cost of the contact strips, there is a need for a method to analyze the stability of the pantograph taking the friction coefficient into account. Stability analysis can be performed by constructing an analytical model of the pantograph, but building such a model requires high costs. Therefore, this study proposes a method to analyze the stability using the measurement of the frequency response function (FRF) of the pantograph when the vehicle is stationary. Since this method predicts the FRF in the sliding state, the construction of an analytical model is not required. In this method, the FRF is measured by exciting the contact strips, and the FRF in the sliding state is estimated by assuming a friction coefficient. Modal characteristics are identified using the estimated FRF, and stability analysis is performed using positive or negative damping ratios. The validity of the results of this analysis was verified by comparing them with the results of the low-speed sliding tests of the pantograph.

A Method for Constructing Geosynthetics-Reinforced Soil Retaining Wall with Rigid Face Using Lightweight Buried Formwork Applicable to Narrow Spaces

Yuki KURAKAMI, Susumu NAKAJIMA, Takeharu KONAMI, Yoshio YAMASHITA

(Vol.39, No.3, 23-29, 2025.3)

We proposed a method for constructing geosynthetics-reinforced soil retaining wall with rear face applicable to narrow spaces. We developed "components that can follow the settlement of embankment," to prevent settlement of embankment from affecting the deformation of the formwork when embankment and formwork are connected. In the proposed method, using the developed components together with lightweight buried formwork, the formwork and reinforcing embankment can be constructed simultaneously from the rear side, without the need for scaffolding. A test construction was carried out to confirm the feasibility of the proposed method. As a result, the developed components in a 2.4 m-high retaining wall were shown to function properly against the settlement of embankment. Considering the sliding amount of the developed components, the applicable height for this method is assumed to be up to approximately 4.0 m.

Evaluation of the Effect of Loose Bearing of Bridge on Onboard Measured Track Geometry Using Numerical Analysis

Koji HATTORI, Kodai MATSUOKA, Hirofumi TANAKA

(Vol.39, No.3, 31-38, 2025.3)

The occurrence of a bearing loosed with a gap in steel bridges is visually detected in situ, which is quite labor intensive. This study investigated the effect of a loose bearing on track geometry using a developed numerical calculation method as a basic investigation of detecting a loose bearing using the track geometry. A non-linear spring representing the loose bearing has been introduced into the existing calculation tool identifying the loaded track geometry considering the structural deformation. The result of the above simulation clarified that the displacement of the loose bearing appears on the track geometry as a local fluctuation with a half wavelength of about 5 m, regardless of the amount of loose.

Effect of Natural Period of Ground in Linear Region on Combination of Inertia Force and Ground Deformation in Seismic Deformation Method

Niki TANAKA, Kimitoshi SAKAI

(Vol.39, No.3, 39-45, 2025.3)

Inertia force and ground deformation are used to calculate the seismic response values of pile foundation structures using the seismic deformation method. In this paper, a study was carried out towards a highly accurate estimation of the combination of inertia force and ground deformation. Specifically, linear dynamic analyses were conducted on various types of grounds and structures, and the combination coefficients for the ratio of the period of grounds to the period of structures were calculated. As a result, it is clarified that the correction coefficient ν gradually decreases as the natural period of the ground T_g increases. Considering this tendency, we proposed a simple estimation method for the combination coefficients. In addition, it was confirmed that the proposed method expressed the results of dynamic analysis more appropriately than the conventional method. The proposed method makes the combination coefficients more accurate and the seismic response values of structures more reasonable.

Automated Crew Scheduling Method to Minimize the Number of Crew Required

Satoshi KATO, Taichi NAKAHIGASHI, Tatsuya KOKUBO

(Vol.39, No.3, 47-53, 2025.3)

Railway companies produce crew schedules when they revise their train timetables. Currently, these schedules are produced manually by experts. However, this manual task is time-consuming. It is therefore necessary to develop a system that supports crew scheduling using an automated algorithm. We propose an automated crew scheduling algorithm based on mathematical optimization to minimize the number of crew required. The results of a computational experiment using real data from a railway line confirmed that the proposed algorithm can quickly generate an efficient crew schedule in terms of the number of crew required.

Evaluation for Running Safety of Railway Vehicles against Localized Strong Winds

Hiroyuki KANEMOTO, Yu HIBINO

(Vol.39, No.4, 1-8, 2025.4)

High-rise buildings can create localized strong winds, a phenomenon known as “building winds.” However, safety assessment methods for trains running in the vicinity of such winds have not yet been established. Therefore, we proposed a method to evaluate the running safety of a vehicle overturned by localized strong winds. Specifically, wind tunnel experiments, computational fluid dynamics analyses, and vehicle dynamics simulations were conducted to investigate the effects of localized strong wind caused by buildings on the behavior of railway vehicles. The results showed that when the rise time of the aerodynamic force acting on the vehicle is less than approximately 2 seconds, the rate of wheel load reduction increases compared to static analysis conditions.

Impact of Tamping Work on Repeated Ballast Settlement

Takahisa NAKAMURA, Tomoaki HIROO, Akiko KONO

(Vol.39, No.4, 9-15, 2025.4)

It has been confirmed that the track irregularity gradually returns to its original shape after ballast tamping for the ballast track even under the same track and support structure conditions. However, the details of this mechanism are not revealed. Therefore, we surveyed an actual situation using track inspection data for this phenomenon. In addition, we performed tests with small model, discontinuum analysis for ballast density after ballast tamping and cyclic loading test to reveal the mechanism of the reversion in settlements after and before ballast tamping.

Proposal for a Method That Takes into Account the Damage Process before Sliding Failure to Verify the Seismic Performance of Railway Embankments and Its Application to Safety Assessment

Ryuichi IBUKI, Tatsuya DOI, Jun IZAWA, Kentaro UEMURA, Sokkheang SRENG

(Vol.39, No.4, 17-24, 2025.4)

Newmark’s sliding block method is used as a standard response analysis method in the seismic design of railway embankments. Although this method is very practical and useful, it has some problems, for example, that it cannot accurately simulate the actual damage to embankments observed in past major earthquakes. In this paper, the authors propose a performance verification method for the seismic stability of embankments taking into account the damage process using the shear strain accumulated at the toe of the embankment as a verification index, the validity of which is verified using the centrifuge shake table tests. In addition, as an example of application of the proposed safety assessment method, the response analysis using a finite element method is also discussed.

Modeling for Longitudinal Displacement of OCL and Method for CalculatingI Its Equilibrium Points

Yoshitaka YAMASHITA, Koki SATO

(Vol.39, No.4, 25-32, 2025.4)

Overhead contact lines (OCLs) are subject to longitudinal displacement due to factors such as temperature changes and external forces. Excessive longitudinal displacement may prevent the tensioning devices from performing their proper tension adjustment function. It is therefore important to develop a method for calculating the longitudinal displacement of OCLs and to be able to predict the longitudinal displacement in response to changes in temperature and external forces. This paper presents a model to represent the longitudinal displacement of OCLs on a curved track installing tensioning devices and hinged cantilevers at each support point and proposes a method for calculating the equilibrium points of the longitudinal displacement of the OCL. Furthermore, the proposed calculation method was verified by scale model tests.

Immediacy and Accuracy of Earthquake Early Warning Method Based on P-wave Threshold Exceedance Applied to the 2004 Mid Niigata Prefecture Earthquake

Misa MORIWAKI, Seiji TSUNO, Masahiro KORENAGA

(Vol.39, No.4, 33-40, 2025.4)

The immediacy and accuracy of the earthquake early warning method based on P-wave threshold exceedance was verified by applying it to data from the 2004 Mid-Niigata Prefecture earthquake. The result confirmed that it is possible to issue an earthquake warning in less than one second in the vicinity of the earthquake source fault region by directly predicting the S-wave by multiplying the pre-calculated amplitude ratios of the S-wave to the P-wave by the P-wave observed in real time. Furthermore, the logarithmic standard deviation of the peak ground acceleration (PGA) of the observed S-wave from the PGA of the predicted S-wave was as small as 0.284, indicating that this method can predict S-wave amplitudes with high accuracy.

QUARTERLY REPORT of RTRI

第 66 巻　第 2 号	Vol. 66, No. 2
2025 年 5 月 1 日　発行	Published date: 1 May 2025
監修・発行所：公益財団法人鉄道総合技術研究所	Supervision/Publisher: Railway Technical Research Institute
〒 185-8540　東京都国分寺市光町 2-8-38	Address: 2-8-38 Hikari-cho, Kokubunji-shi, Tokyo 185-8540, Japan
発行人：芦谷公稔	Issuer: Dr. Kimitoshi ASHIYA
問い合わせ：鉄道総研広報	Contact us: Public Relations, Railway Technical Research Institute Mail Address: rtripr@rtri.or.jp

QUARTERLY
REPORT of
RTRI

RAILWAY TECHNICAL RESEARCH INSTITUTE

Printed in Japan